Observational Constraints on the Number, Albedos, Sizes, and Impact Hazards of the Near-Earth Asteroids

by

Joseph Scott Stuart

BSE Electrical Engineering and Computer Science
University of Pennsylvania, 1993

SUBMITTED TO THE DEPARTMENT OF EARTH, ATMOSPHERIC AND PLANETARY SCIENCES IN PARTIAL FULLFILLMENT OF THE REQUIREMENTS FOR THE DEGREE OF

DOCTOR OF PHILOSOPHY IN EARTH, ATMOSPHERIC AND PLANETARY SCIENCES
AT THE
MASSACHUSETTS INSTITUTE OF TECHNOLOGY

June 2003

Signature of Author:_____
Department of Earth, Atmospheric and Planetary Sciences
21 March 2003

Certified by:_____
Richard P. Binzel
Professor of Earth, Atmospheric, and Planetary Sciences
Thesis Supervisor

Accepted by:_____
Ronald G. Prinn
Head
Department of Earth, Atmospheric, and Planetary Sciences

Observational Constraints on the Number, Albedos, Sizes, and Impact Hazards of the Near-Earth Asteroids

by

Joseph Scott Stuart

Submitted to the Department of Earth, Atmospheric, and Planetary Sciences on March 21, 2003 in Partial Fulfillment of the Requirements for the Degree of Doctor of Philosophy in the Field of Planetary Science

Abstract

This work provides a statistical description of the near-Earth asteroids (NEAs) in terms of number, orbital parameters, reflectance spectra, albedos, diameters, and terrestrial and lunar collision rates. I estimate the size and shape of the NEA population using survey data from the Lincoln Near-Earth Asteroid Research project including more than 1300 NEA detections. The NEA population is more highly inclined than previously estimated and the total number of NEAs with absolute magnitudes (H) brighter than 18 is 1227^{+170}_{-90}.

The absolute magnitude and orbital parameter distributions for the NEAs are combined with reflectance spectra and albedo measurements. I obtain a debiased estimate of the fraction of NEAs in each of 10 taxonomic complexes, and a debiased average albedo for each. The number of NEAs larger than 1 km is 1090±180.

Next, I determine the impact frequency, collision velocity distribution and collision energy distribution for impacts of NEAs into the Earth and Moon. Globally destructive collisions (~10^{21} J) of asteroids 1 km or larger strike the Earth once every 0.60±0.1 Myr on average. Regionally destructive collisions with impact energy greater than 4×10^{18} J (~200 m diameter) strike the Earth every 47,000±6,000 years. The rate of formation of craters expected from the NEAs is found to be in close agreement with the observed number of craters on the Earth and Moon.

These results combine the largest set of NEA discovery statistics from a single survey, the largest set of physical data on NEAs, and corrections for observational bias. The result is a comprehensive estimate of the total NEA population in terms of orbital parameters, absolute magnitudes, albedos, and sizes. This improved description of the NEAs will help us to plan surveys to find and study the remaining undiscovered NEAs, to connect the NEAs to their origins in the main-belt, to connect the NEAs to meteorite samples, to compare the lunar and terrestrial cratering record to the current population of potential impactors, and to understand the magnitude of the NEA impact hazard to the Earth's biosphere.

Thesis Supervisor: Richard P. Binzel
Title: Professor of Earth, Atmospheric, and Planetary Sciences

Acknowledgements

Je voudrais d'abord remercier Rick Binzel qui a uniformément fait tout son possible afin de m'aider à accomplir mes buts principaux: approfondir mes connaissances, publier mes recherches, et finir mes études doctorales. Il a gracieusement guidé l'orientation de mes recherches dans un domaine fructueux et il a également fourni mon projet avec un bon nombre de données de haute qualité. De plus, il a lu toutes mes ébauches de thèse avec une rapidité étonnante, et cela en dépit d'un programme très chargé. Pour ces raisons ainsi que d'autres, je lui suis très reconnaissant.

I am deeply indebted to the entire team that makes the Lincoln Near-Earth Asteroid Research (LINEAR) Project a success. Frank Shelly and the other engineers at the telescope site have done a superb job of designing the system and keeping it running. Of course, special thanks go to the observers who stay up all night to collect the photons. All of those asteroid detections would go to waste if it weren't for the busy folks at the Minor Planet Center to keep track of all the orbits.

I would also like to thank three of Rick's former students and a postdoc: Bobby Bus, Tom Burbine, Steve Slivan, and Andy Rivkin. They have enlightened me on many aspects of asteroid research and academic procedure. My work was greatly enhanced by scientific discussions with Bill Bottke and Al Harris, both of whom also offered suggestions for improving early drafts of chapters of this thesis. The members of my thesis examination committee, Rick Binzel, Jim Elliot, Jack Wisdom, and Al Harris provided many useful suggestions for improving the final draft of my thesis.

The management of MIT Lincoln Laboratory, Gerry Banner, Grant Stokes, Hsiao-Hua Burke, and the Lincoln Scholar's Committee not only provided the financial resources for me to attend graduate school, but also gave me the latitude to pursue an academic goal. Many of my coworkers at Lincoln Laboratory have helped me along the way, including Ron Sayer, Pablo Hopman, Herb Viggh, and Jenifer Evans.

Successful academic pursuits require a great deal of support and encouragement from outside academe, as well. In that regard I have been quite blessed. My Mother has always been there for me, and instilled in me early in life a respect for education. My many friends at Thursday Night Dinner have helped keep me entertained and fed through

the years of toil. And I am most indebted to and thankful for my family. My dear wife Meg, has helped and supported me in more ways than I could possibly list. My son Benji, came into my life midway through this PhD process and changed everything. Without a word, he has taught me volumes about curiosity, determination, and joyfulness.

Table of Contents

Abstract 3
Acknowledgements 5
Table of Contents 7
Chapter 1 Introduction 9
1.1 History of Impact Threat 10
1.2 History of NEA Discovery 12
1.3 History of Population Estimates 13
1.4 Origin of the NEAs 14
1.5 Meteorites and Resources 17
1.6 Some Definitions 17
1.7 Scope of this Work 19
Chapter 2 An NEA Population Estimate From the LINEAR Survey 21
2.1 Abstract 21
2.2 Introduction 21
2.3 LINEAR Survey Data 22
2.4 Debiasing Technique 29
2.5 Detection Probability Analysis 30
2.6 Debiasing 33
2.7 Absolute Magnitude and Orbital Element Distributions 35
2.8 Comparisons to Other NEA Population Estimates 40
2.9 Conclusions 44
Chapter 3 Albedo Bias in NEA Discovery. 47
3.1 Abstract 47
3.2 Introduction 47
3.3 Description of Luu and Jewitt Model 48
3.4 Further Experiments with the LJ Model 50
3.4.1 Differential Phase Darkening versus Albedo 51
3.4.2 Changing the Albedos 52
3.4.3 Limiting Magnitude of Survey 53
3.5 Bias Model Based on Orbital Distributions 53
3.6 Conclusions 54
Chapter 4 Albedos and Diameters of the NEAs 57
4.1 Abstract 57
4.2 Introduction 57
4.3 Spectroscopic and Albedo Data 58
4.4 Trends in Albedo Data 62
4.5 Trends in Taxonomic Data 66
4.6 Absolute Magnitude and Diameter Distributions 73
4.7 Magnitude-limited Debiasing 76
4.8 Alternate Bias Estimation 79
4.9 Debiasing with Tisserand Parameter 87
4.10 Diameter Distribution of the NEAs 91
4.11 Summary 94
4.12 Discussion 95

Chapter 5 The NEA Impact Hazard 99
5.1 Abstract 99
5.2 Introduction 99
5.3 Impact Probability Calculations 101
5.4 Reassessing the Earth Impact Hazard 107
5.5 Cratering Dynamics 111
5.6 Crater Counting on the Moon 117
5.7 Comparison with the Lunar Crater Record 119
5.8 Comparison with the Terrestrial Crater Record 122
5.9 Conclusions 123
Chapter 6 Conclusions and Future Work 125
6.1 Conclusions 125
6.2 Future Work 129
References 132
Appendix: Definitions 145
A.1 Absolute Magnitude 145
A.2 Orbital Parameters 146
A.3 Jovian Tisserand Parameter 147

Chapter 1 Introduction

The near-Earth asteroids (NEAs) are a population of small, sun-orbiting bodies whose orbits bring them near to the Earth's orbit. NEAs and other groups of asteroids sparsely fill the inner solar system interior to Jupiter's orbit (Figure 1.1). NEAs provide a link between the meteorites and the main-belt asteroids that is important for placing the geochemical information obtained from the meteorites into a spatial context to understand the formation of our solar system. The NEAs have the potential to collide with the Earth, leaving interesting geological formations and producing extreme devastation that may have substantially altered the evolution of life on Earth. Collisions of NEAs on the Earth are a long-term hazard for Earth's inhabitants.

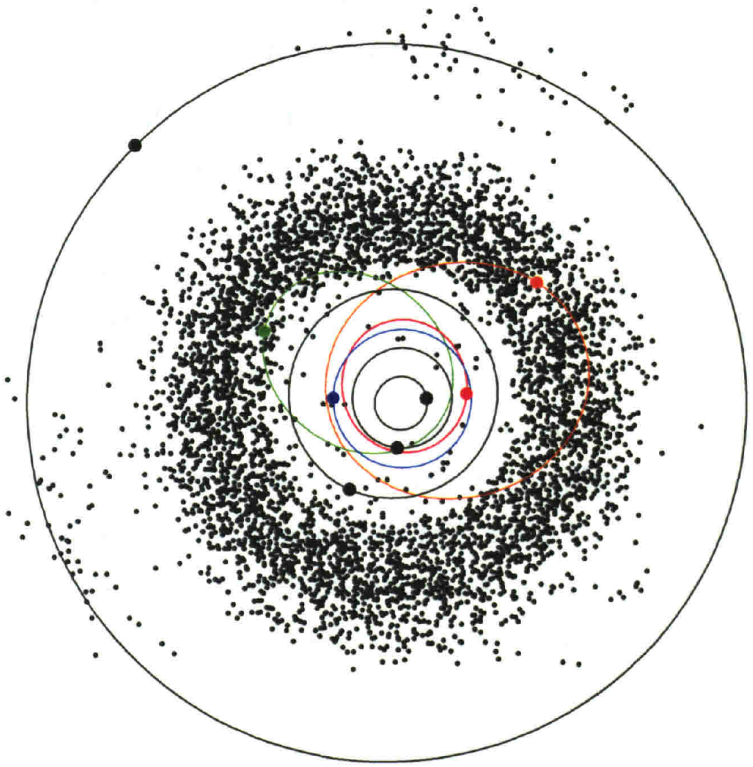

Figure 1.1 Inner Solar System On March 21, 2003 (JD 2452720). The five inner-most planets, are in black (except for the Earth, in blue). The first 5,000 numbered asteroids are shown as black points. Also shown are the orbits and locations of three prototypical NEAs: (1221) Amor in orange, (1862) Apollo in green, and (2062) Aten in red. These illustrate the orbital groups named for those three asteroids.

1.1 History of Impact Threat

The possibility of small celestial bodies approaching and colliding with the Earth was recognized even before the first asteroid was discovered in 1801. Edmond Halley speculated in 1705 that comets could strike the Earth. For most of the first century after asteroids were discovered, they seemed to be confined to the main belt where they would pose no threat to the Earth.

In 1908, a small asteroid exploded in the air above an area of Siberia known as Tunguska. Atmospheric pressure waves, seismic waves, and dust clouds from that event were observed over much of the Earth. The first scientist to visit the site, Leonid Kulik, wasn't able to get there until 1927 but still found vast devastation. By then, most scientists already suspected that the Tunguska explosion had been caused by a small comet or asteroid impact. Only in the last few years has consensus emerged that the 10 megaton explosion was caused by an asteroid rather than a comet (Sekanina 1998).

By 1951, when E. J. Öpik derived formulas for calculating the probabilities of asteroids colliding with planets (Öpik 1951), it was clear to the small number of asteroid researchers that asteroids could collide with the Earth. At the same time, there was an ongoing debate about the origin of the craters on the Moon. The idea that most were volcanic fell by the wayside as evidence mounted that the craters were from impacts. Then E. M. Shoemaker proved that Barringer Crater in Arizona was from an impact (Shoemaker 1960). Within a few years, Shoemaker's detailed comparison of Barringer Crater and several lunar craters had convinced nearly everyone that most of the craters on the Moon were of impact origin. The lunar samples returned by the Apollo missions removed any remaining doubt, and greatly enhanced our understanding of impacts. With so many impact craters easily visible on the Moon, the sometimes violent nature of the solar system was inescapable.

Even so, the fact that asteroid impacts could happen on the Earth was not widely recognized by the public. A group of M.I.T. students probably did more to popularize the threat of asteroid impacts than anyone else. A close approach to the Earth of the large NEA (1566) Icarus in 1967 prompted M.I.T. professor Paul Sandorff to assign to his systems engineering students the task of planning a mission to deal with a pending Earth

impact of an asteroid like (1566) Icarus with only 18 months warning. The results of the students' efforts were widely publicized with an article in Time Magazine, a book (Li 1979), and eventually, a Hollywood movie (*Meteor,* 1979).

In the same year *Meteor* was released, Louis Alvarez and colleagues made a crucial scientific discovery. They found a concentration of iridium in the geological stratum at the Cretaceous-Tertiary boundary. The 65 Myr old K/T boundary corresponds to a mass extinction event that saw the demise of 80% of Earth's species, including the dinosaurs. Iridium is rare on Earth, but common in meteorites, so Alvarez *et al.* attributed the mass extinction to an impact (Alvarez *et al.* 1980). This was the beginning of widespread recognition that impacts have profoundly affected life on Earth. The coincidence of a large impact at the K-T boundary has since been confirmed by a number of geochemical analyses (Bauluz *et al.* 2000) and by the discovery of the 65 Myr old, 170 km diameter Chicxulub impact crater off the Yucatan Peninsula of Mexico (Frankel 1999).

In 1991, NASA convened two working groups to consider the hazard posed by asteroid and comet impacts and to suggest strategies for mitigating the threat. The resulting Spaceguard Survey (Morrison 1992) has greatly influenced scientific attitudes about the impact hazard, and has motivated the U.S. and other governments to support NEA research.

A truly extraordinary event occurred in 1994 that further publicized the dangers posed by asteroid and comet impacts. The comet Shoemaker-Levy 9, while passing by Jupiter, was captured into orbit about Jupiter and torn apart into a few dozen pieces which then collided into the giant planet (Levy 1998). Fortunately, this event was predicted far enough in advance that a major observational campaign was undertaken involving three interplanetary spacecraft (Galileo, Ulysses, and Voyager 2), the Hubble Space Telescope, and many Earth-based observatories. The resulting pictures of Earth-sized scars in Jupiter's atmosphere drove home the message that impacts continue to occur in our solar system.

In the late 1990s and early 2000s, due to the success of the many NEA search programs, and improvements in predicting NEA orbital trajectories, a series of

predictions have been made that specific NEAs may hit the Earth at predictable times a few decades later. The first of these predictions, made in early 1998, involved (36396) 1997 XF11, which was predicted to have a small probability of impacting the Earth in 2028. The asteroid was quickly proven safe with more observations and better orbit analysis, but the resulting media attention brought the issue of asteroid impacts to public awareness. That episode highlighted the need for the NEA community to develop methods of clearly communicating the dangers of asteroid impacts without hyperbole. The Torino Scale (Binzel 2000) was adopted as a result. Several more predictions have been made of potential NEA impacts, but most have been proven safe after further observations allowed for more accurate orbit determination.

1.2 History of NEA Discovery

When the first NEA was discovered [(433) Eros in 1898] it was not initially called an NEA. However, it was recognized as an unusual object; it was the first asteroid discovered that was not confined to the main belt, and the first that crossed the orbit of a planet (Mars). Several decades passed before astronomers found asteroids that closely approach or cross the Earth's orbit. In 1932, Delporte discovered (1221) Amor and Reinmuth discovered (1862) Apollo. Apollo and Amor quickly became the archetypes and namesakes of two groupings of NEAs. The Amor asteroids have orbits that are entirely beyond, but close to, the Earth's orbit. The Apollo asteroids have orbits that cross the Earth's orbit. Continuing in the competition to find asteroids that approach closer to the Earth, Delporte found (2101) Adonis in 1936, which passes 2.4 million km from the Earth's orbit. Reinmuth found (unnumbered) Hermes, in 1937, which passed only 800,000 km from the Earth in 1937.

The growing number of asteroid discoveries prompted the astronomical community to establish the Minor Planet Center (MPC) in 1947 to serve as a central repository for asteroid observations, to maintain a catalog of asteroid orbits, and to quickly notify astronomers of important observational opportunities. The MPC still serves those roles in 2003, and also coordinates follow-up observations to pin down the orbits of newly discovered NEAs and other interesting asteroids.

The work of the MPC was increased when the first dedicated survey to find asteroids, the Yerkes-MacDonald Survey, was started in 1950 by G.P. Kuiper (Kuiper *et al.* 1958). The survey ran from 1950 to 1952 and discovered 1550 asteroids. That was followed by the Palomar-Leiden Survey in 1960 (van Houten *et al.* 1970), which found over 2000 asteroids in two months of observations. Both of those surveys were designed to find main-belt asteroids. The first search specifically designed to find NEAs was the Palomar Planet-Crossing Asteroid Survey, started in 1973 by E.M. Shoemaker and E.F. Helin (Helin and Shoemaker 1979). They discovered 5 new NEAs, 7 new mars-Crossers, and many main-belt asteroids.

In the 1980s, the advent of charge-coupled devices (CCDs) as astronomical instruments revolutionized the search and study of asteroids of all types (Janesick and Elliot 1992). The first group to make use of CCDs to search for asteroids was Spacewatch, which discovered its first asteroid in 1985, but became fully operational as a large search effort in 1990 (McMillan 2000).

Complementing Spacewatch, the Lowell Observatory Near Earth Object Search (LONEOS) began in 1993 with the principal goal of discovering NEAs and near-Earth comets. In 1995, E.F. Helin began the second Palomar survey to find NEAs, the Near Earth Asteroid Tracking Program (Pravdo *et al.* 1997). In 1996, MIT Lincoln Laboratory began the Lincoln Near-Earth Asteroid Research (LINEAR) program (Stokes *et al.* 2000). Spacewatch, LONEOS, NEAT and LINEAR are still operating in 2003.

1.3 History of Population Estimates

E. J. Öpik started efforts to estimate the total number of NEAs, calculating that there are approximately 34 Apollo type NEAs with diameters larger than 1.0 km (Öpik 1963). He was soon followed by Whipple (1967) who predicted that there must be at least 50 Apollos bigger than 1 km. Both of those predictions were made with fewer than 10 known Apollos. Thanks to a continued slow trickle of discoveries of NEAs, and then to the success of the Palomar Planet Crossing Asteroid Survey, by the late 1970s the number of known NEAs had risen to about 50. This almost two-fold increase in the number of known NEAs resulted in about a 30-fold increase in the estimate of the total number of NEAs. G.W. Wetherill (1976) suggested that there are about 1200 NEAs

bigger than 500m. Helin and Shoemaker (1979) estimated that there were 1500 – 2500 NEAs brighter than absolute magnitude 18 (absolute magnitude is defined in Chapter 1A.1). Through the 1980s and early 1990s, the 1979 results of Helin and Shoemaker stood as the best estimates of the NEA population, with Shoemaker *et al.* (1990) making a minor adjustment to that estimate.

In 1993 and 1994, Rabinowitz and coauthors (Rabinowitz *et al.* 1993, Rabinowitz 1994) used data from Spacewatch to speculate that there is a belt of small (less than 50 m diameter) asteroids in low eccentricity orbits very near the Earth. The first new estimate of the number of large NEAs since the Palomar estimates of the late 1970s lowered the estimated number of NEAs with absolute magnitudes brighter than 18 to 700 ± 230 based on 26 NEAs detected in that size range (Rabinowitz *et al.* 2000). Also in 2000, a new technique was used by Bottke *et al.* (2000, 2002) that combined Spacewatch observations of NEAs with dynamical models of the origins of NEAs to estimate that there are 960 ± 120 NEAs brighter than absolute magnitude 18. A.W. Harris (2001) used the results of all of the NEA survey programs to estimate the number of NEAs as ~1000 brighter than absolute magnitude 18. D'Abramo *et al.* (2001) applied a simple probabilistic model to data from the LINEAR survey to estimate the number of NEAs brighter than absolute magnitude 18 as 855±101. The same year, J. S. Stuart (2001) performed a detailed analysis of the LINEAR survey to estimate the NEA population; that work is presented in Chapter 2. A. W. Harris (2002) extended the population model of Stuart to smaller sizes to estimate that there are approximately 0.5 million NEAs with absolute magnitudes less than 24.5 (which is approximately the range for the Tunguska impactor).

1.4 Origin of the NEAs

NEAs had not been discovered when Daniel Kirkwood noticed gaps in the main-belt asteroids (Kirkwood 1876). But those gaps became important in understanding the relationship between the main-belt asteroids and NEAs. Early work on the origins of the NEAs concluded that NEAs must be constantly resupplied by some reservoir of small objects (Öpik 1963) because they survive for only a few million years before colliding with a planet, or the sun, or being ejected from the solar system. Recent analysis

confirms that NEAs can survive the chaotic dynamics of the inner solar system for only a few tens of millions of years (Gladman *et al.* 2000).

With such short lifetimes, the NEAs must be escapees from another group of small objects. Early researchers concluded that most NEAs must be extinct comets (Öpik 1961, 1963) because there weren't enough Mars-crossing asteroids to supply the NEAs. Over a decade later, the state of knowledge was much the same with the main belt being thought incapable of supplying NEAs through gravitational interactions with the planets (Wetherill 1976). A breakthrough came in the early 1980s when J. Wisdom discovered that chaotic dynamics in one of the Kirkwood gaps (the 3:1 commensurability with Jupiter in which an asteroid completes three orbits for each orbit of Jupiter) could quickly increase the eccentricity of an asteroid to make it cross the orbit of Mars or even the orbit of Earth or Venus (Wisdom 1981,1982,1983,1985). At about same time, J. G. Williams showed that secular resonances are capable of quickly increasing the eccentricities of main-belt asteroids to make them planet crossing (Wetherill 1979). The dynamics of the main-belt source regions were further explored by many researchers (Morbidelli *et al.* 2002a for a review) culminating with the work of Bottke *et al.* (2000, 2002) in which all of the potential NEA source regions are combined into a statistical model of the origins of the NEAs.

Taking a different approach to the problem of the origins of the NEAs, Binzel *et al.* 1992 showed that physical properties of the NEAs (spin rate and shape) match quite well with small (<5 km diameter) main-belt asteroids. This represented some of the first physical data on main-belt asteroids of comparable size to NEAs, and loosely constrained the cometary fraction of the NEA population to between 0 and 40 percent.

If the NEAs are derived from main-belt asteroids, they should be of similar composition. The main-belt asteroids are a diverse set of bodies that formed from a heterogeneous cloud of gas and dust over a range of temperatures, and they have undergone a variety of post-formation geological modification. Diversity in the composition of asteroids was first noticed by studying differences in their colors (Bobrovnikoff 1929). Systematic broadband photometry (Wood and Kuiper 1963, Chapman *et al.* 1971), combined with albedos (Chapman *et al.* 1975) lead to the

recognition of two broad classes of asteroids: the dark, "carbonaceous" types (C-types) that dominate the mid and outer main belt, and the brighter, "stony" types (S-types) that dominate the inner part of the main-belt. A more sophisticated taxonomy, based on eight-color photometry was introduced by Tholen (1984) in which the asteroids were divided into 14 classes. The advent of CCD spectroscopy in the 1980s allowed for a much richer description of the spectral reflectance properties of asteroids. These high resolution spectra were developed into an asteroid taxonomy comprising 26 classes by Bus (1999, Bus and Binzel 2002a, Bus and Binzel 2002b). I use the Bus taxonomy in Chapter 4 to address the compositional and size distribution of the NEAs.

Despite the likelihood that most NEAs are supplied from the main-belt, there are also undoubtedly comets among the NEAs. Comets are distinguished from asteroids, observationally, by virtue of displaying comae and tails when they are heated by the sun. Asteroids do not, and were thus named "star-like" by 19th century astronomers. This definition is not quite as simple as it sounds because comets may exhibit very little coma when weakly heated. Similarly, an asteroid could exhibit a temporary coma or tail if dust from its surface were kicked off from a small impact. Compositionally, asteroids are defined as being made of rock and metal, and formed in the inner solar system at temperatures too high for ices to condense from the solar nebula. Comets are made of ice, with an unknown, possibly large amount of dust and organic solids, and they formed further from the sun in cooler parts of the solar nebula. There is also overlap in the compositional definition since there are surely objects that are roughly equal mixes of ices and rocky material that formed near the boundary where ices could condense from the solar nebula.

Furthermore, the observational and compositional definitions of asteroids and comets are mismatched. After repeated passes through the inner solar system, comets that do not disintegrate into dust may lose most of their volatile ices and stop producing comae and tails; they become extinct comets. Or, they may build up a thick layer of dust and organic solids that insulates and covers the volatile ices preventing sublimation, rendering the comet dormant. These extinct and dormant comets would appear to be asteroids. Their orbits may also be modified to resemble asteroid orbits by interactions with Jupiter and the other planets. In this work, I use the term NEA to refer to objects

that meet the observational definition of asteroids. I will, however, further discuss the issue of extinct and dormant comets within the NEA population in Chapter 4.

1.5 Meteorites and Resources

The meteorites are an extraordinarily valuable sample of a wide range solar system materials that have undergone far less geological processing than rocks from the Earth. Chemical, elemental, and radioisotope analyses of meteorites led to nearly all of our current understanding of how the solar system, and the Earth itself, formed. Given that meteorites are in fact extraterrestrial, then they are, by definition, samples of rocky and metallic NEAs. To take full advantage of the meteorites, we must understand where they formed in the solar system and how they came to the Earth. Thus, an understanding of the NEAs, how they derive from the main-belt asteroids, and how they connect to the meteorite samples (Burbine 2000) is important to better understand the formation of the solar system, the Earth, and the formation of planets around other stars.

Two important steps have been made in connecting the meteorites to NEAs and main-belt asteroids. The first is that the genealogy of the Howardite-Eucrite-Dioginite (HED) meteorites has been definitively traced to the main-belt asteroid (4) Vesta (Burbine *et al.* 2001, Binzel and Xu 1993). The second is that the most abundant type of meteorite, the ordinary chondrites, have been tentatively associated with the most abundant type of NEAs and inner main-belt asteroids, the S types (Binzel *et al.* 1996).

In a very real sense, the NEAs are the Earth's nearest neighbors: many NEAs require less rocket fuel to reach, land on, and return material from than does the Moon. As humanity extends its operations in space the NEAs will eventually become a valuable repository of raw material including metals, but perhaps most importantly: water (Rivkin *et al.* 2002). Because of their accessibility, the NEAs may also provide convenient destinations for testing spacecraft as a step toward exploring more distant parts of the solar system. This process has already begun with the phenomenally successful trip to the asteroid (433) Eros by an unmanned NASA spacecraft (Veverka *et al.* 2001).

1.6 Some Definitions

The NEAs are dynamically defined as all asteroids with perihelion distances less than 1.3 astronomical units from the sun. Perihelion is the point in a solar elliptical orbit

that is closest to the sun, and an astronomical unit (AU) is the distance of the Earth from the sun. The NEAs are divided into three groups: Amors, Apollos, and Atens. The Amors have perihelion distances less than 1.3 AU, and greater than 1.017 AU, which is currently the maximum distance of the Earth from the sun. Thus Amor asteroids do not currently cross the Earth's orbit. The Apollos have perihelion distances less than 1.017 AU and semimajor axis greater than 1 AU. The semimajor axis is half of the length of the longest axis of the elliptical orbit (the Earth's semimajor axis is 1 AU). Aten asteroids have semimajor axes less than 1 AU, and aphelion distances greater than 0.983 AU, which is the minimum distance of the Earth from the sun. Aphelion is the point in a solar elliptical orbit which is furthest from the sun. Only one asteroid has been discovered with aphelion less than 0.983 AU (2003 CP20 discovered 11 February 2003). As more members of this class of asteroids are discovered, they may be classified as NEAs. See Figure 1.1 for a depiction of some asteroid orbits and Appendix A.2 for defintions of asteroid orbital parameters.

The definition of NEA as having a perihelion distance less than 1.3 AU is a somewhat arbitrary definition that is maintained primarily for backward compatibility with previous research. On the other hand, there is no other definition that is particularly better. The boundary at 1.3 AU was chosen to be near a minimum in the distribution of perihelion distances of the asteroids so that the fewest asteroids would be near the boundary (Shoemaker *et al.* 1979). With timescales of tens of millions of years, the orbits of Amors may be perturbed by gravitational interactions with the planets to drift out beyond the 1.3 AU boundary, or they may drift inward to become Apollos. Likewise, Apollos and Atens can drift into other categories on similar timescales. On even longer timescales, asteroids may move from deep within the main belt into near-Earth space. The definition of NEA using a perihelion distance of 1.3 AU provides a very simple definition that uses the current orbital elements and does not require extensive orbit analysis to determine if the asteroid may become Earth-crossing in the future (or was in the past). At the same time, it is a set of asteroids that is much smaller than the whole catalog of main-belt asteroids, and contains the vast majority of asteroids that could become Earth-crossing in several tens of millions of years.

1.7 Scope of this Work

When a telescopic survey detects asteroids, two types of measurements are made: astrometry and photometry. Astrometry is the process of measuring the position of the asteroid in relation to the background stars, which are used to define a common positional reference system. Astrometry spanning a few weeks or months is used to calculate an osculating orbit for the asteroid. The osculating orbit is an ellipse described by six parameters, defined in Appendix A.2, and a time, or epoch, for which the orbit is valid. The osculating orbit may be used to predict the location of the asteroid for times near the epoch. It may also be propagated to a different epoch by taking into account gravitational perturbations from the planets, and other factors. The NEAs have a range of orbits that make some NEAs easier to discover than others. There is thus an observational selection effect or bias that makes the distribution of orbital parameters for the known NEAs unrepresentative of the distribution for the as-yet-undiscovered NEAs. This observational bias depends in complicated ways on the orbits of the NEAs, as well as on the surveying strategy used. An important aspect of understanding the distribution of NEAs is to correct for this observational bias to obtain the true, unbiased distribution of the orbital parameters of the NEAs.

Photometry is the process of measuring the brightness of an asteroid. As with astrometry, the background stars are used for calibration. The apparent brightness of an asteroid depends on many factors: the brightness of the sun, the distance of the asteroid from the sun and the observer, the size of the asteroid, its reflectivity, or albedo, the asteroid's phase angle (*i.e.* the angle between the observer and the sun as measured at the asteroid), and a variety of observer specific parameters such as weather, detector sensitivity, etc. The brightness of the sun is well known. An asteroid's orbit, computed from astrometry spanning a few weeks or months, provides accurate enough information about the location of the asteroid relative to the Sun and Earth to be able to account for the asteroid's distance from the Sun, its distance from the observer, and its phase angle. The background stars are used to measure observer specific parameters such as atmospheric extinction and detector sensitivity. With each of those factors accounted for, the remaining variables that control the brightness of an asteroid are its size and albedo.

Those two parameters can be combined into a single parameter, the absolute magnitude (defined in Appendix A.1).

The number of NEAs, and of asteroids in general, increases rapidly as one moves to smaller and smaller sizes (or dimmer absolute magnitudes). However, smaller asteroids are dimmer (other factors being equal) than larger asteroids, and dimmer asteroids are more difficult to find with telescopic surveys. So, for example, it is likely that all or nearly all NEAs larger than about 5 km have already been found. However, perhaps only about half of the NEAs larger than 1 km have been found, and only a small fraction of NEAs larger than 100 m have been found. Characterizing the number of NEAs as a function size or absolute magnitude, by accounting for this size-related observational bias, is another important aspect of understanding the distribution of the NEAs.

This work seeks to provide a comprehensive description of the NEAs: their number, orbital distribution, compositional distribution, albedos, sizes, impact hazards, lunar cratering rates, and terrestrial cratering rates. A key theme is to account for the various observational selection effects that cause the catalog of known NEAs to differ from the true distribution. I first use the results of the LINEAR survey to estimate the number of NEAs as a function of absolute magnitude and orbital parameters, in Chapter 2. Chapter 3 addresses the question of observational selection effects in the observed NEA population in order to begin to describe the compositional distribution, albedos and sizes of the NEAs. This analysis is extended in Chapter 4, by combining Chapter 2's results with taxonomic and albedo data. This combination produces a description of the compositional distribution, albedo distribution and size (diameter) distribution of the NEAs. I use this new model of the NEA population in Chapter 5 to assess the hazard posed to the Earth from asteroid impacts. Chapter 5 also calculates the rate of crater formation expected from this NEA population model, and compares that with the observed cratering record on the Earth and Moon.

Chapter 2 An NEA Population Estimate From the LINEAR Survey[1]

2.1 Abstract

I estimate the number of near-Earth asteroids (NEA) and their orbital distributions using survey data from the Lincoln Near-Earth Asteroid Research (LINEAR) project covering 375,000 square degrees of sky and including more than 1300 NEA detections. A simulation of detection probabilities for different values of orbital parameters and sizes combined with the detection statistics in a Bayesian framework provides a correction for observational bias and yields the NEA population distribution as a function of absolute magnitude, semi-major axis, eccentricity, and inclination. The NEA population is more highly inclined than previously estimated, and the total number of NEAs with absolute magnitudes less than 18 is 1227^{+170}_{-90}.

2.2 Introduction

Because of the interest in NEAs, and primarily because of the risk of devastation from impacts, the US Air Force and MIT Lincoln Laboratory began the Lincoln Near-Earth Asteroid Research (LINEAR) project in 1996. NASA began contributing operational and developmental support to LINEAR in 1999. The LINEAR project evolved from a long and successful program of developing electro-optical space-surveillance technology to detect and catalog Earth orbiting artificial satellites. The advances those programs made in highly sensitive, large format, frame-transfer charge-coupled devices (CCDs), as well as the advances made in moving target detection algorithms, were naturally applied to the problem of discovering and cataloging NEAs. The LINEAR program operates with a Lincoln Laboratory developed, 2560x1960-pixel, frame-transfer CCD mounted on a 1-meter telescope from the U.S. Air Force ground-based electro-optical deep-space surveillance (GEODSS) system in Socorro, New Mexico. This telescope and CCD can achieve a limiting visual magnitude of 22 over a 2 square degree field of view with less than 100 seconds of integration time. During a long winter night, using a 10-second integration time, the system can image about 1200 square

[1] This chapter is an expanded version of: Stuart, J.S. A Near-Earth Asteroid Population Estimate from the LINEAR Survey, *Science* **294**, p.1691-1693, 23 Nov 2001. The results presented here are identical to the results in that paper. The descriptions and explanations have been expanded.

degrees of sky five times over (the moving target detection algorithm uses five images of the same field of view, over an interval of 2 hours, to detect asteroids). For further descriptions of the LINEAR project, see Viggh *et al.* (1998a, 1998b), and Stokes *et al.* (1998, 2000).

Since beginning full scale operations in 1998, LINEAR has been responsible for about 70% of the world-wide total number of asteroid detections, and NEA discoveries. It has discovered more than half of the currently known NEAs and has detected over 75% of the known NEAs. LINEAR has discovered nearly 5 times as many asteroids (including main-belt asteroids) as the next most prolific observatory. The large amount of data produced by LINEAR yields a significant advance in understanding the statistics of the NEA population.

2.3 LINEAR Survey Data

Because of the huge volume of data produced by the LINEAR CCD, the raw data from the searches were not archived until high-speed, large-capacity tapes became available in 2002. Instead, a summary of each night's observing is produced and stored. The summary contains a record for each field searched, including the computed visual magnitude for a star with a signal-to-noise ratio of 6 (SNR6). This number is obtained by selecting a few hundred solar-type stars from the USNO SA2.0 star catalog and using their cataloged magnitudes to calculate a color-corrected CCD magnitude. The CCD magnitude is defined as the V magnitude of a solar-type star that produces the same photoelectron generation rate in the unfiltered CCD sensor as the star does. The USNO SA2.0 provides calibrated B and R magnitudes that are converted to V magnitudes using a linear fit to (B-V) versus (B-R). The V magnitude is converted to a CCD magnitude by adding an offset that is determined by a blackbody spectrum for the star whose effective temperature is estimated from the catalogued B and R magnitudes (Rork 1998).

The CCD magnitude is converted to a signal flux with the equation $F = 10^{-0.4 M_{CCD}}$, where F is the expected flux, and M_{CCD} is the catalogued magnitude with color corrections to convert to CCD magnitude. This expected signal flux, for each star, F_i, is divided by the measured signal for that star, S_i, determined with a single pixel aperture. The typical seeing at the LINEAR site is 2" (full-width at half-maximum of the point-

spread function). The plate scale is 2".26 per pixel, so the single-pixel aperture captures about 60% of the photon flux, on average. The resulting gain ratios are linearly averaged to produce the average gain value for the image $\langle G \rangle = \frac{1}{L}\sum_{i=1}^{L} F_i/S_i$, where S_i is the measured signal from one of the stars, and L is the number of catalogued stars used. The average gain, $\langle G \rangle$, is the correction factor to convert CCD signal to expected (catalogued) flux and is used to calculate the magnitudes of stars and asteroids from the CCD measurements.

So if an asteroid has a signal level of S_a, using a single-pixel aperture, the reported magnitude for the asteroid is $M_{ast} = -2.5\log_{10}(S_a\langle G \rangle)$. The magnitude of a star with signal-to-noise ratio of six is calculated as $M_{SNR6} = -2.5\log_{10}(6\sigma\langle G \rangle)$, where σ is the spatially averaged, single pixel, RMS sky background noise for the image. M_{SNR6} is a good estimate for the faintest object that can be detected by the search system, and I will use this as the limiting visual magnitude for the search.

Unfortunately, during the time period in which the data for this analysis were collected, the SNR6 stellar magnitude was recorded for only the first of the five frames. On many nights, when the weather was variable, (Figure 2.1) the SNR6 stellar magnitudes fluctuate enough to make limiting magnitude determination uncertain. On the other hand, on many nights, the weather was more stable, and the SNR6 magnitudes were more constant, Figure 2.2. It seems reasonable to conclude that on the night illustrated in Figure 2.2 the weather was constant enough to assume that the limiting visual magnitude for the first image in each field is an acceptable expression of the overall limiting magnitude for the field. Recently, the telescope control software was modified to record SNR6 limiting magnitudes for every frame of all fields. These data confirm (Figure 2.3) that on nights when the first frame SNR6 magnitudes are steady, the intervening frames are similarly calibrated.

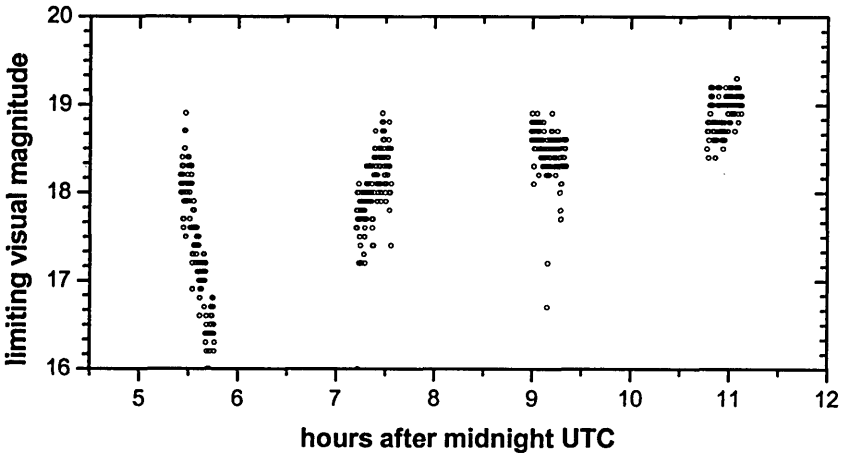

Figure 2.1Limiting Magnitudes for a Variable Night, Day 349, 1998. The limiting visual magnitudes for each field is plotted over the course of a single night. The limiting visual magnitude is calculated as the magnitude for an average SNR6 star, see text above for details of calculation. The SNR6 limiting visual magnitude was available for only the first of five frames. The extreme variability over the course of the night, due to changing weather conditions, makes it impossible to calibrate the frames for which the SNR6 limiting magnitude was not recorded. Nights with this sort of variability were not used in this analysis.

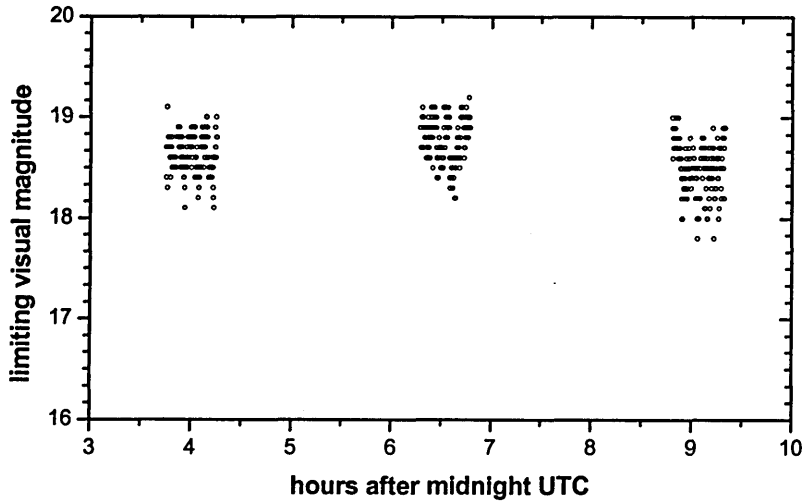

Figure 2.2 Limiting Magnitudes for a Consistent Night, Day 63, 1998. The limiting visual magnitudes for each field is plotted over the course of a single night. The limiting visual magnitude is calculated as the magnitude for an average SNR6 star, see text above for details of calculation. The SNR6 limiting visual magnitude was available for only the first of five frames. The weather on this night was reasonably consistent throughout the night, so the SNR6 limiting visual magnitude for the first of the five frames was assumed to be representative of the limiting visual magnitude for the remaining four frames in each block. The overall limiting visual magnitude for the night was estimated by averaging the limiting visual magnitude from the first frames.

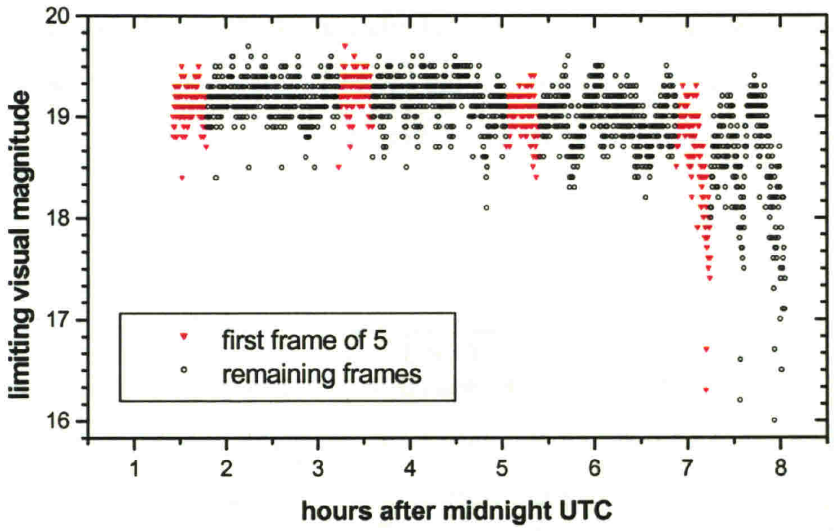

Figure 2.3 Limiting Visual Magnitude for a Night with All Frames Available, Day 335, 2002. The limiting visual magnitudes for each field is plotted over the course of a single night. The limiting visual magnitude is calculated as the magnitude for an average SNR6 star, see text above for details of calculation. Red triangles show the limiting visual magnitude for the first of the five frames in each field. The black dots show the limiting visual magnitude for the other four fields. Around 8:30 UTC, heavy clouds moved in so that only three frames were acquired for the last field. The limiting visual magnitudes for the intermediate frames (black dots) match the limiting visual magnitudes for the first frame of each block (red triangles). This validates the use of the first frame limiting visual magnitudes as a measure of the overall limiting visual magnitude for the night.

To test the validity of using the SNR6 limiting magnitude as the detection limit for NEAs, I compared the SNR6 limiting magnitude to the limiting magnitude derived from observations of main-belt asteroids. The catalog of numbered and multi-opposition main-belt asteroids from the Minor Planet Center was propagated to determine which asteroids should have been within the telescope search area each night, and how bright those asteroids were. The catalogued asteroids were compared with the detected asteroids. The ratio of detected asteroids to total expected asteroids within the field of view gives a direct measure of the detection efficiency of the sensor, as a function of apparent visual magnitude, for each night. I found that the SNR6 limiting magnitude, on average, matches the apparent visual magnitude at which main-belt asteroids have a 50% probability of being detected by the LINEAR moving-target detection algorithm (Figure 2.4). To test whether these two methods give statistically similar results, I used a paired t-test. The resulting t-statistic is 2.01, which has a p-value of 0.06 in a two-tailed

student's t distribution. Thus, the two methods produce results that are not statistically different. Because the limiting magnitudes determined from main-belt asteroids used the catalogued, V-band, absolute magnitude to calculate apparent visual magnitude, this comparison also validates the treatment of the SNR6 limiting magnitudes as visual magnitudes that do not need further color corrections.

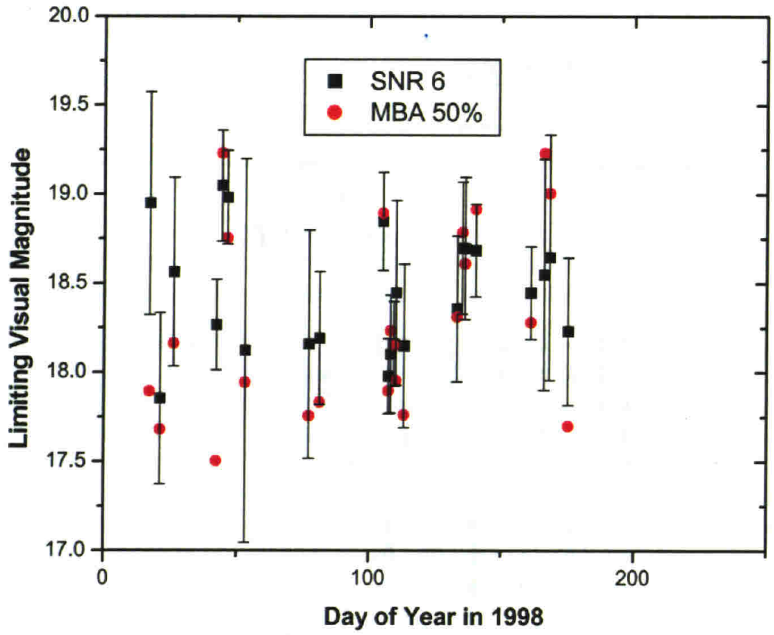

Figure 2.4 Comparison of Limiting Magnitude Calculations. Limiting visual magnitudes, as calculated by two different methods are shown for 23 nights. The red circles give the limiting visual magnitude for each night as determined by the apparent visual magnitude at which main-belt asteroids had a 50% probability of detection on each night. The black squares are the limiting visual magnitude calculated as an average of stars with signal-to-noise ratios of 6 (see text above for further description). The error bars plotted with the SNR 6 values give the one standard deviation variability between fields on each night. On average the two methods give similar results. Using a paired t-test, the difference between the two methods is not statistically significant at the 5% level ($t = 2.01$, $p=0.06$).

Most asteroids are not spherical bodies, and an asteroid's brightness will change as the asteroid rotates and presents changing cross-sectional area to the observer. This effect can be studied by measuring the changing brightness of an asteroid through several rotation periods to compile a rotational lightcurve (*e.g.* Slivan 1995). Rotational lightcurves have not been measured for most of the NEAs detected by LINEAR. This introduces an additional uncertainty into the calculation of an asteroid's absolute magnitude from its observed brightness. Because of a lack of knowledge of the rotational

states of most NEAs, no attempt has been made to account for the effect of rotational lightcurve variation.

There is a disadvantage to using the main-belt asteroids as the primary method of determining the limiting magnitude each night. On many nights, there aren't enough main-belt asteroids within the search area to make the calibration. The density of main-belt asteroids falls rapidly with increasing ecliptic latitude. For fields more than 30 degrees away from the ecliptic plane, there are rarely enough main-belt asteroids to determine the limiting magnitude. NEAs are detected at higher ecliptic latitudes than main-belt asteroids, primarily because of their proximity to Earth, and also because they tend to have higher orbital inclinations. Part of the power of the LINEAR data is that observations are taken over the entire sky, not just in the ecliptic. In order to be able to use some of this high latitude data, I use the SNR6 limiting magnitude rather than the main-belt asteroids to calibrate the limiting magnitude in my population estimates.

For each of the nights with consistent atmospheric transparency (as in Figure 2.2) the SNR6 limiting magnitudes are averaged together to define a single limiting magnitude for the night. The data from hundreds of nights are then combined together (as described below) to determine long-term detection efficiency. Thus, variation of the limiting magnitude within a night, and random errors in determining the limiting magnitude for an individual night are averaged out over hundreds of nights and have very little effect on the final estimate of the NEA population. However, if there is a systematic bias that causes the limiting magnitude to be over- or under-estimated every night, then that would potentially have a large effect on the final NEA population estimate. This potential source of bias has been included in the uncertainty estimates by simulating the effects of increasing or decreasing all of the nightly limiting magnitudes by 0.1 magnitudes. This level of systematic bias in the limiting magnitude calculation results in a 7% uncertainty in the final population estimates, and that uncertainty has been added in quadrature with the Bayesian error estimates described below.

The calculation of limiting magnitude does not account for trailing losses. The telescope tracks at sidereal rate to keep the background stars from moving across the CCD during an image. An object moving relative to the stars will therefore move across

the CCD during an image, spreading its signal over multiple pixels. The signal strength in any one pixel will thus be reduced, an effect termed trailing loss. However, each pixel on the LINEAR CCD subtends 2.26 arcseconds, and the maximum integration time that LINEAR uses is about 10 seconds. That means that an NEA must be moving faster than 5° per day to move one pixel during the longest images. About 1% of the NEAs that LINEAR detects are moving faster than 5° per day. The trailing losses for LINEAR are thus minor. If a model for trailing losses were included in this analysis it would tend to increase the resulting estimate of the number of NEAs, though not significantly.

In three years of operation starting in March 1998, and ending February 2001, the LINEAR project searched almost 500,000 square degrees of sky on nearly 600 nights, discovering 657 new NEAs and over 110,000 new main-belt asteroids. After examining plots similar to Figure 2.2, and selecting only those nights on which the limiting visual magnitudes were reasonably consistent, I was left with 412 usable nights. The limiting magnitudes on those 412 nights range from 13.0 to 20.3 with 99% in the range 15 to 20. The accepted nights covered more than 375,000 square degrees of sky, and included 1343 detections of 606 different NEAs. The total sky coverage is depicted in Figure 2.5.

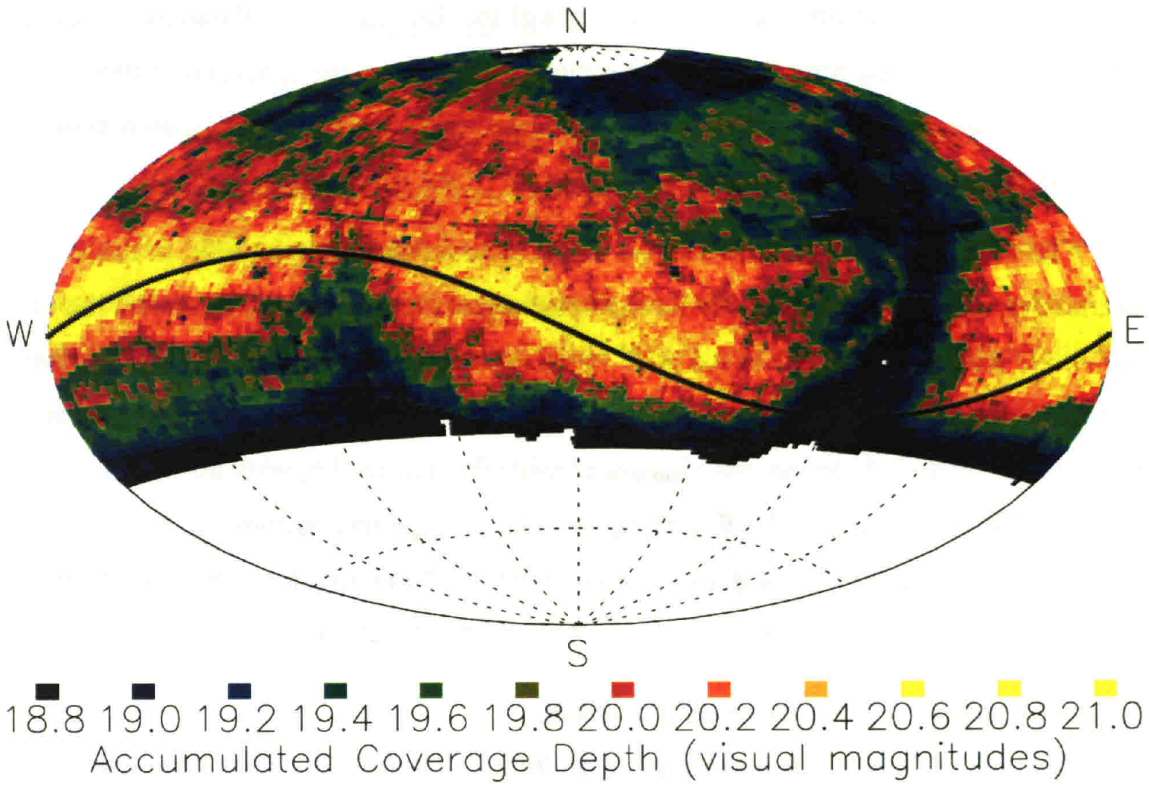

Figure 2.5 Sky Coverage. An equal-area projection of the entire celestial sphere in right ascension, and declination coordinates showing the area coverage and accumulated depth of the LINEAR survey data used in this analysis. The ecliptic plane is plotted in black for reference. More than 375,000 square degrees of sky were surveyed from March 1998 through February 2001. Since the moving target detection algorithm uses five images of the same field to detect moving asteroids, this represents nearly 2 million square degrees of sky imaged. The color-coded accumulated depth is the equivalent limiting magnitude from combining multiple searches of each field. The SNR6 limiting magnitude for each field is converted to an equivalent integration time by assuming that the signal to noise ratio is proportional to the square root of the integration time. The equivalent integration times are then summed for all of the nights on which LINEAR searched a given field. The summed equivalent integration times are then converted back into astronomical magnitudes. This figure appears as Figure 1 of Stuart (2001).

2.4 Debiasing Technique

To estimate the size and nature of the asteroid population from the available observational data, I must remove the observational biases from the data. The search program preferentially detects asteroids that are bright in the sky over New Mexico on nights when the search is operating. Thus, a complicated combination of an asteroid's intrinsic brightness and orbital parameters, along with the telescope properties and weather in New Mexico determine whether any given asteroid is likely to be detected. To account for observational bias, I begin by defining a four dimensional parameter space in which near-Earth asteroids may be placed. I then use the pointing history of the telescope, the nightly limiting magnitude, and the laws of orbital dynamics to estimate the

probability of detection for asteroids in all parts of the four-dimensional parameter space. This probability of detection for different regions of the parameter space, combined with the actual number of asteroid detections in each part of the parameter space, then allows me to estimate the number of asteroids in each part of the parameter space.

The four dimensional space consists of the asteroid's semi-major axis, *a*, its eccentricity, *e*, its inclination, *i*, and its absolute magnitude, *H*. In the *a* direction, the bins are 0.1 AU wide from 0.6 AU to 3.6 AU. In the *e* direction the bins are 0.1 in width from 0.0 to 1.0. Bins with *a-e* values that do not meet the definition of NEA are excluded from the analysis. In the *i* direction, the bins are 5° wide from 0° to 50°, with the last bin extending to 180° to include the few objects with very large inclinations. In the *H* direction, the bins are 0.5 magnitudes wide from 11 to 23 magnitudes. The *a-e-i-H* space was thus divided into 49,200 bins.

2.5 Detection Probability Analysis

With the *a-e-i-H* space divided into a multitude of bins, I determined, for each bin, the probability that an asteroid with the specified values of *a, e, i,* and, *H*, would have been detected by the LINEAR search. In order to fully specify an asteroid orbit, one needs to specify, in addition to *a, e,* and *i*, three angles: the longitude of the ascending node, the argument of perihelion, and the mean anomaly (Ω, ω, *M*). It is widely believed that, for the total population of near-Earth asteroids, those three angles are uniformly distributed between 0 and 2π. Given the perturbations that occur because of planetary encounters in the inner solar system, and the relative ease by which these angles are altered, there is no plausible mechanism by which any of these three parameters would become non-uniformly distributed. So, to determine the probability of detection of an asteroid in a particular *a-e-i-H* bin, I averaged over the other three orbital parameters assuming a uniform probability distribution for Ω, ω, and *M*.

For each *a-e-i* bin, 200 ellipses were generated by randomly selecting 200 values of argument of perihelion and longitude of the ascending node. All were assigned *a-e-i* values for the center of the bin. For each of these 200 ellipses, 720 test particles were placed on the ellipse at every half degree of mean anomaly. All of these test particles are then propagated, by a two-body propagation algorithm, to every night that the telescope

searched. The solar phase function and the heliocentric and geocentric distances are computed to find the difference between absolute magnitude and apparent visual magnitude. The locations of the test particles are checked against the pointing history from the LINEAR telescope. Any time a test particle falls within the field of view of the telescope, the limiting magnitude for that night, along with the observing geometry for the test particle, is used to determine the faintest absolute magnitude (largest value of H) that would be detectable in that telescope field. If the maximum absolute magnitude, H, for the new detection is fainter than the currently recorded detection threshold, then the record is updated to the new H. All 720x200 test particles in a single *a-e-i* bin are compared against the pointing history for all of the nights. At the end, each test particle had a limiting absolute magnitude indicating that anything brighter than that value (smaller H) should have been detected by the search. This analysis is depicted in Figure 2.6.

After performing this simulation for each *a-e-i* bin, I calculate what fraction of the 720x200 pseudo-asteroids would have been detected for the value of H associated with each of the H bins. These numbers are the probabilities of detection for each *a-e-i-H* bin. If for example, an *a-e-i-H* bin ends up with a probability of detection of 20%, this implies that, had there been a single real asteroid with the given values of *a-e-i-H,* then our search would have had a 20% chance of detecting it.

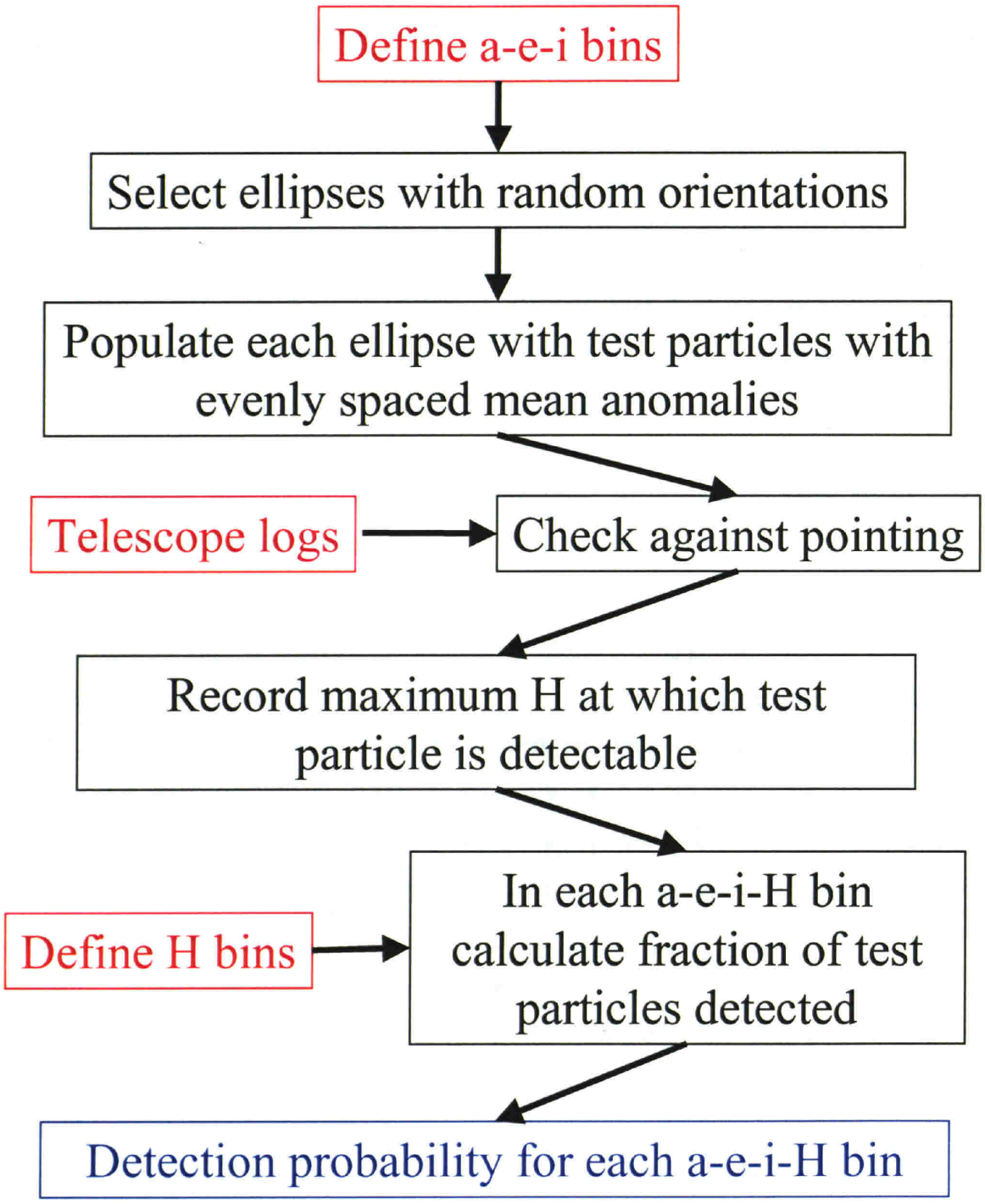

Figure 2.6 Flowchart for Detection Probability Analysis. Shows the steps in calculating the detection probability for the LINEAR data used in estimating the NEA population. Inputs are in red, outputs are in blue, and processes are in black.

2.6 Debiasing

For each of the 49,200 bins in *a-e-i-H* space, I estimate the value of N, the true number of NEAs in the bin. Using a binomial statistical model with N asteroids, and detection probability p, the probability distribution for the number of detections x, is a binomial distribution

$$P_{N,p}(x) = \binom{N}{x} p^x (1-p)^{N-x}. \tag{2.1}$$

The quantity x/p is an unbiased estimator of the number of asteroids, N. Thus, my estimate for the total number of NEAs in any of the bins is $\langle N \rangle = x/p$, where x is the observed number of NEAs in a bin, and p is the detection probability calculated in each *a-e-i-H* bin.

I also need to determine the uncertainty in the estimate of the number of NEAs in each bin. We can treat equation (2.1) as a likelihood function for the true number of asteroids in a bin, and use Bayes' Law to convert it to a posterior distribution for the number of NEAs in a bin:

$$\mathrm{Po}(N) = \frac{\sum_{N=0}^{\infty} \binom{N}{x} p^x (1-p)^{N-x} \Pr(N)}{\sum_{N=0}^{\infty} \Pr(N)} \tag{2.2}$$

$\Pr(N)$ is the prior probability distribution function for N, and $\mathrm{Po}(N)$ is the posterior probability distribution function for N. In a Gaussian distribution, one standard deviation around the mean encompasses about 68% of the integrated probability. To determine a similar uncertainty value for the posterior PDF for N given in equation (2.2), I find the points above and below the estimator $\langle N \rangle$ such that about 68% of the probability from equation (2.2) is contained between them, and label those points N_U and N_L. N_U can be thought of as the largest number of NEAs that could actually exist in the bin and still allow my estimate, $\langle N \rangle$, to be within one standard deviation of the true value given the binomial statistical model in equation (2.1). This defines an upper and lower one standard deviation uncertainty as $N_U - \langle N \rangle$, and $\langle N \rangle - N_L$. The uncertainties are added in quadrature when adding together the number of NEAs in multiple bins to obtain the total number of NEAs.

The prior distributions that I use start as Gaussian distributions that specify the number of NEAs as a function of absolute magnitude. First, two absolute magnitude distributions were defined: a "lower" cumulative distribution $C_L(<H) = 10^{-3.5+0.35H}$, and an "upper" cumulative distribution $C_U(<H) = 10^{-4.3+0.42H}$. The lower cumulative distribution sets the number of NEAs with H<18 at 630, while the upper cumulative distribution sets the number of NEAs with H<18 at 1819. These two cumulative distributions are converted to incremental distributions in the same 0.5 magnitude wide bins as used above, so that each H bin has a lower value and an upper value assigned to it. The prior distribution for each H bin is then defined as a Gaussian distribution whose mean is midway between the lower and upper value, and whose standard deviation is half the difference between the lower and upper value. In H bins where the Gaussian distribution would place a significant fraction of its power at unphysical values corresponding to a negative number of asteroids, a Poisson distribution is convolved with the Gaussian distribution to obtain a prior distribution with the desired mean but with no power at negative values. The resulting prior distributions are used to determine uncertainties, but do not affect the value of $<N>$.

In principle, a fully Bayesian analysis could be performed using equation (2.2) to define the posterior distribution for the number of NEAs in each bin, and using the maximum *aposteriori* estimator as the estimate for the number of NEAs in the bin. Summing bins would be performed by convolving together the posterior distributions for those bins. This results in a problem, however. The binomial likelihood function, and therefore the posterior distributions in equation (2.2), have means that are always greater than zero, even when there are no detections in a bin. When the posterior distributions are convolved together to sum the bins, the means add. After summing several bins the Law of Large Numbers drives the convolved posterior distributions to become nearly Gaussian with the maximum *aposteriori* estimator becoming very close to the mean of the posterior distribution. Thus, summing together many bins with no detections would result in a very large estimate for the total number of NEAs. If the bin size were decreased, the resulting estimate for the number of NEAs would increase linearly with the number of bins even though no new detections were made. This runaway process in

the posterior distributions can be controlled only by selecting very tightly constrained prior distributions. But then, the actual observations have very little effect on the final answer since it is controlled primarily by the prior distribution. The method I use here is equivalent to using the maximum likelihood estimator, and simply summing the maximum likelihood estimators when combining bins. That is because the unbiased estimator defined above is equivalent to the maximum likelihood estimator for a binomial likelihood function.

When the binomial distribution in equation (2.1) is used as a likelihood function, there is an asymmetry around the unbiased estimator, $<N>$. The asymmetry is preserved by Bayes' Law to produce an asymmetrical *aposteriori* probability distribution function. When the uncertainties are determined for the number of NEAs in a bin, this asymmetry causes the upper uncertainty value $N_U - <N>$ to always be larger than the lower uncertainty value $<N> - N_L$. The one standard deviation uncertainties are always larger on the upper side than on the lower side. This is a natural consequence of using a binomial statistical model. In essence it says that it is more likely that the number of NEAs in a bin is larger than we think and we happened to miss more than expected in the present experiment than that the number of NEAs in a bin is small and we happened to find more than expected.

2.7 Absolute Magnitude and Orbital Element Distributions

With an unbiased estimate of the number of NEAs in each *a-e-i-H* bin, I could, in principle, provide a full 4-dimensional map of the asteroid population. However, because there are more bins than asteroids, the number of detections in any given bin is small (either 0 or 1 in almost all cases), so the noise in the estimates for individual bins is large. However, by summing over any three of the dimensions, I obtain an estimate of the distribution over the fourth parameter with robust statistics (no fewer than 20 detections per 1-dimensional bin).

The number of NEAs as a function of absolute magnitude is shown as a binned, non-cumulative distribution in Figure 2.7, and as a cumulative distribution in Figure 2.8. The estimated number of NEAs with $H<18$ is 1227^{+170}_{-90}. Much of the literature on asteroid population estimates assumes an exponential form for the number of NEAs as a

function of absolute magnitude. To compare with that body of work, I fit a straight line to the logarithm (base 10) of the non-cumulative *H* distribution (Figure 2.7). The non-cumulative best fit line is $N(H)=10^{-4.33+0.39H}$, where N(H) represents the number of NEAs in the bin of width 0.5 whose upper limit is H. The linear least-squares fit for the offset is –4.33±0.22, and for the slope is 0.39±0.013. Translating the non-cumulative fit to a cumulative distribution yields a fit of $N(<H)=10^{-3.88+0.39H}$. The latter is the straight green line shown in Figure 2.8.

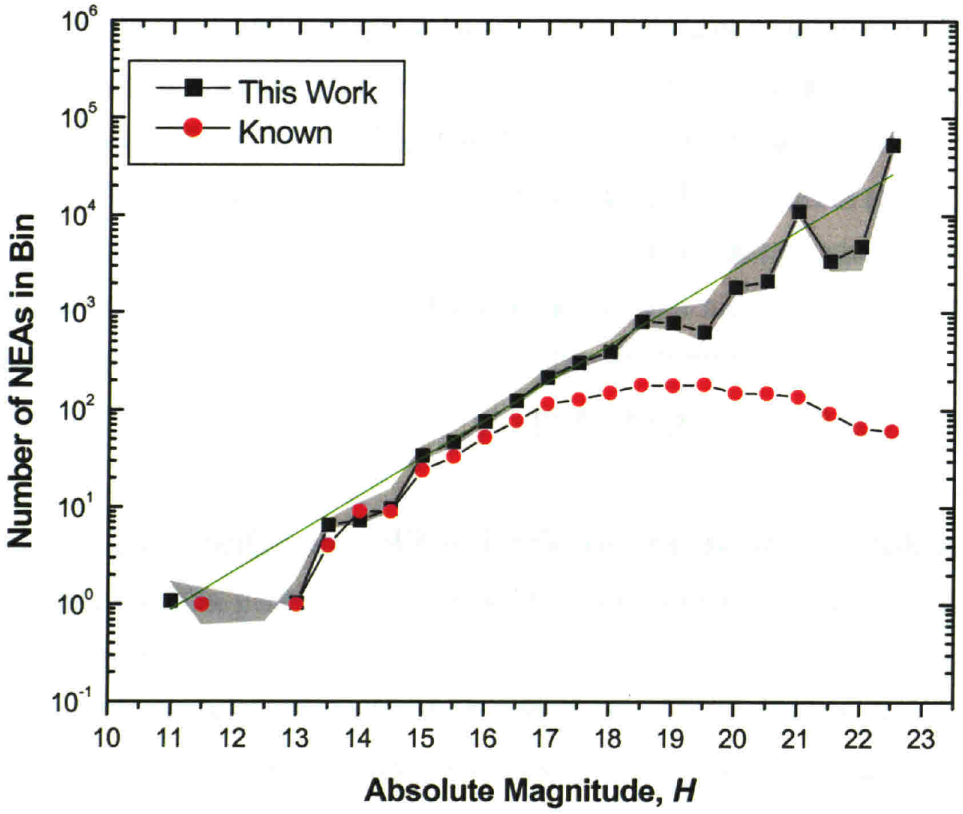

Figure 2.7 Non-Cumulative Absolute Magnitude Distribution of the NEAs. The number of NEAs, as estimated in this work, versus absolute magnitude is shown as black squares. The grey shaded region indicates the one-standard-deviation error envelope. The number of known NEAs (as of 18 April 2003) are shown as red circles. The bin size is 0.5 magnitudes, and points are plotted at the top of the bin (that is the bin from 17.5 to 18 is plotted at 18). The green line is a linear-least-squares fit to the base 10 logarithm of the estimated number of NEAs in the bins from 14.5<H<18.5. The equation for the line is $N(H)=10^{-4.33+0.39H}$

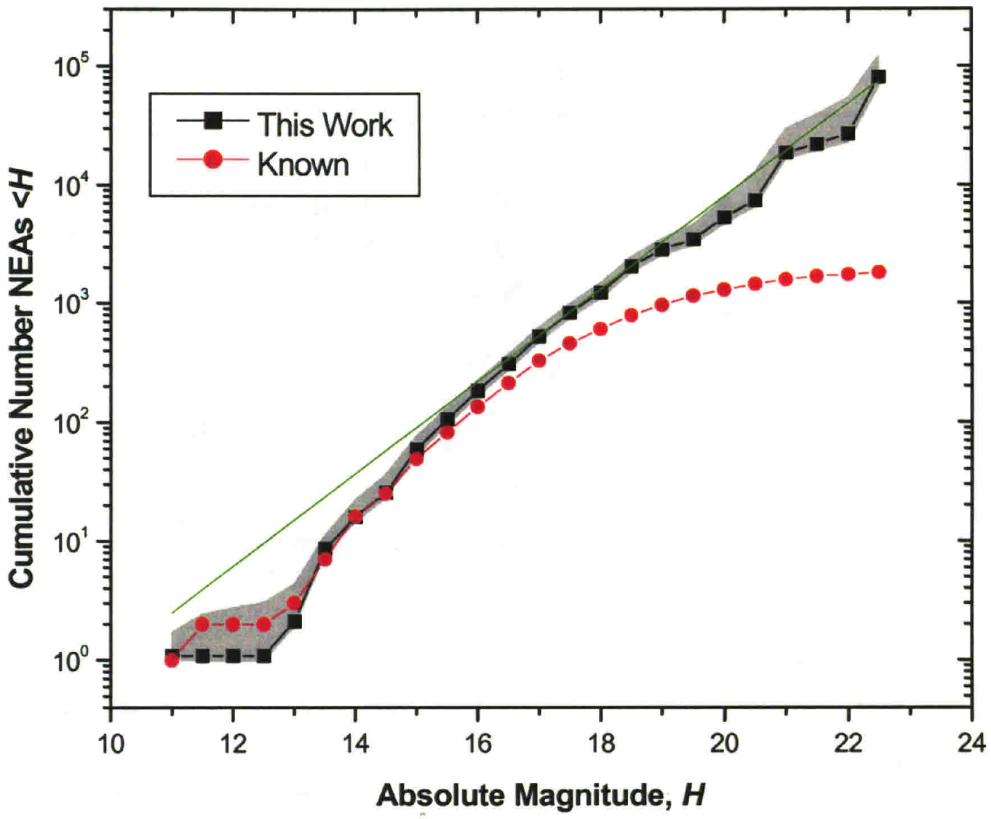

Figure 2.8 Absolute Magnitude Distribution of the NEAs. The cumulative number of NEAs, as estimated in this work, with absolute magnitudes brighter than H is shown (black squares). The grey shaded region around the curve indicates the 1σ error envelope. For comparison, the absolute magnitude distribution of the known NEAs (as of 18 April 2003) is shown as red circles. The green line without symbols shows the same exponential function as in **Figure 2.7**, but converted to a cumulative distribution. The equation for the line is $N(<H) = 10^{-3.88 + 0.39H}$. (433) Eros and (1036) Ganymed are the only two NEAs with $H<13$. The LINEAR data used in this survey happened to find Eros, but not Ganymed. That is why the estimated population is lower than the known population at $H<13$. This figure is adapted from Figure 2 of Stuart (2001).

The projection of the estimated number of NEAs onto the inclination dimension of the *a-e-i-H* space is shown in Figure 2.9. The *a-e-i-H* space is collapsed into one dimension by summing the estimated number of NEAs in each bin (<*N*>) over the *a*, *e*, and *H* dimensions. In the *H* dimension, only the bins up to $H<18.5$ have been included in the sum. This is to allow the inclination distribution to reflect just the large NEAs while including the bins with the most detections. For the data used in this analysis, more

detected NEAs fell into the bin 18.0<H<18.5 than any other H bin (70 out of 606 detected NEAs had 18.0<H<18.5, and 341 detected NEAs had H<18.5).

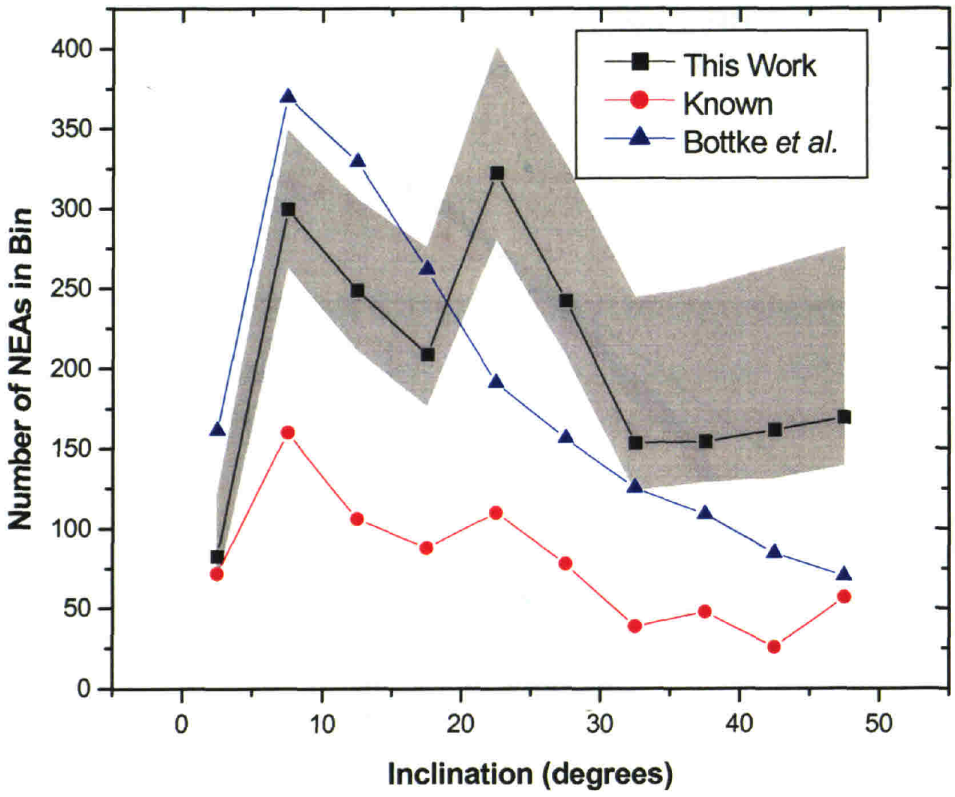

Figure 2.9 Inclination Distribution of the NEAs. The number of NEAs with H<18.5, as estimated in this work, is shown as a function of orbital inclination (black squares). The shaded region indicates the 1σ error envelope for the estimate. The NEA inclination distribution as estimated by Bottke *et al.* (2000, 2002) is plotted as blue triangles, and the currently known population (as of 18 April 2003) is shown as red circles. All three curves are plotted with a bin size of 5°, and in all three curves, the last bin (at inclination of 47.5°) contains all of the NEAs with inclinations greater than 45°. The curve from the Bottke *et al.* distribution has been renormalized so that the total number of NEAs under the blue curve is the same as the total number of NEAs under the black curve. This figure is adapted from Figure 3 of Stuart (2001).

The marginal distribution over semimajor axis is given in Figure 2.10. The semimajor axis distribution is computed in the same manner as the inclination distribution, summing over the e, i, and H dimensions. The estimated distribution is similar to the distribution of known NEAs with some enhancement at semimajor axes larger than 2 AU. That enhancement is due to the simple observational selection effect that NEAs with semimajor axes beyond 2 AU spend a lot of time far away from the Earth

and are thus fainter. The spikiness in the semimajor axis distribution below 2.5 AU is not statistically significant. A smoother looking distribution can be fit to the given distribution with acceptable χ^2 values. The lack of corresponding spikes and dips in the distribution of known NEAs leads to the conclusion that the spikiness of the estimated distribution is probably not real.

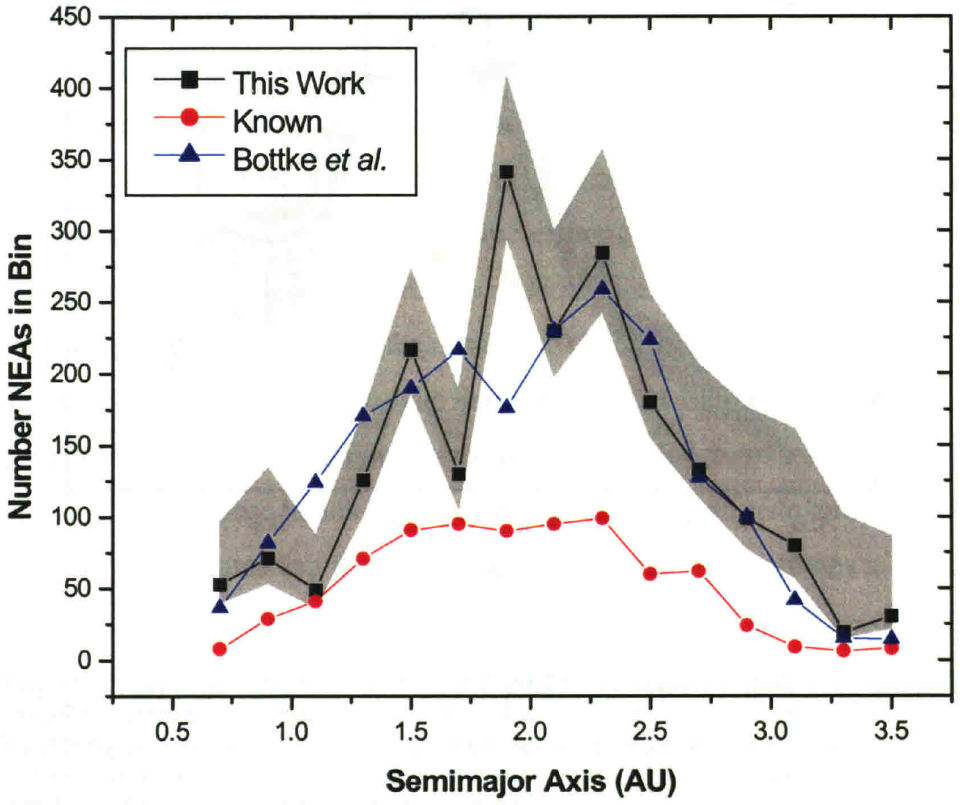

Figure 2.10 Semimajor Axis Distribution of the NEAs. The number of NEAs with H<18.5, as estimated in this work, is shown as a function of semimajor axis (black squares). The shaded region indicates the 1σ error envelope for the estimate. The NEA semimajor axis distribution as estimated by Bottke *et al.* (2000, 2002) is plotted as blue triangles, and the currently known population (as of 18 April 2003) is shown as red circles. All three curves are plotted with a bin size of 0.2 AU. The curve from the Bottke *et al.* distribution has been renormalized so that the total number of NEAs under the blue curve is the same as the total number of NEAs under the black curve. This figure is adapted from Figure 3 of Stuart (2001).

The marginal distribution of the NEAs over eccentricity is shown in Figure 2.11. The eccentricity distribution is calculated the same way as the inclination distribution, summing over the a, i, and H dimensions. As with the semimajor axis distribution, the

eccentricity distribution is similar to the known distribution and the estimate of Bottke *et al.* (2000, 2002).

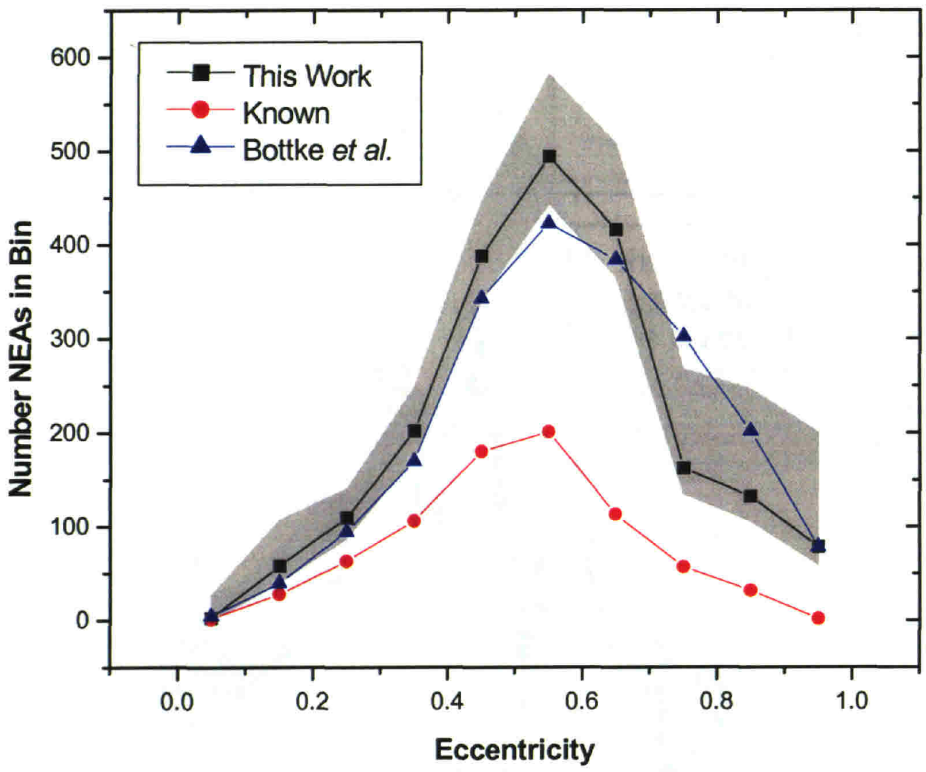

Figure 2.11 Eccentricity Distribution of the NEAs. The number of NEAs with H<18.5, as estimated in this work, is shown as a function of eccentricity (black squares). The shaded region indicates the 1σ error envelope for the estimate. The NEA eccentricity distribution as estimated by Bottke *et al.* (2000, 2002) is plotted as blue triangles, and the currently known population (as of 18 April 2003) is shown as red circles. All three curves are plotted with a bin size of 0.1. The curve from the Bottke *et al.* distribution has been renormalized so that the total number of NEAs under the blue curve is the same as the total number of NEAs under the black curve. This figure is adapted from Figure 3 of Stuart (2001).

2.8 Comparisons to Other NEA Population Estimates

In recent years, two other estimates of the NEA population have been published based on detections from automated surveys. Rabinowitz *et al.* (2000) used 34 NEA detections made by the Near-Earth Asteroid Tracking project, and a Monte-Carlo simulation to correct for the effects of observational bias. The input to the Monte-Carlo simulation was randomly generated populations of asteroids with orbital parameter distributions that match a debiased population estimate based on Spacewatch data

(Rabinowitz 1993). That estimate predicted the existence of 750 +/- 250 NEAs with $H<18$. The inclination distribution used in that analysis was quite different from the inclination distribution derived here in that it assumed far fewer NEAs at inclinations near 25° and far fewer with inclinations greater than 40°. To test whether the difference between the size of the NEA population predicted here (~1250) and that predicted by Rabinowitz (~750) is due to the differences in the distribution over the orbital elements, I constrained my population model to match the known NEAs in their distributions over *a*, *e*, and *i*, and allowed the model to vary the number of NEAs as a function of absolute magnitude. This was done by averaging together the detection probabilities from the Monte Carlo simulation using weights in each *a-e-i* bin proportional to the number of NEAs with $H<18$ in the bin. Thus, the four dimensional parameter space of *a-e-i-H* was collapsed to a one dimensional space in *H* by assuming that the distribution over *a*, *e*, and *i* matches the known population. Estimates of the number of NEAs in each *H* bin were then obtained as before by dividing the number of detections in the *H* bin by the averaged detection probability for that *H* bin. The number of NEAs in the *H* bins below 18 were then summed. Using this constraint, my model predicts that there are 780 ± 75 NEAs with $H<18$. The very close match between this constrained estimate and the estimate by Rabinowitz *et al.* indicates that the difference between the two estimates is caused by the different distributions of the orbital elements.

The data from the LINEAR survey has been analyzed by other researchers to estimate the number of NEAs as a function of absolute magnitude. D'Abramo *et al.* (2001) applied a simple probabilistic model to the number of new discoveries and serendipitous detections of previously discovered NEAs made by LINEAR in 1999. The basis of this model is to assume that within a small range of absolute magnitude (D'Abramo *et al.* used 0.5 magnitude bins, as do I) the probability of discovering any particular new NEA is the same as the probability of serendipitously redetecting any particular known NEA. Thus, the detection efficiency within each magnitude bin is the number of redetections divided by the number of previously known NEAs in that bin. The total number of asteroids in a bin is then the number of previously known NEAs plus the number of new discoveries divided by that detection efficiency. This method was also used by Shoemaker *et al.* (1990) as a "sanity check" for a more elaborate debiasing

method. D'Abramo *et al.* estimated that there are 855±101 NEAs with absolute magnitudes brighter than 18. This is substantially lower than the number found here. The method used by D'Abramo *et al.* assumes that the NEAs that have not yet been discovered are as easy to detect as NEAs that have already been discovered. However, this is not the case. NEAs on some types of orbits, particularly high inclination orbits, are more difficult to discover than others, and those that are easier to discover tend to get discovered first. Thus the detection efficiency for new discoveries is lower than the detection efficiency for redetections, even if the survey is not performing targeted follow-ups. By assuming that the detection efficiencies are the same for new NEAs and for redetections, the D'Abramo *et al.* method implicitly assumes that the distributions of orbital elements of undiscovered NEAs matches the distribution of orbital elements of the known NEAs. Because of this, the method used by D'Abramo *et al.* can only be considered a lower limit to the number of NEAs.

Bottke *et al.* (Bottke 2000, 2002) examined the dynamical mechanisms that remove asteroids from the main asteroid belt and deposit them into the inner solar system. They estimated the fraction of time that asteroids from each of four different source regions would spend in various portions of the *a-e-i* parameter space. By matching that analysis against observational data from the Spacewatch telescope, Bottke *et al.* estimated the fraction of the NEA population due to each of the three source regions and the total size of the population. Their analysis predicted that there are 910±120 NEAs with $H<18$, substantially fewer than estimated here. The semimajor axis and eccentricity distribution obtained here match the Bottke *et al.* distributions reasonably well (Figure 2.10 and Figure 2.11). The inclination distribution estimated by Bottke *et al.* was significantly depleted in inclinations near 25° and greater than 40° (Figure 2.9) compared to my estimate. The four source regions that control the distribution of orbital elements in their analysis do not produce inclinations as high as those estimated by this study. Again, this difference in the inclination distribution, combined with the difficulty in finding high inclination NEAs, explains the discrepancy in the number of NEAs with $H<18$. Two classes of asteroids in the main belt, the Hungarias, and the Phocaeas, have inclinations near 25° and could produce NEAs with high inclinations when perturbed into near-Earth orbits (Migliorini *et al.* 1998). Bottke *et al.* (Bottke, personal communication 2002) are

presently expanding their analysis to include Hungarias and Phocaeas. Perhaps with the addition of the new source of high inclination objects, Bottke's inclination distribution will agree with the one presented here.

Shoemaker published an estimate of the NEA population (Shoemaker *et al.* 1990) that was based on a combination of observational data from the Palomar Survey and counts of the number of craters on the Moon (Shoemaker 1977). Shoemaker's estimate puts the number of NEAs with $H<18$ at around 1500 objects with poorly defined but presumably fairly large error bars. That roughly agrees with this estimate.

The population estimate presented here was published in 2001 (Stuart 2001), and the results were used by Harris (2002) to estimate the number and impact frequency of smaller objects, in the size range thought to have caused the Tunguska impact. Harris estimated the relative number of NEAs in bins of 0.5 absolute magnitudes from $21.5<H<25.5$. He then normalized his population estimate in the two largest size bins to the number given in this work to convert his relative numbers to an absolute estimate of the number of small NEAs. He also calculated expected impact rates for those NEAs. The Tunguska impact is thought to have been an asteroid in the range of H=24-24.5. Harris determined that there are roughly a half million NEAs in that H bin, and that impacts of those NEAs should occur approximately once every 1000 years.

Extending the size distribution of NEAs to even smaller sizes is the work of Brown *et al.* (2002). They used United States Department of Defense and Department of Energy satellites designed to detect nuclear explosions to determine the rate of impact into the Earth's atmosphere of small NEAs in the range of 1-10m (approximately $28<H<33$). Brown *et al.* report that a single exponential function (i.e. a straight line on a log-log plot such as Figure 2.8) matches the size distribution of their estimated flux of small impactors, and, when extended to larger sizes, matches the estimates in this work in the range $22.5<H<20$. Brown *et al.* also note that the same exponential size distribution nicely fits the number of impactors near 0.1 m (approximately H=38) as estimated by the meteoroid fireball counts from a network of Canadian fireball cameras (Halliday 1996). At those sizes, the size distribution is significantly steeper than the straight line fit presented here for $14<H<18.5$.

2.9 Conclusions

I have combined the largest existing set of NEA detections from a single survey with a model of observational bias effects to estimate the number of NEAs as a function of absolute magnitude, semimajor axis, eccentricity, and inclination. The estimated population matches other estimates in the distributions over semimajor axis and eccentricity, but predicts significantly more NEAs at high inclinations than other estimates. These high inclination NEAs may point to a significant contribution to the NEA population from the Hungaria and Phocaea asteroid families. The number of NEAs with absolute magnitudes less than 18 is 1227^{+170}_{-90}, higher than other recent estimates.

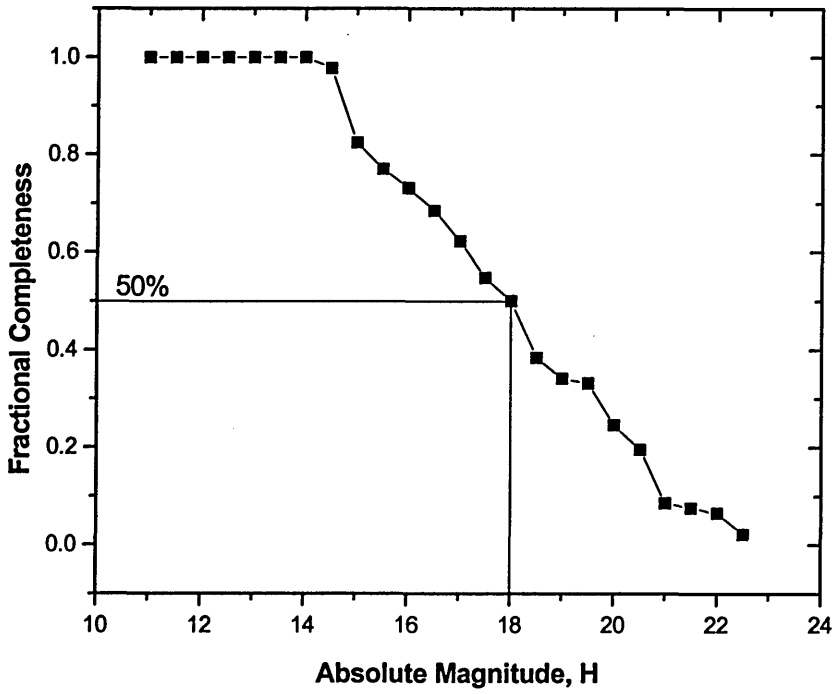

Figure 2.12 Fractional Completeness of NEA Catalog. Using the cumulative number of NEAs versus absolute magnitude (**Figure 2.8**), and the MPC catalog of NEAs known as of 18 April 2003, the cumulative completeness of the catalog is determined. About half of the NEAs with $H<18$ have been discovered.

As of 18 April 2003, the Minor Planet Center lists 613 known NEAs with $H<18$. Thus, the current catalog of NEAs is about 50% complete for NEAs with $H<18$. The current catalog is apparently complete, to within a few asteroids, for $H<14.5$. The

fraction of the NEAs that have already been discovered for each absolute magnitude bin is shown in Figure 2.12.

As the LINEAR Project continues to scan the skies in the next several years, more data will become available to refine these estimates. The system has recently begun to record, for every search field, several photometric parameters in addition to the SNR6 limiting magnitude used here. That information should help to refine the estimates of the limiting magnitude and to ensure that there is no systematic bias in the determination of the detection efficiency of the system. The inevitable increase in the sheer number of detections will improve the statistical accuracy of the population estimates. More detections may also allow for characterization of the NEA population at higher inclinations (beyond 50°) and at fainter absolute magnitudes.

Chapter 3 Albedo Bias in NEA Discovery.

3.1 Abstract

In this Chapter, I analyze a simple model of NEA discovery bias. The NEAs are divided into two categories mirroring a coarse taxonomy of main-belt asteroids that divides them into high albedo S-types and low albedo C-types. The observational bias that results from a magnitude-limited discovery survey is expressed as the ratio of discovered S-types to discovered C-types. The contributions to this bias from the albedos and solar phase functions of the two classes of NEAs, and from the overall completeness level of the discovery survey is discussed. I find that this simple model of NEA discovery bias cannot be applied to current NEA survey programs and I develop another model based on the NEA orbital distributions presented in section 2.7.

3.2 Introduction

Like the main-belt asteroids, the NEAs display a diversity of surface reflectance properties (e.g. Gradie and Tedesco 1982; Bus and Binzel 2002b). Reflectance spectroscopy of asteroids has been used since the mid-1960s to classify the asteroids into groupings (Wood and Kuiper 1963, Chapman *et al.* 1971). The groupings were eventually formalized into taxonomic systems. The taxonomies initially comprised a few broad classes (Chapman *et al.* 1975). Thanks to improvements in technology (primarily CCD spectrographs) and to a larger sample of measured asteroids that shows more diversity, the taxonomies have expanded over the years to more finely describe the spectral characteristics of the asteroids (Tholen 1984, Bus 1999).

A telescope survey that detects NEAs down to some limiting magnitude (such as LINEAR) will be able to detect smaller NEAs if they have higher albedos and more favorable phase functions than if the NEAs have lower albedos and more severe darkening at high phase angles. Since the number of asteroids increases rapidly at smaller sizes, there is a substantial bias toward finding more NEAs with higher albedos and more favorable phase functions. To understand the relative proportions of the various taxonomic classes among the NEAs, and to determine the number of NEAs as a function of diameter, one must first account for the observational selection effects that favor the discovery of higher albedo asteroids.

Further observational bias in asteroid discovery can be attributed to phase angle effects. Two asteroids with the same value of absolute magnitude, *H,* but different values of phase slope parameter, *G*, will have the same apparent brightness at zero phase angle (the *H*, *G* photometric system is described in Appendix A.1). However, the asteroid with lower *G* will appear darker than the other at non-zero phase angles. This effect is termed differential phase darkening. Furthermore, the phase slope parameter is correlated with the geometric albedo. Low albedo (darker) objects tends to have lower values of *G* (Tedesco 2002). Thus an asteroid that is already difficult to detect because of low albedo, is made more difficult to detect because of differential phase darkening.

Luu and Jewitt (1989) modeled the discovery circumstances of near-Earth asteroids to study the effects of albedo and differential phase darkening on discovery bias. They assumed a bimodal population of NEAs that mirrors the first classification of main-belt asteroids into S- and C-types (Zellner 1973). I have re-implemented the model of Luu and Jewitt in order to reevaluate their conclusions in light of the characteristics of current day search programs such as LINEAR. I then present another model to calculate the discovery bias of asteroids based on the population estimates of section 2.7. This model will be further developed in Chapter 4 by expanding the taxonomy to include a more detailed description of asteroid types and to account for additional sources of observational bias.

3.3 Description of Luu and Jewitt Model

The model of NEA discovery bias developed by Luu and Jewitt (hereafter referred to as the LJ model) uses a Monte-Carlo approach to generate NEAs and tests whether those NEAs are detected or not. The statistical characteristics used to generate those Monte-Carlo NEAs are as follows.

1) They are uniformly distributed in three dimensional space around the Earth, from its surface ($\Delta_{min} = 4.3 \times 10^{-5}$AU) out to a distance of Δ_{max} = 1.5 AU. The orbits of the NEAs are not modeled, they are statically placed within this volume.

2) The diameters of the asteroids are selected according to a power law distribution $\left(\mathrm{N}(>D) \propto D^{-\alpha}\right)$ with exponent, α, varying from 2.0 to 4.0, within the range of 1 to 10 km.

3) Each asteroid is equally likely to be either S-type or C-type, with S-type asteroids assigned albedos and phase slope parameters of p_S=0.150, G_S=0.25, and C-type asteroids assigned albedos and phase slope parameters of p_C=0.047, G_C=0.15.

NEAs are randomly generated with those statistical properties, and the geocentric distance, heliocentric distance, solar elongation, phase angle and apparent visual magnitude are all calculated. To be detectable, a Monte-Carlo NEA must have a solar elongation greater than 90°, and must be brighter than the detectability threshold of V_{lim}=15.5. Any Monte-Carlo NEA that meets those two criteria is deemed discovered and its properties are recorded. The simulation continues generating Monte-Carlo NEAs until 10,000 NEAs are discovered. Since equal numbers of S-types and C-types are generated, the resulting ratio of S-types to C-types (n_S:n_C) is the observational bias factor for how strongly S-types are favored over C-types for discovery. The LJ model includes a final step in which the discovered Monte-Carlo NEAs are renormalized so that the model phase distribution matches the observed phase distribution for NEAs at the time of discovery, and the n_S:n_C ratio is recomputed. As this final step does not appear to substantially change the results, and it was not described in detail in the paper, it was omitted.

Table 3.1 gives the n_S:n_C bias factors from the original LJ work, as well as the values obtained from the current reimplementation using the same model parameters. For each value of the power law index, α, the current implementation of the LJ model was run 100 times. The results from the runs were checked for statistical agreement, and then combined. The current reimplementation agrees with the previously published factors, indicating that this is an accurate reimplementation of the LJ model.

power law index, α	$B_{S:C}$ (from Luu & Jewitt)	$B_{S:C}$ (reimplementation)
2.0	5.61 ± 0.14	5.31 ± 0.01
2.5	5.38 ± 0.13	5.43 ± 0.01
2.8	5.73 ± 0.14	5.53 ± 0.02
3.0	5.68 ± 0.14	5.57 ± 0.02
3.5	5.65 ± 0.14	5.76 ± 0.02
4.0	5.88 ± 0.15	5.94 ± 0.02

Table 3.1 Model bias correction factors. The bias correction factors from Luu and Jewitt 1989 are shown for comparison with the reimplementation of the same algorithm as presented here.

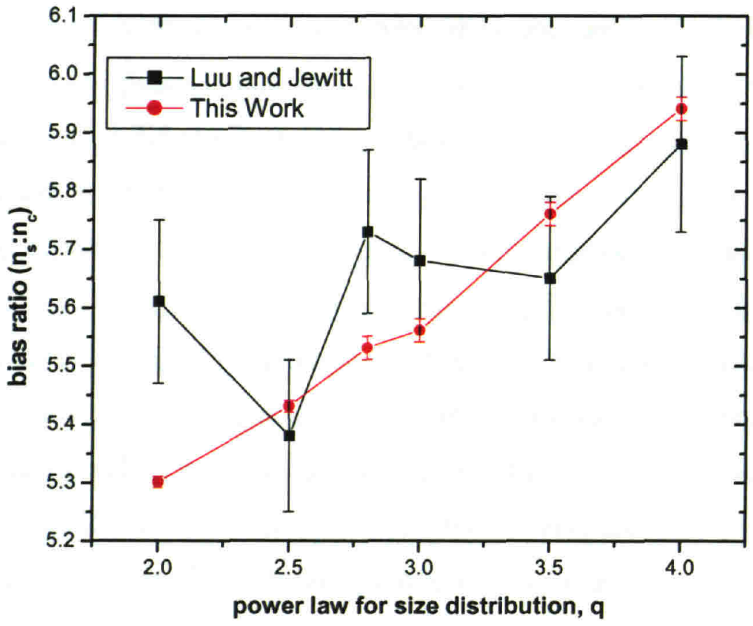

Figure 3.1Model bias correction factors. The bias correction factors from Luu and Jewitt 1989 are plotted for comparison with the reimplementation of the same algorithm as presented here.

3.4 Further Experiments with the LJ Model

I next experiment with the LJ model to explore the effects of several of the parameter values. I will use, as a baseline, the bias factor for the α=3.0 power law model. The results of these experiments are summarized in Table 3.2. The first question I will address is the relative importance of albedo and differential phase darkening.

Experiment	$B_{S:C}$
baseline	5.57 ± 0.02
albedo only	4.67 ± 0.01
phase slope, G only	1.19 ± 0.01
p_S=0.23, p_C=0.12	2.91 ± 0.01

Table 3.2 Bias factors for alternate scenarios. The baseline scenario is the same as in **Table 3.1**, for the α=3 case with p_S=0.15, p_C=0.047, G_S=0.25,G_C=0.15. The "albedo only" scenario sets G_S=G_C=0.15, while leaving the albedos as in the baseline scenario. The "phase slope, G only" scenario sets p_S= p_C=0.15, while leaving the phase slope as in the baseline scenario. The "p_S=0.23, p_C=0.12" scenario uses the quoted values for albedo, and the baseline values for G.

3.4.1 Differential Phase Darkening versus Albedo

To separate the effect of albedo from the effect of differential phase darkening, I ran two sets of experiments. As before, each experiment consists of 100 runs of the LJ model, and each run continued until 10000 asteroids were detected. In the first experiment, I set the phase slope parameters of the two types of asteroids to be equal, G_S=G_C=0.15, leaving only the albedo to distinguish them. In the second experiment, I set the albedos of the two types of asteroids to be the same, $p_S = p_C$ =0.15, leaving only the phase slope parameters to distinguish them. The results are given in Table 3.2. Almost all of the S:C discovery bias is produced by the difference in albedo, with the phase darkening playing a very minor role. This is to be expected, since the maximum difference in phase darkening with the G values used here occurs at a phase angle of about 80°, and is a difference of only about 0.22 visual magnitudes. The factor of three difference in albedo assumed here, on the other hand, produces a difference of 1.2 visual magnitudes. The lack of importance of the phase parameter in determining discovery bias accounts for the fact that this reimplementation closely matches the original LJ results despite the lack of a renormalization procedure being applied to the phase angle distribution. Shoemaker *et al.* (1990) similarly finds that the S:C discovery bias attributable to differential phase darkening accounts for a bias factor of 1.24.

Luu and Jewitt (1989) also include a simulation of discovery of main-belt asteroids to determine an S:C bias ratio for the main-belt. Their bias ratios for main-belt asteroids are much lower than their model's bias ratio for the NEAs. They conclude that the difference in the bias ratio between the main belt and the NEAs is attributable to the fact that NEAs are often discovered at higher phase angles than main-belt asteroids, and the lower phase coefficient for C-type asteroids relative to S-type asteroids produces more

phase darkening for the C-types. I have shown that the differential phase darkening is a minor contributor to the S:C bias ratio in the LJ model. How can this apparent contradiction be resolved? Luu and Jewitt did not consider the effects of overall completeness level on the bias ratio. If a population of equal numbers of S- and C-type asteroids is say, 99.9% complete (meaning that 99.9% of the asteroids in the population have been discovered) then the observed bias ratio is necessarily going to be very close to unity. Only if the survey is substantially incomplete can there can be a substantial observational bias in the observed S:C ratio. I also implemented Luu and Jewitt's model of main-belt asteroid discovery to reproduce their model bias numbers for that population. I found that for the α=3 case, the overall completeness level approached 25%, meaning that 25% of the randomly generated test asteroids were observable. On the other hand, for the LJ NEA model in the α=3 case, only 0.8% of the test asteroids were observable. This difference in completeness of the Luu and Jewitt NEA model versus their main-belt model accounts for the difference they computed for the S:C bias ratios of the NEAs and the main-belt population.

For the phase coefficients assumed in the LJ model, G_C=0.15 and G_S=0.25, the maximum difference in brightness due to phase loss occurs at a phase angle of about 80°, and is equal to about 0.22 magnitudes. For LINEAR, a wide-area, ground-based survey, the average phase angle for detected NEAs is 28°. The average difference in phase loss for G_C=0.15 and G_S=0.25 is about 0.13 magnitudes, or a factor of 1.13 in brightness. This same factor of brightening could be achieved by increasing the albedo of the S-type NEAs from 0.15 to 0.17. That small a change in albedo is smaller than the uncertainties in the albedos of the NEAs.

3.4.2 Changing the Albedos

I next consider the question of how the assumed albedos affect the computed bias. For this I used albedo values similar to the current assumptions about S-type and C-type albedos (Morbidelli *et al.* 2002b), with a factor of two difference between the types, p_S=0.23, p_C=0.12. As expected, the lower difference between the albedos substantially reduces the resulting bias factor, as seen in Table 3.2.

3.4.3 Limiting Magnitude of Survey

Another consideration is the effect of the limiting magnitude of the survey. Current search programs routinely achieve limiting magnitudes in the range of V_{lim}=18 to V_{lim}=19 (*e.g.* Pravdo *et al.* 1997, and Stokes *et al.* 2000). This produces a problem for the LJ model. A limiting magnitude this faint easily allows for the detection of 1 km diameter asteroids out to the model's geocentric distance cutoff of 1.5 AU. Applying the LJ model with a deeper limiting magnitude creates an artificial cutoff where most simulated objects are discovered right at the maximum distance of 1.5 AU, and none are discovered beyond that. Thus the increased limiting magnitude fails to make the model representative of the current search effort in which 1 km objects are routinely discovered beyond 1.5 AU. A possible solution to this is to increase the cutoff distance in the LJ model so that Monte-Carlo asteroids can be generated at heliocentric distances beyond 1.5 AU. However, in order to allow the discovery distances to be limited by the newly increased detectability threshold, rather than by an arbitrary cutoff, the distance cutoff for generating Monte-Carlo asteroids must be increased to about 3.5 AU from the Earth, or well into the main belt. The simulation would then be based on the assumption that NEAs are uniformly distributed within a volume extending outward from the Earth to the main belt, an assumption that is indefensible. A better approach is to include orbital dynamics and a model of the orbital distributions of the NEAs in the simulation. This will create a more realistic description of the spatial distribution of NEAs.

3.5 Bias Model Based on Orbital Distributions

The capabilities of current search programs to detect NEAs when they are as far away as the main belt makes it necessary to properly model the orbits of NEAs to get an accurate picture of discovery geometry. Thus, I started with a model of the NEA population from section 2.7 that provides an estimate of the distribution of the NEAs in a three dimensional space of orbital parameters. As in the LJ model, I used a pseudorandom number generator to create test particles such that the resulting distributions of the three orbital parameters, semi-major axis, eccentricity, and inclination would match the real NEA population. The other orbital parameters, argument of perihelion, longitude of the ascending node, and mean anomaly, were all uniformly distributed from 0 to 2π. At this stage of the simulation, the test particles were not

assigned sizes or brightnesses. The randomly generated orbits were propagated and the daily positions were checked against three years of pointing history from the LINEAR system (the same pointing described in section 2.3). Any time a test particle fell within the telescope's field of view, without regard to brightness, the event was noted, along with enough information to completely recover the viewing geometry later (the 6 orbital elements, the search's limiting magnitude, the geocentric distance, the heliocentric distance, and the phase angle). The orbits of test particles that never fell within the field of view were separately recorded.

The second part of the simulation was to apply various models of size, and albedo to determine which test particles would be detected by the survey. In the simplest case, the simulation can assume the same parameters as the LJ model, albedos and *G* values for S-types and for C-types, and the same population slope parameters and produce bias factors comparable to the LJ model, but more appropriate for the results of current search programs. Those results are given in Table 3.3 as the LINEAR model.

power law index, α	$B_{S:C}$(reimplementation)	$B_{S:C}$(LINEAR model)
2.0	5.31 ± 0.01	1.79 ± 0.03
2.5	5.43 ± 0.01	1.89 ± 0.03
2.8	5.53 ± 0.02	1.97 ± 0.03
3.0	5.57 ± 0.02	2.03 ± 0.04
3.5	5.76 ± 0.02	2.13 ± 0.04
4.0	5.94 ± 0.02	2.25 ± 0.05

Table 3.3 The bias correction factors for discovery bias of S-type and C-type NEAs using the same parameters as the Luu & Jewitt model. The second column repeats the values from **Table 3.1** for the reimplementation of the LJ model. The third column gives the bias correction factors using the same parameters as the LJ model for NEA size limits, power law index, albedos, and phase slope parameters, but using the NEA absolute magnitude and orbital element distributions from section 2.7 and the pointing history from LINEAR to model the NEA population and the discovery circumstances.

3.6 Conclusions

NEAs of different taxonomic classes have different observational selection effects. The observed ratios of class number is therefore not representative of the true ratios in the complete NEA population. The two most important factors that control this differential selection bias are the albedos of the classes, and the overall completeness level of the survey. Dark, low albedo NEAs are more difficult to discover than similar sized, high albedo NEAs, and will thus be under-represented in the observed NEA population. As the survey of NEAs becomes complete, or finds all of the NEAs down to some size limit,

this bias will naturally disappear since the observed population becomes identical to the complete population.

Other factors besides albedo and survey completeness affect the observational selection biases. Differential phase darkening also produces a selection bias against darker objects. However, the size of the selection effect that is due only to differential phase darkening is insignificant when compared to the bias due solely to albedo. Indeed, the effect of differential phase darkening for the model used here is smaller than the effect of small changes in the albedo of S- and C-type NEAs.

The NEA absolute magnitude distribution from section 2.7 has a slope of 0.39. This translates to a slope in the diameter distribution of α=1.95. The current best estimate for the albedos of the S- and C-type NEAs (Table 4.7) is p_S=0.23, p_C=0.12. Using this size distribution and those albedos with the LINEAR bias model, the observational bias ratio is $B_{S:C}$=1.30±0.02.

To accurately model the selection biases for the currently known population of NEAs, one must account for the ability of current search programs to discover NEAs when they are as far away as the inner main-belt. Thus, the orbits of the NEAs must be accurately modeled along with the parameters of the NEA survey programs to capture effects relating to observing geometry. In the real world, when a survey like LINEAR discovers an NEA, its taxonomic classification and albedo are not known. Another observational program must obtain the NEA's reflectance spectrum over visible and near-infrared wavelengths to determine taxonomy. To determine its albedo, the NEA must be measured in the visible and thermal infrared parts of the spectrum by a third observational program. These additional surveys introduce their own selection effects which must be accounted for to convert the observed distributions of taxonomic classes and albedos into an estimate of the true, unbiased distributions. The NEAs have also been found to be more diverse than a simple S/C bimodal distribution. Including other taxonomic categories, each with its own albedo will also change the bias ratios. Analyzing these effects will be the focus of Chapter 4.

Chapter 4 Albedos and Diameters of the NEAs

4.1 Abstract

I present a model of the near-Earth asteroid albedo distribution. The albedo distribution is based on a bias correction method described here and applied to albedo and spectral measurements of the NEAs. I find that the bias-corrected, fractional abundances of the taxonomic complexes are as follows: A-0.2%; C-10%, D-18%, O-0.4%, Q-14%, R-0.1%, S-22%, U-0.4%, V-2%, X-34%. Overall, the bias-corrected mean albedo for the whole NEA population is 0.14±0.02. Using this mean albedo, an absolute magnitude of 17.7±0.1 translates to an estimated diameter of 1 km. I find that there are 1090±180 NEAs with diameters larger than 1 km.

4.2 Introduction

Recent estimates of the number of near-Earth asteroids (NEAs) constrain the size of the population as a function of absolute magnitude (Bottke *et al.* 2000, Stuart 2001, Bottke *et al.* 2002; see also section 2.7). The reflectivity, or geometric albedo (Russell 1916) must be known to estimate the size of an NEA from its measured absolute magnitude (*e.g.* Harris and Harris 1997, Fowler and Chillemi 1992). Since few albedo measurements have been made for NEAs, the absolute magnitudes cannot be converted to physical sizes. Albedo measurements are available for fewer than 1% of the NEAs, and those albedo values span a wide range, from 0.023 to 0.63. This factor of 27 variation in albedo corresponds to more than a factor of 5 uncertainty in the diameter of an NEA with a given absolute magnitude. Therefore, the size of the population as a function of diameter is poorly known.

Several past attempts have been made to estimate the albedo distribution of the NEAs. Luu and Jewwit (1989) used a Monte-Carlo simulation of NEA discovery to estimate the observational bias in the ratio of an assumed bimodal population of light (S-type, albedo = 0.15) and dark (C-type, albedo = 0.047) NEAs (see Chapter 1 for more description of that work). Shoemaker *et al.* (1990) used a similar argument to obtain a mean albedo for the NEAs and to convert their absolute magnitude distribution to a diameter distribution (and ultimately to distributions for impact energy and crater diameter). The primary reason for updating these earlier estimates here is to make use of

the order-of-magnitude increase in the number of known, catalogued NEAs, to take account of the capabilities of current NEA search programs that lead to observational biases that are different from those of the search programs of the 1980s, and to include the latest taxonomic classifications and albedo measurements for NEAs.

Morbidelli *et al.* (2002b) have recently conducted a similar study. They attempt to define a reasonable albedo distribution for each of the main-belt source regions that their earlier work (Bottke *et al.* 2000, and Bottke *et al.* 2002) identified as being the most important suppliers of asteroidal and cometary material to the NEA population. The albedo distributions of the main-belt source regions can then be combined in the correct proportions to yield an albedo distribution of the NEAs. Unfortunately, the albedo distribution of the main-belt source regions is poorly known for asteroids in the same size range as the NEAs. Thus, the albedos of the small members of the main-belt source regions that ultimately become the NEAs must be extrapolated from the albedos of the larger members. The work presented here is a complementary approach that uses direct observation of the physical properties of a subset of the NEAs to determine the albedo distribution of the NEAs for which albedos are not available.

The rest of this chapter describes the debiasing of the NEA taxonomy and albedo data in an essentially two-step process. First, the absolute magnitude and orbital element distributions from section 2.7 are combined with albedo measurements within each taxonomic complex to define an average albedo for each complex. Second, the average complex albedos are combined with the observed fractional abundances of the complexes to produce debiased fractional abundances for each complex. The average complex albedos and debiased fractional complex abundances are combined to derive an overall average albedo and a diameter distribution for the NEAs.

4.3 Spectroscopic and Albedo Data

Building on the success of the Small Main-belt Asteroid Spectroscopic Survey, a multi-wavelength observing program has been (and is continuing to be) carried out to obtain spectra and albedos for NEAs. This program comprises visible spectroscopy, near-infrared spectroscopy, and thermal infrared flux measurements. The visible spectroscopy is collected at Kitt Peak National Observatory, at Palomar Observatory,

and on the Magellan I Telescope at Las Campanas Observatory. Near-infrared spectroscopy is collected at the NASA Infrared Telescope Facility. The W.M. Keck Observatory is used to obtain thermal flux measurements for albedo modeling.

The visible and near-IR spectra obtained for the NEAs were reduced with the Image Reduction and Analysis Facility (IRAF) software using the standard techniques described by Bus and Binzel (2002a). The resulting spectra were converted to spectral types using the Bus taxonomy as described in Bus and Binzel (2002b). The spectral types were combined into a smaller number of complexes as described in Bus and Binzel (2002b).

The thermal flux measurements from Keck were converted to estimates of albedo, radiometric diameter, and beaming parameter using the Near-Earth Asteroid Thermal Model described by Harris (1998). The albedo values used in this work are from Delbo *et al.* (2003), and Harris and Lagerros (2002). These data are summarized in Table 4.1 and Figure 4.1. Further detail is given in Table 4.2, in which the NEATM albedo, taxonomic classification, and absolute magnitude are given for each of the 36 NEAs with NEATM albedo measurements. The publications from which the albedo values are taken are also listed in Table 4.2.

Taxonomic Complex	Includes	# of NEA Albedos	# of NEA Spectra
A	A	0	1
C	C,C-subgroups,B,F,G	6	23
D	D,T	1	9
O	O	1	6
Q	Q, Sq	7	80
R	R	0	1
S	S,K,L, S-subgroups	12	125
U	U	0	3
V	V	3	14
X	X,X-subgroups,E,M,P	6	48
Totals		**36**	**310**

Table 4.1 NEA Spectral and Albedo Data. The taxonomic complexes of Bus and Binzel (2002b) are grouped into 10 complexes. The number of NEA spectra and NEATM albedos (Delbo *et al.* 2003) available for each complex is given.

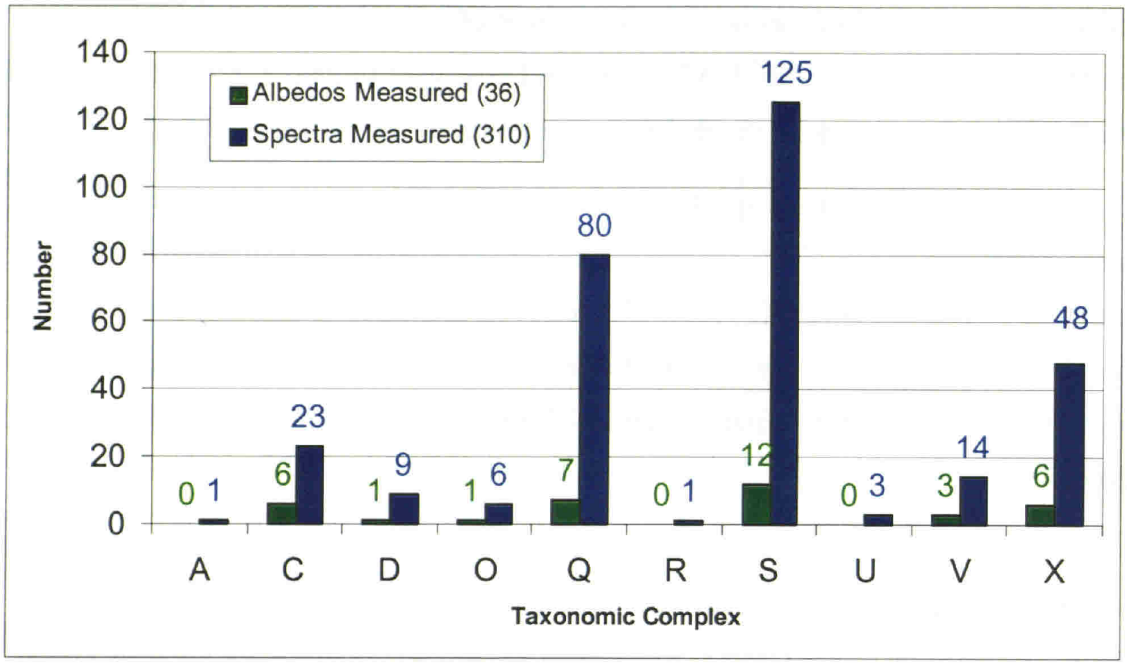

Figure 4.1 NEA Spectral and Albedo Data. The taxonomic classes of Bus and Binzel (2002b) are grouped into 10 complexes. The number of NEA spectra and NEATM albedos (Delbo *et al.* 2003) available for each complex is given.

Name	Complex	Absolute Magnitude	Albedo	Reference
(433) Eros	S	11.2	0.21	1
(1566) Icarus	Q	16.0	0.33	2
(1580) Betulia	C	14.6	0.17	2
(1627) Ivar	S	12.9	0.15	3
(1862) Apollo	Q	16.3	0.26	4,2
(1866) Sisyphus	S	13.0	0.15	3
(1915) Quetzalcoatl	S	19.0	0.31	2
(1980) Tezcatlipoca	S	14.0	0.14	1,2
(2100) Ra-Shalom	C	16.1	0.08	3
(2201) Oljato	Q	16.9	0.24	2
(3200) Phaethon	C	14.5	0.11	4,2
(3551) Verenia	V	16.8	0.53	2
(3554) Amun	M	15.9	0.17	4,2
(3671) Dionysus	C	16.7	0.16	2
(3757) 1982 XB	S	19.0	0.34	2
(4034) 1986 PA	O	18.2	0.52	3
(4055) Magellan	V	14.9	0.31	3
(4660) Nereus	E	18.7	0.55	3
(5587) 1990 SB	Q	13.6	0.5	3
(5604) 1992 FE	V	17.4	0.32	3
(5751) Zao	E	14.9	0.36	3
(6053) 1993 BW3	Q	15.2	0.18	5,2
(6178) 1986 DA	M	15.1	0.14	4,2
(6489) Golevka	Q	19.1	0.63	6,2
(9856) 1991 EE	S	17.0	0.30	7
(14402) 1991 DB	C	18.9	0.14	3
(16834) 1997 WU22	S	15.4	0.3	3
(19356) 1997 GH3	S	17.0	0.34	3
(25330) 1999 KV4	C	16.3	0.05	3
1999 FK21	S	18.0	0.32	3
1999 NC43	Q	16.1	0.14	3
2000 BG19	P	17.8	0.04	3
2000 PG3	D	15.7	0.042	3
2001 FY	S	18.8	0.52	3
2002 BM26	P	20.1	0.02	3
2002 CT46	S	20.8	0.32	3

Table 4.2 Details of NEATM albedo measurements used here. Shown are the MPC catalog number (if the asteroid is numbered) and name or provisional designation along with the taxonomic complex from the Bus Taxonomy, the V-band absolute magnitude, the V-band albedo from the NEATM thermal model, and the publication from which the albedo was obtained. The reference numbers correspond to the following papers: 1 – Harris and Davies (1999); 2 – Harris and Lagerros (2002); 3 – Delbo *et al.* (2003); 4 – Harris (1998); 5 – Pravec *et al.* 1997; 6 – Mottola *et al.* 1997; 7 – Harris (1998).

4.4 Trends in Albedo Data

To test for correlations between the albedos of NEAs and their orbital parameters or absolute magnitudes, I have utilized a larger set of NEA albedo data, including albedo measurements from a variety of methods. Most of these 80 albedo measurements are taken from Table 1 of Binzel *et al.* (2002a), except for two that are noted in Table 4.3. Note that many of the albedo measurements used to look for trends in the albedo data are not used in the rest of the analysis in this chapter because they are not from the NEATM thermal model and I have no bias correction model for the disparate sources of these other albedo measurements. There are suggestions that the albedos of S-type asteroids increase with decreasing size when main-belt asteroids are combined with NEAs (Binzel *et al.* 2002b). Looking at just the NEAs, however, this trend is not compelling (Figure 4.2). Formally, the correlation between absolute magnitude and albedo is not quite statistically significant at the 95% level. None of the taxonomic complexes exhibit a convincing correlation between albedo and absolute magnitude, so I assume that there is no correlation in debiasing the NEA albedo data.

Scatter plots of albedo versus orbital parameters are given in Figure 4.3, Figure 4.4, Figure 4.5, and Figure 4.6. There is no statistically significant correlation between albedo and eccentricity (Figure 4.4) or inclination (Figure 4.5). There is perhaps some correlation between albedo and semimajor axis (Figure 4.3). This correlation is better explained as a dependence of albedo on the Jovian Tisserand parameter (Figure 4.6).

NEA Designation	Taxonomic Complex	Tisserand Parameter	Albedo	Albedo Source
2000 PG3	D	2.547109	0.042	NEATM*
3552	D	2.313653	0.02	RPB,AIII
1999 JM8	P	2.985565	0.02	Radar*
5370	C	2.730813	0.05	RPB,AIII
14827	C	2.928258	0.05	RPB,AIII
3360	C	2.963798	0.07	RPB,AIII
1996 JA1	V	2.958596	0.30	RPB,AIII

Table 4.3 Albedos and Taxonomic Complexes for NEAs with T_J<3 and measured albedos. Of the NEAs with known albedos and $T_J < 3$, 6 out of 7 have low albedos consistent with cometary origin. The sources for the albedo measurements are as follows: NEATM – The NEATM model (Delbo *et al.* 2003); RPB, AIII – Taken from Binzel *et al.* (2002a); Radar - Albedo obtained by combining a radar derived shape model with optical brightness measurements (Benner *et al.* 2001). The two marked with * are the two additional albedo measurements that do not appear in Binzel *et al.* (2002a).

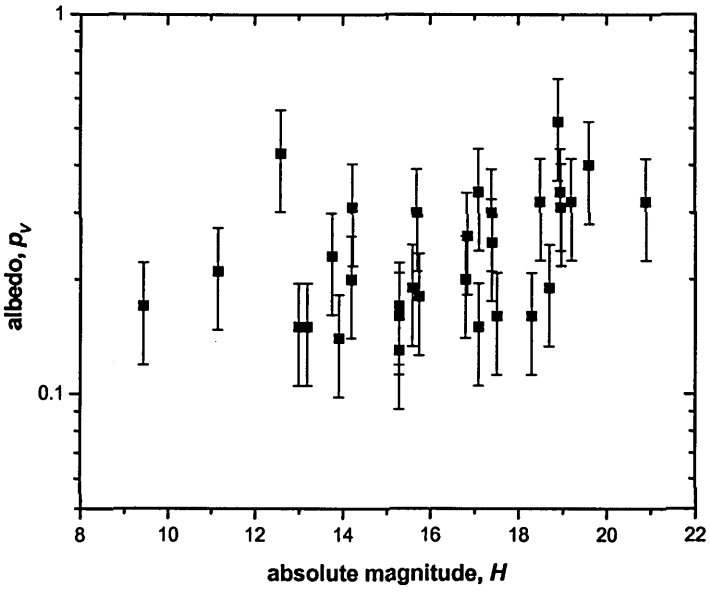

Figure 4.2 Visual Geometric Albedo versus Absolute Magnitude for S-Type NEAs. Black squares show the albedos of 80 NEAs from Table 1 of Binzel *et al.* (2002a) and Table 4.3, with 30% error bars. The correlation between p_V and H is not quite statistically significant at the 95% level using a 2-sided t-test (r = 0.35, t=2.01, *pval*=0.054).

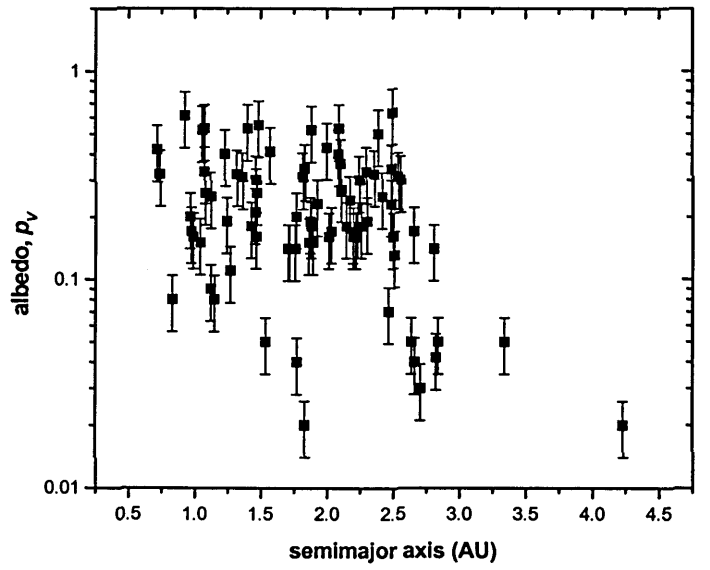

Figure 4.3 Visual Geometric Albedo versus Semimajor Axis for NEAs. Black squares show albedos of 80 NEAs from Table 1 of Binzel *et al* (2002a), with 30% error bars. The correlation between p_V and semimajor axis is statistically significant at the level of 98.8% using a 2-sided t-test (r = -0.28, t=-2.58, *pval*=0.0116). If the two points with largest semimajor axis are excluded, the significance of the correlation decreases to 97% (r = -0.21, t=-1.84, *pval*=0.069).

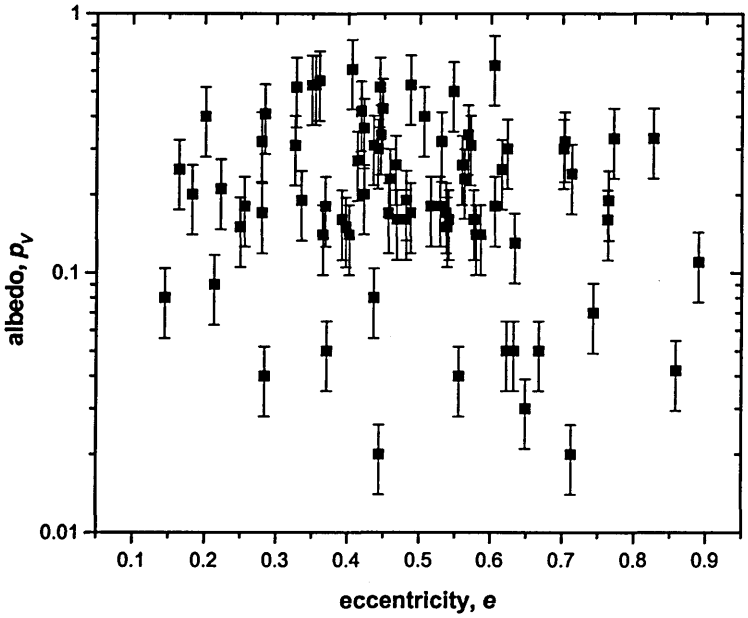

Figure 4.4 Visual Geometric Albedo versus Eccentricity for NEAs. Black squares show albedos for 80 NEAs from Table 1 of Binzel *et al* (2002a), with 30% error bars. The correlation between p_V and e is not statistically significant (86%) using a 2-sided t-test (r = -0.17, t=-1.48, *pval*=0.14).

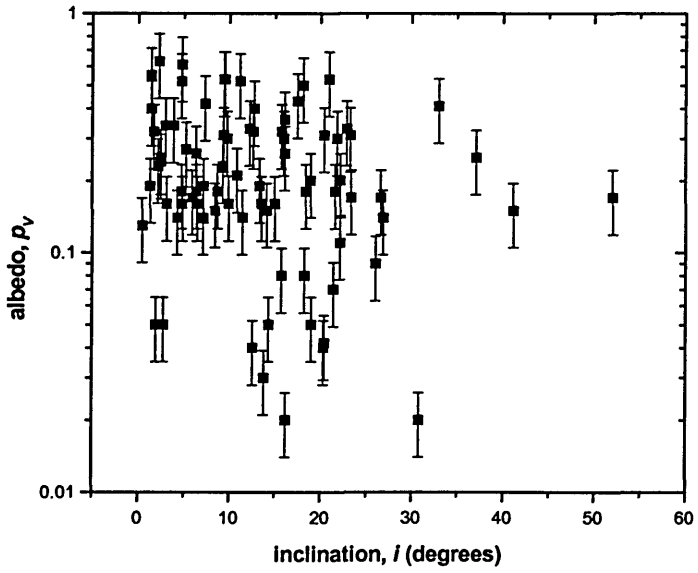

Figure 4.5 Visual Geometric Albedo versus Inclination for NEAs. Black squares show albedos for 80 NEAs from Table 1 of Binzel *et al* (2002a), with 30% error bars. The correlation between p_V and i is not statistically significant (93%) using a 2-sided t-test (r = -0.20, t=-1.79, *pval*=0.077).

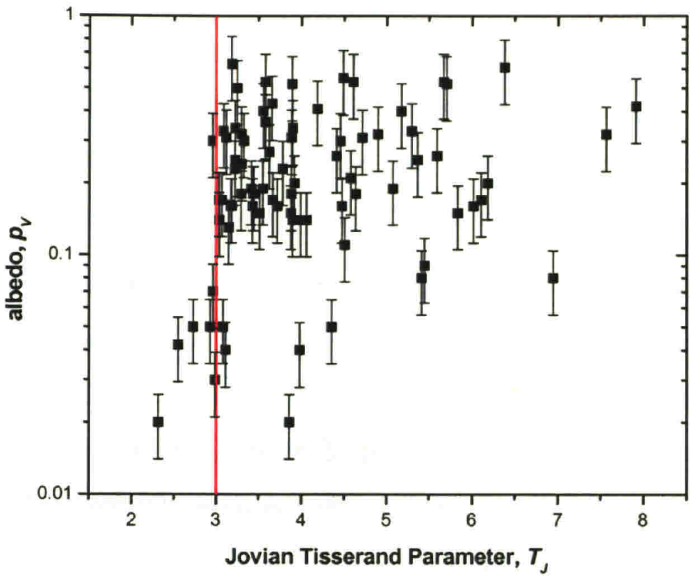

Figure 4.6 Visual Geometric Albedos versus Tisserand Parameter for NEAs. Black squares show the albedos of 80 NEAs from Table 1 of Binzel *et al.* (2002a) and **Table 4.3**, with 30% error bars. This plot is similar to Fig. 1 of Fernandez *et al.* (2001), but with only NEAs plotted. There is a marked difference in the distribution of albedos for NEAs with T_J<3 and for NEAs with T_J>3. The correlation between p_V and T_J is statistically significant (97%) using a 2-sided t-test (r = 0.24, t=2.20, *pval*=0.031). NEAs on orbits consistent with cometary origin tend to have very low albedos, also consistent with cometary origin.

The dependence of albedo on Jovian Tisserand parameter is indicative of extinct comets within the NEA population. The presence of extinct comets in the NEA population has long been an open question (for example, Öpik 1961, Wetherill 1988, Weissman *et al.* 1989, Weissman *et al.* 2002). If such exist, they are expected to have low albedos and featureless, reddened spectra similar to D-type asteroids (for example, Lagerkvist 1993, Hicks *et al.* 2000). NEAs of cometary origin may also be distinguishable by their orbital properties (for example, Kresák 1979; Harris and Bailey 1998). In particular, extinct comets may be expected to be dynamically linked to Jupiter (Kresák 1979), because the great mass of Jupiter makes it the most effective body for changing cometary orbits into NEA-like orbits. Linkage to Jupiter may be revealed by the Tisserand parameter (defined in Appendix A.3). Tisserand parameter values less than 3 indicate that an object is dynamically linked to Jupiter and is thus a candidate for being an extinct comet. An asteroid or comet may not change its Tisserand parameter solely by gravitational interactions with Jupiter, so an object with $T_J < 3$, that is not interacting with other planets will remain on an orbit with $T_J < 3$. However, an object may change

its value of T_J by non-gravitational forces (for example, cometary outgassing) or by interactions with other planets. The NEAs are in orbits that bring them close to Mars and Earth and possibly other planets, and those interactions could change the value of T_J. Therefore, the T_J=3 boundary is not expected to be a completely rigid barrier between NEAs of cometary origin and NEAs of asteroidal origin, but the gravitational effects of Jupiter are strong enough to dominate the other orbital perturbations.

It was noted by Fernandez *et al.* (2001) that the T_J=3 boundary is associated with marked bifurcation in the albedos of asteroids, with asteroids on the $T_J < 3$ side of the boundary having very low albedos similar to cometary nuclei. Using all currently available NEA albedo data confirms the trend: 6 out of 7 NEAs with $T_J < 3$ also have very low albedos. Figure 4.6 illustrates this effect, and the albedos for NEAs with $T_J < 3$ used in Figure 4.6 are given in Table 4.3.

4.5 Trends in Taxonomic Data

As with the albedos, the relative abundances of the taxonomic complexes show some correlations with orbital parameters. Figure 4.7, Figure 4.8, and Figure 4.9, show that the trend is best explained as a correlation with the Jovian Tisserand parameter, T_J. The darker complexes are more prevalent in the $T_J<3$ part of the parameter space than in the $T_J>3$ space. This is also shown in Figure 4.10 where we see that even before debiasing, the darker complexes (C, D, and X) are more abundant than the bright complexes (S, and Q) for $T_J<3$. As illustrated in Figure 4.11 through Figure 4.16 there do not appear to be any other trends in the relative abundances of the major taxonomic complexes versus the orbital parameters.

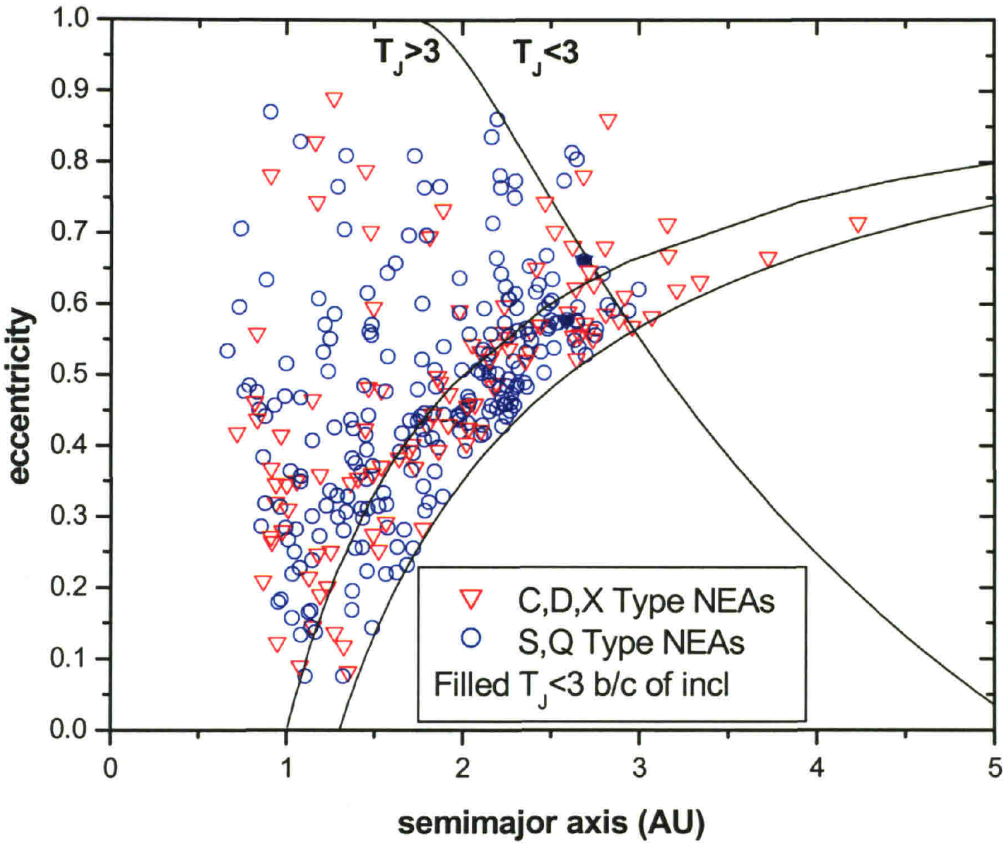

Figure 4.7 Semimajor Axis and Eccentricity for the NEAs. The taxonomic complexes are grouped into dark and light groups. The curved line that intersects the X axis at 1.3 AU delineates the edge of the NEA population as asteroids with perihelion less than 1.3 AU. The curved line that intersections the X axis at 1 AU delineates the Earth-crossing region. The other line divides the space into regions with T_J<3 and T_J>3, for asteroids with inclination of 0. A few of the NEAs are plotted with filled symbols to indicate that they have T_J<3 even though they appear on the left side of the T_J=3 boundary. The nonzero inclination of those NEAs reduces their Tisserand parameter to below 3. NEAs with T_J<3 have a higher abundance of dark taxonomic complexes than do NEAs with T_J>3.

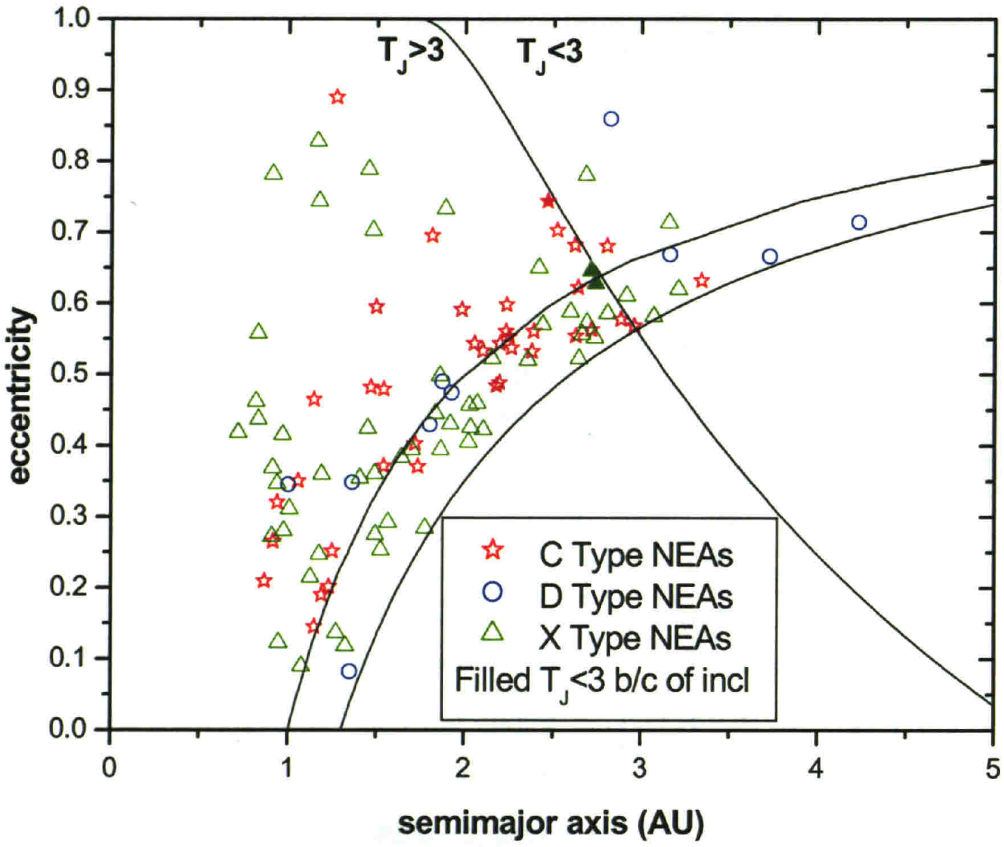

Figure 4.8 Semimajor Axis and Eccentricity for the Dark NEA Complexes. The curved line that intersects the X axis at 1.3 AU delineates the edge of the NEA population as asteroids with perihelion less than 1.3 AU. The curved line that intersections the X axis at 1 AU delineates the Earth-crossing region. The other line divides the space into regions with T_J<3 and T_J>3, for asteroids with inclination of 0. A few of the NEAs are plotted with filled symbols to indicate that they have T_J<3 even though they appear on the left side of the T_J=3 boundary. The nonzero inclination of those NEAs reduces their Tisserand parameter to below 3. Among the dark taxonomic complexes, the NEAs with the lowest values of T_J are dominated by the D-types, which have the darkest surfaces.

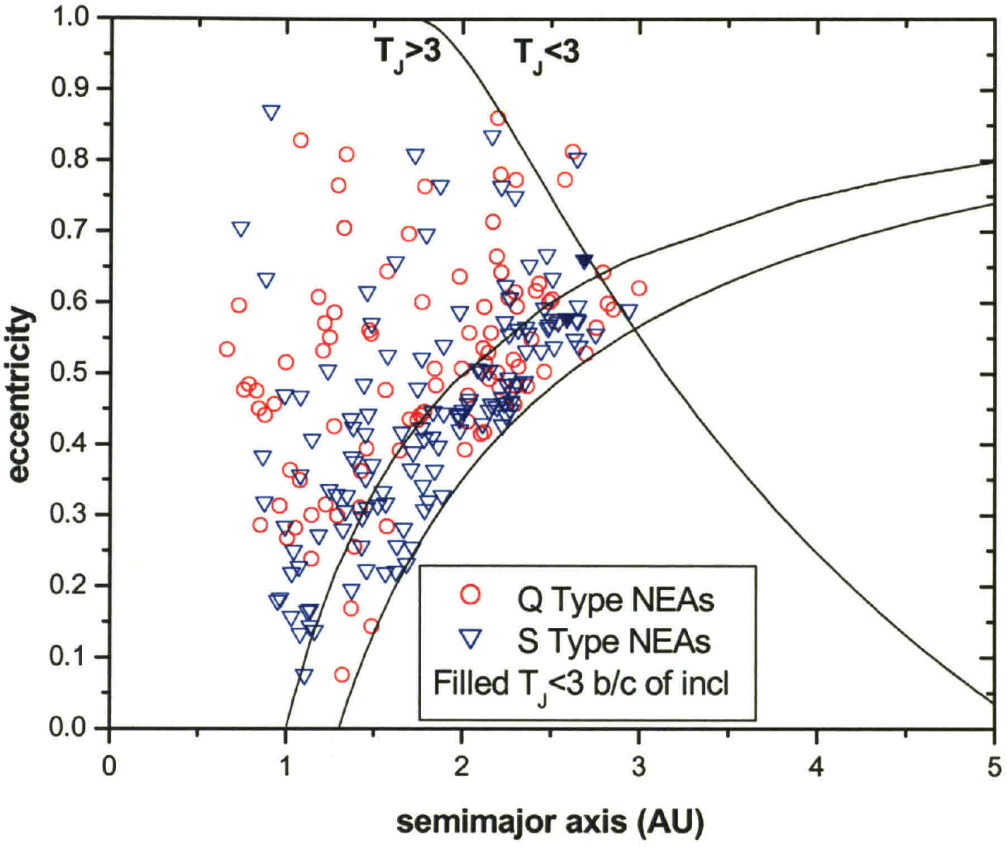

Figure 4.9 Semimajor Axis and Eccentricity for the Bright NEA Complexes. The curved line that intersects the X axis at 1.3 AU delineates the edge of the NEA population as asteroids with perihelion less than 1.3 AU. The curved line that intersections the X axis at 1 AU delineates the Earth-crossing region. The other line divides the space into regions with T_J<3 and T_J>3, for asteroids with inclination of 0. A few of the NEAs are plotted with filled symbols to indicate that they have T_J<3 even though they appear on the left side of the T_J=3 boundary. The nonzero inclination of those NEAs reduces their Tisserand parameter to below 3. The relative distributions of S and Q type NEAs do not depend on eccentricity and semimajor axis.

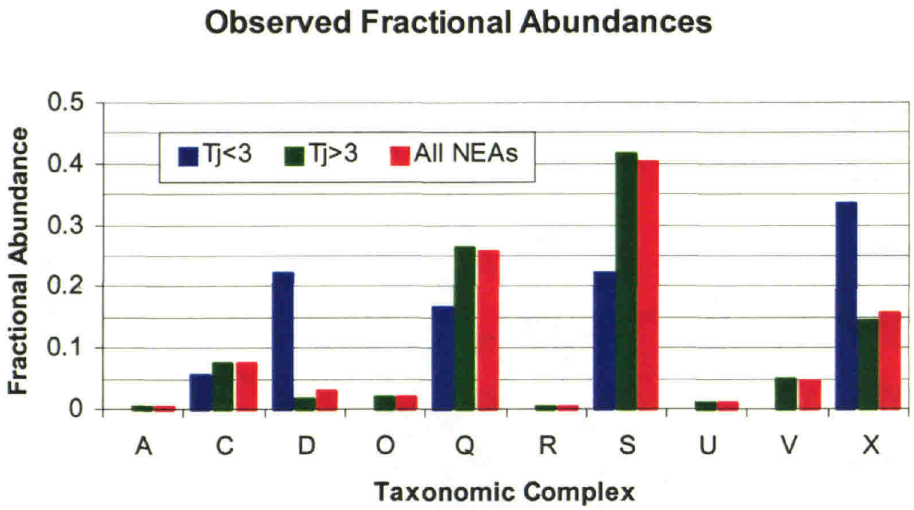

Figure 4.10 Observed Fractional Abundances of the Taxonomic Complexes for $T_J < 3$ and $T_J > 3$. The NEA classifications from Table 4.1 and Figure 4.1 are divided according to the Jovian Tisserand parameter. Even before debiasing, the dark NEA complexes, particularly the D-type NEAs are more prevalent among the NEAs with T_J <3 than among the NEAs with T_J >3. The bars are in left-right order as indicated in the caption.

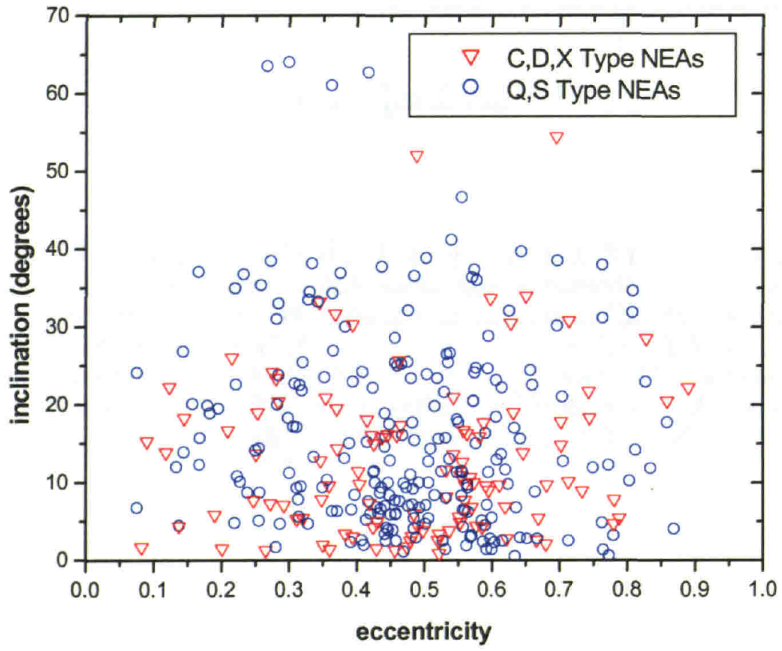

Figure 4.11 Eccentricity and Inclination for the NEAs. The taxonomic complexes are grouped into dark and light groups. The relative abundances of dark and light types do not depend upon inclination and eccentricity.

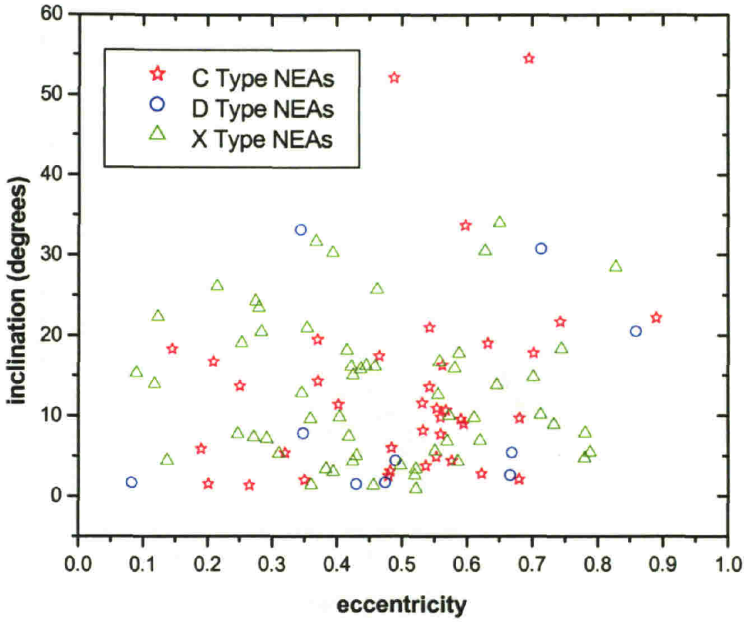

Figure 4.12 Eccentricity and Inclination for the Dark NEA Complexes. The relative abundances of the C, D, and X complexes do not depend upon inclination and eccentricity.

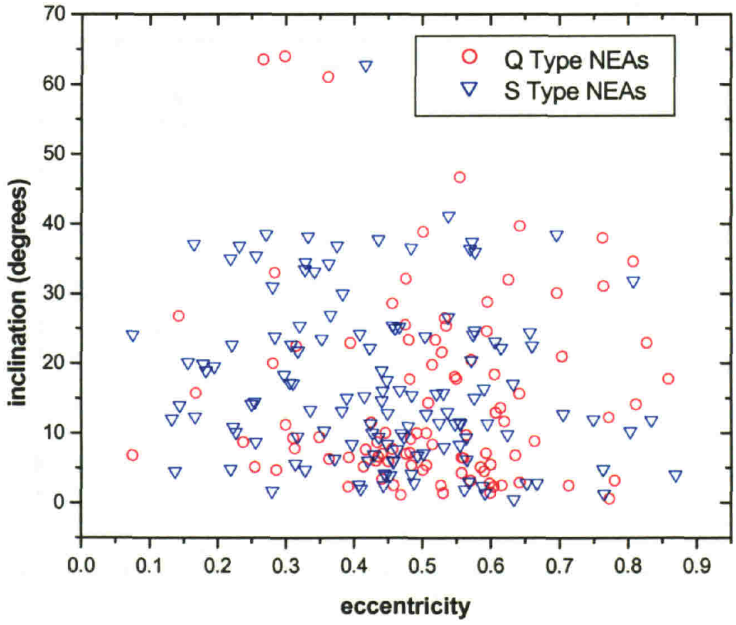

Figure 4.13 Eccentricity and Inclination for the Bright NEA Complexes. The relative abundances of the S and Q type NEAs do not depend on inclination and eccentricity.

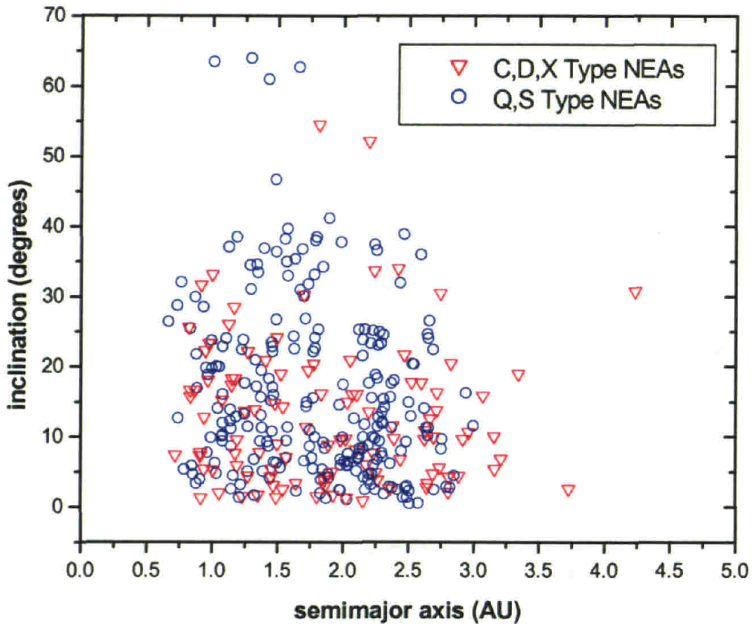

Figure 4.14 Semimajor Axis and Inclination for the NEAs. The taxonomic complexes are grouped into dark and light groups. The relative abundances of the dark and light groups do not depend on inclination and semimajor axis.

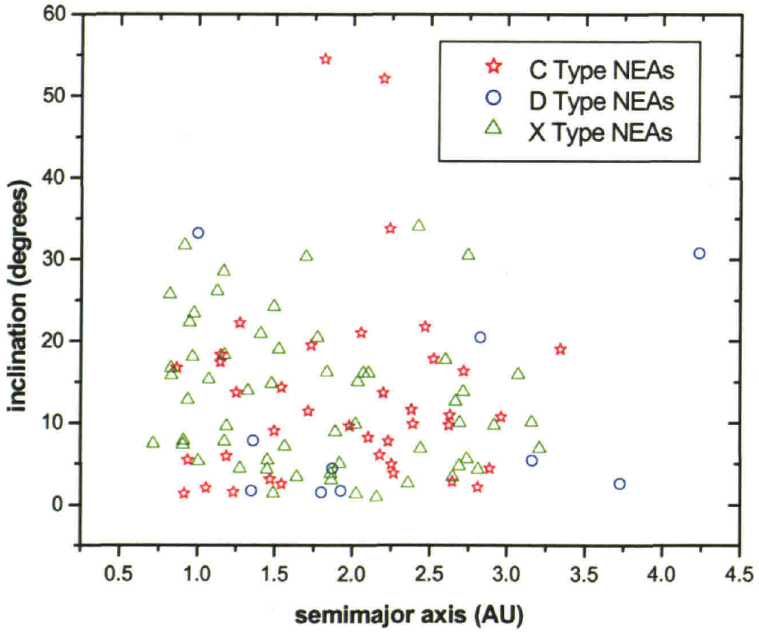

Figure 4.15 Semimajor Axis and Inclination for the Dark NEA Complexes. The relative abundances of the C, D, and X types do not depend on inclination and semimajor axis.

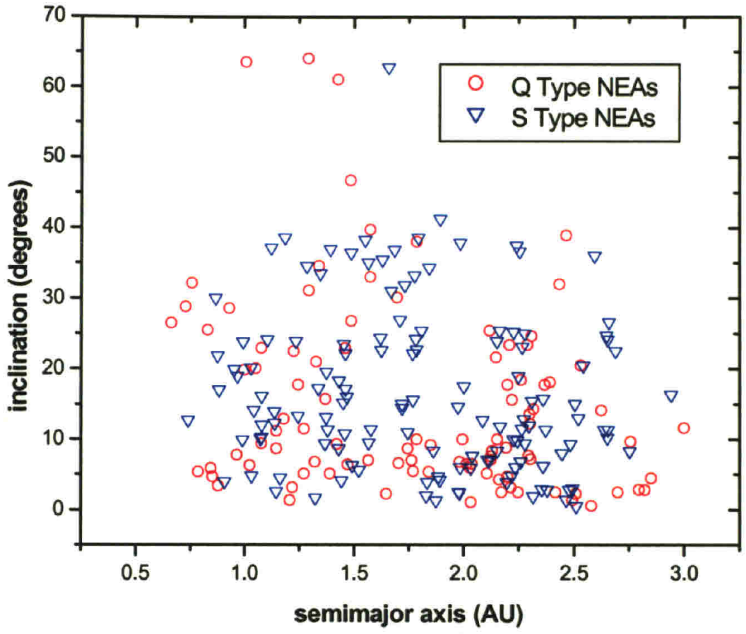

Figure 4.16 Semimajor Axis and Inclination for the Bright NEA Complexes. The relative abundances of the Q and S types do not depend on inclination and semimajor axis.

The Jovian Tisserand parameter will be discussed further in section 4.9. In the initial analysis presented next, I assume that the spectral properties and albedos of the NEAs and are not correlated with the orbital parameters, absolute magnitude, or diameter of the NEAs. I will address the effects of the correlation with T_J after discussing the simpler case of no correlation in order to show how the debiased population changes when this correlation is allowed in the solution.

4.6 Absolute Magnitude and Diameter Distributions

Before proceeding to a discussion of the methods used to debias the albedo and spectral data, I will first explain several equations necessary for working with population distribution functions based upon absolute magnitude or diameter. The absolute magnitude system and equations for converting between absolute magnitude and diameter are defined in Appendix A.1.

My population model fits an exponential distribution to the number of NEAs versus absolute magnitude of the following form:

$$N(<H) = B10^{\beta H} \tag{4.1}$$

where the exponent is $\beta = 0.39 \pm 0.013$ ($\beta = 0.35 \pm 0.02$ in Bottke's model). Equation (4.1) gives the cumulative number of NEAs with absolute magnitudes less than (i.e. brighter than) a specified value. That equation assumes that the population can be approximated by a simple exponential function. The number of NEAs can be expressed equivalently as a diameter distribution, or the cumulative number of NEAs with diameters greater than a specified value:

$$N(>D) = AD^{-\alpha} \tag{4.2}$$

Using equation **(A.2)**, the exponential slope of the absolute magnitude distribution, β, can be converted into the power-law slope of the diameter distribution quite simply as $\alpha = 5\beta$. Likewise, the scaling constants, A, and B, can be related by $A = Bp_V^{-2.5\beta}10^{\beta C}$, where p_V is the visual geometric albedo, and C=15.618 is a constant that defines the absolute magnitude system.

I now assume that the NEAs can be divided into M taxonomic complexes where all the members of a complex, i, have the same albedo, p_i, and the population distribution of each taxonomic complex follows equations (4.1) and (4.2). For each complex I may write that the number of NEAs of that type with absolute magnitudes brighter than H, is given by

$$N_i(<H) = f_i N(<H) = f_i B 10^{\beta H} \tag{4.3}$$

where the f_i are the magnitude-limited fractional abundances of each complex, and $\sum_{i=1}^{M} f_i = 1$. These magnitude-limited fractional abundances are the proportions of the NEAs that would fall into each of the taxonomic complexes if one were to classify all of the NEAs up to some limiting absolute magnitude. The population in each complex can also be described by a diameter distribution given by

$$N_i(>D) = g_i N(>D) = g_i AD^{-\alpha} \tag{4.4}$$

where the g_i are the diameter-limited fractional abundances of each complex, and $\sum_{i=1}^{M} g_i = 1$. These diameter-limited fractional abundances are the proportions of the NEAs that would fall into each of the taxonomic complexes if one were to classify all of the NEAs down to some limiting diameter. The f_i differ from the g_i because the members of

one complex have a different albedo from the members of the other complexes and the number of objects increases rapidly with decreasing size. The f_i and g_i can be related by the following equations:

$$g_i = \frac{f_i \rho_i^{-2.5\beta}}{\sum_{j=1}^{M} f_j \rho_j^{-2.5\beta}} \tag{4.5}$$

$$f_i = \frac{g_i \rho_i^{2.5\beta}}{\sum_{j=1}^{M} g_j \rho_j^{2.5\beta}} \tag{4.6}$$

I am now in a position to define an average albedo for all the NEAs, averaging over all of the M taxonomic complexes. I start with the definition that I want an average albedo, p_N such that when equation (A.2) is used, $N(>D) = N(<H)$ for all diameters and absolute magnitudes. This "number-averaged" albedo is slightly different from the geometric mean which is usually used to average together albedos from different objects. The number-averaged albedo assures that the number of NEAs brighter than a given absolute magnitude is equal to the number with diameters larger than the equivalent diameter when the number averaged albedo is used in equation (A.2) to convert between absolute magnitude and diameter. The number-averaged albedo may be calculated from the albedos of each complex and either the magnitude-limited fractional abundances or the diameter-limited fractional abundances as follows:

$$p_N = \left(\sum_{i=1}^{M} f_i p_i^{-2.5\beta} \right)^{\frac{1}{-2.5\beta}} \tag{4.7}$$

$$p_N = \left(\sum_{i=1}^{M} g_i p_i^{2.5\beta} \right)^{\frac{1}{2.5\beta}} \tag{4.8}$$

If equations (4.5) and (4.6) are used to relate f_i and g_i, then equations (4.7) and (4.8) give identical values. They are two different ways to calculate the same value of p_N.

If one is interested in a particular diameter, D_o, then one can use the average albedo, p_N to define an average absolute magnitude, H_o, that is equivalent to D_o. One can calculate H_o by using p_N and D_o in equation (A.2). This averaging function has the nice property that the same answer will be obtained if the values of p_i are averaged in subgroups, and then the subgroups averaged or if all are averaged at once.

4.7 Magnitude-limited Debiasing

In any telescope search program to discover or study asteroids, the primary observational selection effect is that the telescope is flux limited. That is, objects with bright apparent magnitudes are more likely to be observed than fainter objects. Since I am assuming that there are no correlations between the orbital parameters and the spectral properties of the NEAs, the primary selection effect is that NEAs with brighter absolute magnitudes are more likely to be discovered, and observed for spectra. Therefore, as a first step, I assume that the observed fractional abundances of NEA spectral types, and the observed albedos within a taxonomic complex are absolute magnitude limited samples, or equivalent to the f_i defined in equation (4.3). I can then use equation (4.7) to obtain debiased or diameter-limited values.

Contrary to the assumptions made above, the actual NEAs within a single taxonomic complex do not all have the same albedo. To define an average albedo within each complex I assume that each albedo measurement within a single complex represents a subset that have that albedo. I assume that the measured albedos are a magnitude-limited sample of the albedo values within a complex, and I use equation (4.7) to obtain an average albedo for each complex. So, for example, 12 members of the S complex have had their albedos measured, and the average albedo for this complex would be calculated by averaging the 12 measured albedos with equation (4.7) where the $f_i = 1/12$. A similar averaging is done for each of the other taxonomic complexes. Three of the taxonomic complexes have no NEA members with a measured albedo, so the **A**, **R**, and **U** complexes have been assigned albedos from average main-belt values[2]. These three complexes (and the **O** complex with only a single measured albedo) represent a tiny fraction of the NEAs and so they have very little effect on the final answer. The D complex also has only one member with a NEATM measured albedo, and there are enough D-types to significantly effect the final answer. However, the measured albedo

[2] The average albedos for main-belt asteroids in the A, R, and U taxonomic complexes were calculated as the geometric mean of the albedos from IRAS (Tedesco *et al.* 2002) that have the appropriate taxonomic classification from the file Taxonomic Classifications, Version 3 in the Physical Data System Small Bodies Node (http://pdssbn.astro.umd.edu/SBNast/holdings/EAR-A-5-DDR-TAXONOMY-V3.0.html) which is a compilation of the taxonomies of Tholen (1984); Barucci *et al.* (1987); Tedesco *et al.* (1989); Howell *et al.* (1994); and Xu *et al.* (1995).

for that D-type NEA (0.042) is quite similar to the average of main-belt D-types, so this NEA's albedo is used as the albedo for the D complex. The resulting debiased albedos are given in Figure 4.17. The observed (magnitude-limited) and debiased (diameter-limiter) fractional abundances are shown in Figure 4.18.

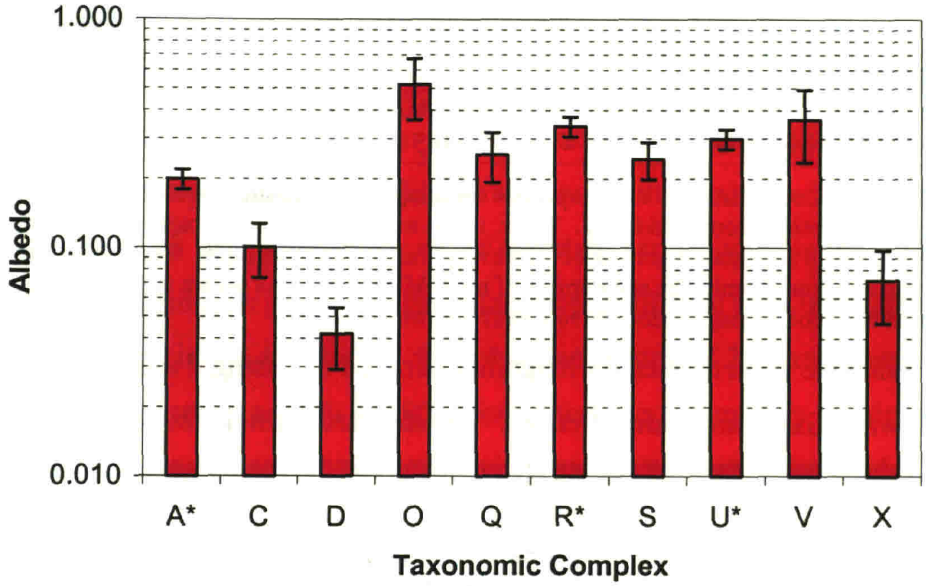

Figure 4.17 Debiased Average Albedos. The debiased average albedo of each taxonomic complex is shown as calculated from equation **(4.7)** using NEATM albedos for NEAs with SMASS taxonomy classifications. Complexes marked with * have been assigned albedos from average main-belt values.

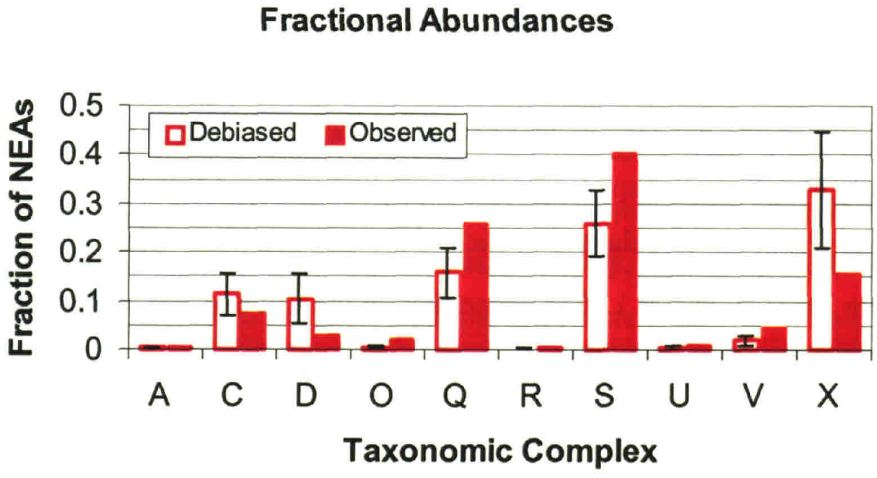

Figure 4.18 Fractional Abundances of NEA Taxonomic Complexes. The observed fractional abundances are assumed to be absolute magnitude-limited and are converted to diameter-limited or debiased fractional abundances using the average albedos for each complex.

The debiased albedos and diameter-limited fractional abundances given in Figure 4.17 and Figure 4.18 can be combined with equation (4.7) to obtain an average albedo for all of the NEAs. The average albedo can also be used to provide an absolute magnitude that is equivalent to an average 1 km diameter NEA, and estimate the number of NEAs that are larger than 1 km in diameter. These numbers are summarized in Table 4.4.

	This Chapter	Chapter 2
average NEA albedo	0.16 ± 0.02	0.11 (assumed)
H equivalent to 1 km	17.63 ± 0.1	18 (assumed)
number NEAs bigger than 1 km	885 ± 149	1227±170

Table 4.4 Summary of Average NEA Properties for Magnitude-Limited Debiasing. The current work is compared to the results from section 2.7. There, it was assumed that the average albedo of the NEAs was 0.11, meaning that an absolute magnitude of 18 was equivalent to a 1 km NEA. The debiased albedos, corresponding absolute magnitudes and number of multi-kilometer NEAs shown is derived from the assumption of an absolute magnitude-limited survey described above.

To calculate uncertainties for magnitude-limited debiasing, I assumed a straightforward Gaussian model of errors. The standard formula for propagating uncertainties (Bevington 1969, pg. 59) is

$$\sigma_f^2 = \left(\frac{\partial f}{\partial x}\right)^2 \sigma_x^2 + \left(\frac{\partial f}{\partial y}\right)^2 \sigma_y^2 \qquad (4.9)$$

where f is a function of x and y, σ_f^2 is the one-standard-deviation uncertainty for f, and x and y are uncorrelated ($\sigma_{xy}^2 = 0$). Each of the albedo measurements from NEATM are assigned uncertainties of 30%. The uncertainty in the albedo is difficult estimate precisely, because the uncertainty stems primarily from uncertainties in the thermal model used to perform the calculation rather than statistical noise in the thermal IR data. An unertainty of 30% is perhaps larger than necessary, but is a safe limit (Delbo 2003). The observed fractional abundances of each of the taxonomic complexes are assigned Poisson error bars ($\sigma_N = \sqrt{N}$). The uncertainty in the value of B is taken from the linear least-squares fit to the log of the number of NEAs as a function of absolute magnitude (Figure 2.7). All of these uncertainties are combined by equation (4.9) to calculate the one-standard-deviation uncertainty in the average albedo of the taxonomic complexes, the debiased-fractional abundandances of the taxonomic complexes, and the overall, average albedo of the NEAs.

4.8 Alternate Bias Estimation

As an alternative to assuming that the observational bias in our spectral and albedo data was simply absolute magnitude-limited, I estimated the observational bias with a simulation of the observational programs. To estimate the bias in the known NEA population that is due to albedo, I began by generating pseudorandom asteroid orbital elements that match a debiased population model. Nominally, I use the population model from section 2.7, for comparison, I also tried the population model by Bottke *et al.* (2002). Bottke's distribution differs from my distribution in a few keys ways. First, Bottke *et al.* found a slightly shallower slope in the absolute magnitude distribution, meaning that it predicts slightly fewer small NEAs relative to a given number of large NEAs. Also, my distribution predicts substantially more NEAs at high inclination, primarily as a "bump" in the distribution around an inclination of 25°, and also in a larger tail going out to inclinations as high as 50°. I found that the two models are similar enough that the resulting biases are not dependent upon which population model is chosen as a starting point (see Table 4.5).

The population model takes the three dimensional space of orbital elements, semi-major axis, eccentricity, and inclination, (a,e,i), and divides the space into a number of cells. For each cell the population model specifies the fraction of NEAs whose parameters fall within that cell. Thus, a pseudorandom number generator was used to produce test particles with values of (a,e,i) that statistically match the population model. Within each cell, the values of (a,e,i) were offset from the cell center with a uniform distribution so that the pseudorandom asteroids would fill the volume of the cell rather than all being located at the cell center. The other orbital parameters, longitude of the ascending node, argument of perihelion, and mean anomaly, were all assumed to be uniformly distributed from 0 to 2π, and values for them were assigned for each test particle. At this stage of the simulation, no size or brightness information was specified for any of the test particles. 30000 test asteroid were generated in this manner.

Each test asteroid had its orbit propagated (with a simple two-body propagation), and an ephemeris generated for each night on which the LINEAR survey operated (the same nights used in deriving the asteroid population model, with the same rejection

mechanism for nights with poor weather). A record was generated each time any test asteroid fell within the field of view of the sensor, without regard to brightness or limiting magnitude. The output record included the test asteroid's orbital elements, its heliocentric coordinates, geocentric coordinates, solar phase angle, the limiting magnitude of the telescope on that night, and the time. In short, enough information to quickly reconstruct all the relevant details of the potential observation without having to repropagate the orbit. A separate file of records was generated for those test asteroids that never fell within the field of view of the telescope. Those records contained only the orbital elements of the unobservable test asteroids. 5096 test asteroids never fell within the field of view. 24904 of the test asteroids did fall within the field of view. Those 24904 test asteroids generated 184521 potential observations, or an average of 7.4 potential sightings for each potentially observable test asteroid (POTA).

Armed with the list of POTAs and the properties of each potential observation, it is a quick matter to apply any desired distribution of absolute magnitudes, or, equivalently, any desired distribution of diameters and albedos, to the list of potentially observable asteroids. Determining which of the test asteroids would have actually been observed given its designated size, its calculated apparent brightness, and the nightly limiting magnitude for the telescope was then a simple scan through the list with no orbit propagation or field of view checks required. Thus, many different combinations of diameter and albedo could be tried with little computer time required.

For each of the real NEAs in our dataset with measured albedos, I know its absolute magnitude, spectral complex, albedo, and diameter. For each of these asteroids I conducted a simulation of the discovery and measurement bias for that particular asteroid. For example, one of our real NEAs (3200) has a measured albedo of $p_V = 0.14$, and an absolute magnitude of $H = 14.3$, giving a diameter of 5.53 km. So, all 30000 of the test asteroids were assigned albedos of 0.14, and diameters of 5.53 km. Assigning all 30000 test asteroids the same albedo and diameter allows me to average over the orbital parameter distribution and obtain a bias correction factor for this particular combination of albedo and diameter. The combination of diameter and albedo, along with the other information recorded for each potential observation (namely, heliocentric and geocentric

distances, and phase angle) allow for the calculation of the apparent visual magnitude for each potential observation via equation (A.2) with a phase slope parameter value of $G = 0.082 + 0.69 p_V$ used for all test asteroids.[3] A similar relationship between G and p_V is used by Morbidelli *et al.* (2002b).

If a potential observation had a computed apparent magnitude that was brighter than the limiting magnitude for that night, the POTA was deemed a discovered test asteroid. If a POTA was never brighter than the relevant night's limiting magnitude then it would be labeled an undiscovered test asteroid. After all POTAs where thus processed, I ended up with a list of discovered test asteroids. I also had two lists of undiscovered test asteroids (the test asteroids that never entered the field of view of the telescope and the test asteroids that were within the field of view but were never bright enough to be detected) that could be combined into one list. The fraction of discovered asteroids (i.e. $\frac{\text{discovered}}{\text{discovered + undiscovered}}$) is then a measure of the discovery bias for NEAs with the given albedo and diameter. This process was repeated for all of the NEAs in our dataset.

So far, I have estimated only one part of the albedo bias, the part that is due to the discovery of the NEAs. There is also a requirement to measure the spectra and albedos of the NEAs, and those processes add their own biases. These additional measurement biases were calculated in a similar manner to the discovery bias. I started with the list of discovered asteroids (with sizes and albedos attached), propagated their orbits, and determined which ones would have been measured for spectra with a simulation of the spectral observing programs. Those test asteroids that had their spectra measured went into a simulation of the albedo measuring program to see which would have their albedos measured. Those discovered test asteroids that were selected by the simulation for spectral and albedo measurements were deemed to be "measured" test asteroids. I then calculated the fraction of measured test asteroids for each value of albedo simulated. The fraction of measured test asteroids was then my estimate of the bias for a given albedo-diameter pair. This bias value is essentially the probability that a randomly selected NEA would have had been discovered and then gone on to have its spectrum and albedo

[3] This linear relationship between G and p_V was derived from a linear least squares fit to the values from the SIMPS catalog (Tedesco *et al.* 2002), excluding those with G=0.15.

measured. This bias is only valid in a relative sense to the bias for other albedos because I used a starting population size (30000) that is much larger than the actual number of NEAs.

To simulate the observational program to measure the spectra, I used the observational log books from observing runs to Palomar Observatory, and to Kitt Peak National Observatory from January, 1998 to March, 2002. Over a total of 31 nights, distributed between the two observatories, spectra for 180 NEAs were measured in this time period. I assume that the observational selection effects modeled for this subset of the observations is representative of the selection effects for the whole dataset. Histograms of the visual magnitudes at the times of observation indicate that the limiting magnitude for both observatories is about V_m= 19.5. Thus, a single limiting magnitude was used for all the nights modeled in this simulation. For each night on which observing was modeled at either of the locations, all of the discovered test asteroid's orbits were propagated to local midnight for that night. Any discovered test asteroid on a given night that was located above the observatory's southern declination limit, and had a solar elongation of more than 50 degrees was added to a list of potentially measurable test asteroids (PMTAs). All of the PMTAs for a given night were then ranked by a "measurement probability." The measurement probability was a combination of three probabilities that describe the interest in measuring an NEA. The first probability, p_B, modeled the desire to obtain bright asteroids because they are easier to observe, and varied linearly from 0 to 1 as the apparent visual magnitude for that night varied from 20 to 10 (however, values of apparent visual magnitude greater than V_m= 19.5 were never measured in the simulation). The second probability, p_H, modeled the desire to obtain measurements for small NEAs, and varied linearly from 0 to 1 as the absolute magnitude varied from 10 to 22. The third probability, p_I, modeled the desire to obtain measurements for high inclination NEAs, and varied linearly from 0.2 to 1 as the inclination of the test asteroid varied from 0 to 90 degrees. The final measurement probability was calculated as $p_M = 1-(1-p_B)(1-p_H)(1-p_I)$. Any PMTA with a p_M value greater than 0.7 was deemed to be measured. The value of 0.7 is an arbitrary value chosen to provide a reasonable number of simulated measurements on each night for the full range of albedos. As with the use of 30000 test asteroids, the choice of this arbitrary

cutoff sets the overall scale of the measurement biases that are calculated, but does not effect the relative bias between different values of albedo. After a PMTA passed all of the tests and was measured on some night, it was removed from the pool of PMTAs for the remainder of the nights so that any given PMTA was measured only once.

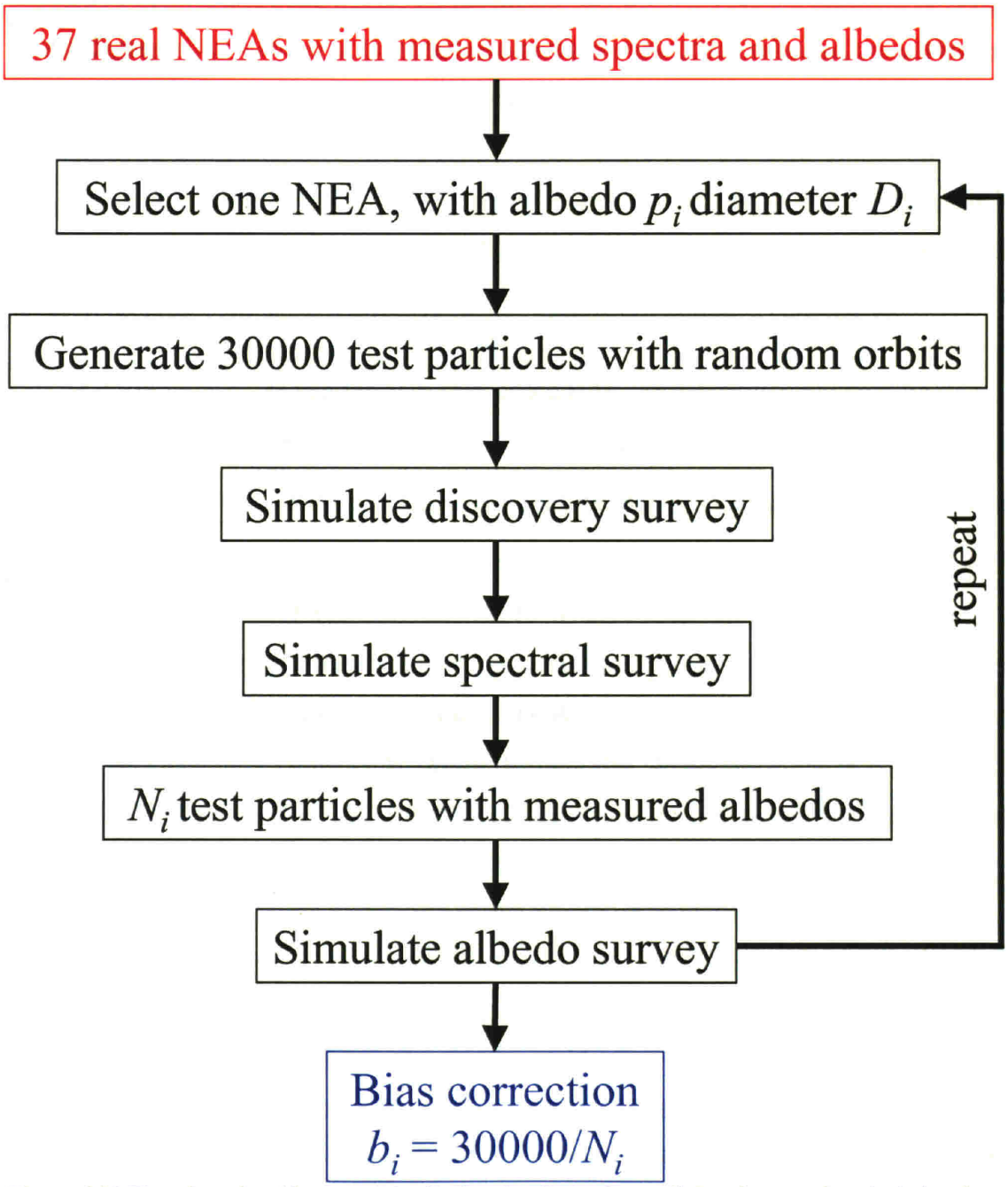

Figure 4.19 Flowchart for Alternate Bias Estimation Procedure. Shows the steps in calculating the bias correction factors. The input to the procedure is in red, output is in blue, and processes are in black.

The test asteroids that were successfully measured by the spectral observing simulation were further tested to see if they would have their albedos measured by a simulation of the albedo measuring program. The simulation for albedo measuring was very similar to the simulation for measuring spectra. The simulation modeled seven observing nights at the W. M. Keck Observatory from March 2000 to February 2002. Each of the test asteroids with successfully measured spectra had its orbit propagated to local midnight for each night at the Keck Observatory. The test asteroid's diameter, albedo, and heliocentric and geocentric distances were used to calculate the expected thermal flux at 10 μm using a simple approximation of a blackbody at uniform temperature. The observational limit for the telescope to be able to detect the asteroid and calculate its albedo was set at 2 mJy. As with the spectral measurement, a thermal measurement probability was defined to account for the interest in measuring smaller NEAs, and high inclination NEAs. This probability was defined as $p_A = 1-(1-p_H)(1-p_I)$, with p_H, and p_I as defined above for the spectral measuring. As before, any test asteroid with p_A greater than 0.7, and thermal flux greater than 2 mJy was deemed to have its albedo measured.

So, after assigning the same value of albedo and diameter to the 30000 test asteroids, processing them through the discovery simulator, the spectrum measuring simulator, and the albedo measuring simulator, some fraction of the test asteroids would have had their albedos measured. The fraction of measured asteroids is then the probability of measurement for that NEA, and is the inverse of the observational bias for that NEA. Let $b_I = \frac{30000}{\#\text{ test asteroids with measured albedos}}$. The process was repeated for each of the 36 real NEAs in my sample with measured albedos.

I wish to use these bias correction factors to average together the measured albedos within each taxonomic complex. The bias correction factors as I've stated them account for observational selection effects as a function of both size and albedo. Before averaging together the albedos from a complex of NEAs, I also need to account for the varying sizes of the NEAs within the complex. If we've found one large NEA with a particular albedo, then there are probably many small ones out there with a similar

albedo. But if we've found one small NEA with a particular albedo value that doesn't imply that there are big NEAs like it. I am assuming that the numbers of NEAs as a function of size follows a power law, equation (4.2). To average together the albedos of NEAs with different sizes, I use that power law to correct the bias factors to the same diameter. To correct for the varying sizes, I think of each NEA with a measured albedo as representing a group of similar NEAs with the same albedo and varying sizes. It just happens that I have a measurement of one object from this group. The observational bias I estimated suggests that there should be b_l similar NEAs with the same albedo and the same diameter. I use the following formula to convert that to the number of similar NEAs with the same albedo at 1 km diameter: $N_l(1) = b_l D^{\alpha+1}$, where the exponent has changed because I am using a differential distribution rather than a cumulative distribution. The l subscript iterates over the NEAs with measured albedos, within one taxonomic complex. The N_l yield diameter-limited fractional abundances for each measured albedo within a taxonomic complex by $g_l = \frac{N_l}{\sum N_l}$. The average albedo for each complex can then be computed by equation (4.5), averaging over all of the NEAs within the complex that have measured albedos, ρ_l.

The results of this model are summarized in Table 4.5 (labeled as **survey simulation**). The results are very similar to the results from assuming a magnitude-limited sample (labeled **magnitude-limited debiasing**). In addition, several test cases were performed where some of the assumptions within the observational simulation were varied to ascertain their effects on the final answer. These experiments were to vary the limiting thermal flux for the albedo observing survey up or down by one order of magnitude (labeled **high thermal flux** and **low thermal flux**) , to vary the limiting visual magnitude for the spectral measuring program up or down by one visual magnitude (labeled **dimmer spectral mag limit** and **brighter spectral mag limit**), to use an alternate (a,e,i) NEA population distribution (labeled **Bottke (a,e,i) distribution**), and to use the same value of G=0.15 for all NEAs rather than having the phase slope parameter vary with the albedo (labeled **no G variation**). None of these experiments made a substantial difference to the final answer.

Another variation that I tried in the simulation to determine the observational bias was to average over the sizes of the test particles within the simulation (labeled **diameter averaging**). In this case, the 30,000 test asteroids that were generated for each of the 36 NEAs with measured albedos were not all assigned the same diameter. Diameters were chosen randomly in the range 1 km to 5 km according to the diameter distribution given by equation (4.2). After propagating 30,000 test asteroids with random orbits, random diameters, and the same albedo value through the discovery, spectral measuring, and albedo measuring surveys, I obtained a bias correction factor for each of the 36 NEAs. Within each taxonomic complex, the bias correction factors were normalized to sum to one, and then used as diameter-limited fractional abundances (g_i) to average together the measured albedos for a given taxonomic complex using equation (4.8) to get the average albedo for each taxonomic complex.

As another point of comparison, I calculated an overall average albedo for the NEAs without using the spectral classifications at all (labeled **no spectral data**). The 36 measured albedo values were assumed to be a magnitude-limited sample of the albedos of the NEA population and were averaged with equation (4.7). This last case does produce results that are substantially different from the magnitude-limited assumption that uses the spectral classifications. The use of the taxonomic complexes to combine the albedos is likely to produce a better answer than combining the albedos directly. First, the albedo survey was conducted with some consideration toward obtaining albedo measurements within each of the complexes to constrain the albedos of each complex. This could introduce some additional bias when the complexes are all combined into one. Because the NEA albedos are correlated with their taxonomic complex, the albedo survey would no longer be magnitude limited. Second, there are an order of magnitude more measurements of NEA taxonomies than of NEA albedos, and the albedos do not vary nearly as much within a taxonomic complex as between taxonomic complexes. The overall variation in the measured albedos in this sample is a factor of 27 (from a Q-type asteroid with albedo of 0.63 to a P-type with albedo of 0.023). The variation within the X complex is a factor of 24. The next largest variation is within the Q complex with albedos that vary by a factor of 4.5. Thus, using the taxonomic complexes to weight the

albedo measurements results in a reduction of the uncertainty inherent in averaging a small sample from a widely varying population.

	average albedo	1 km equivalent H magnitude	number bigger than 1 km
magnitude-limited debiasing	0.155±0.02	17.63±0.1	885±146
survey simulation	0.161	17.60	858
high thermal flux	0.168	17.55	819
low thermal flux	0.151	17.61	913
brighter spectral mag limit	0.161	17.60	858
dimmer spectral mag limit	0.161	17.60	858
Bottke (a,e,i) distribution	0.163	17.59	847
no G variation	0.163	17.59	847
diameter averaging	0.160	17.60	858
no spectral data	0.119	17.93	1155

Table 4.5 Comparison of Debiasing Techniques. The magnitude-limited debiasing case is as described above in section 4.7. The survey simulation is as described above in this section. All of the other cases are similar to the survey simulation case with a single parameter value changed. For the high thermal flux case, the flux limit for successful observations from the Keck albedo survey was changed from 2 mJy to 20 mJy, and for the low thermal flux case it was changed to 0.2 mJy. The brighter spectral mag limit case is similar to the survey simulation case but with the limiting magnitude for successful spectral observing changed from 19.5 to 18.5 visual magnitudes. For the dimmer spectral mag limit case, that quantity was changed to 20.5 visual magnitudes. For the Bottke (a,e,i) distribution case, the test asteroids were generated according to the (a,e,i) distribution in Bottke, *et al.* 2002, all other parameters were the same as in the survey simulation case. For the no G variation case, all NEAs had assigned phase slope parameters G=0.15 rather than having G linearly dependent upon the albedo as in the survey simulation case. For the diameter averaging case, as described above, the test NEAs were assigned random diameters. The case of no spectral data was obtained by assuming that the albedo measurements were a magnitude-limited sample without using spectral data. With the exception of case where spectral data was excluded from the analysis, none of the variations are significantly different from the base case of magnitude-limited debiasing.

As seen in Table 4.5 the simulations of the observational programs produce debiased results that are very similar to the simple assumption of the magnitude-limited debiasing of section 4.7. Therefore, I have chosen to use the results of the simpler approach to proceed with an analysis of how the debiasing is affected by correlations between the taxonomic complexes and the Jovian Tisserand parameter.

4.9 Debiasing with Tisserand Parameter

Because of the association of dark objects with potentially cometary orbits (sections 4.4 and 4.5), I have performed another debiasing of the NEAs with objects on $T_J < 3$ orbits separated from objects on $T_J > 3$ orbits. Only one NEA with $T_J < 3$ has a NEATM albedo measurement (2000 PG3), and only 7 NEAs with $T_J < 3$ have albedo values from any source (Table 4.3). Therefore, the average albedos for the taxonomic complexes from the magnitude-limited case given above (Figure 4.17) are used for both the $T_J < 3$

objects and the $T_J > 3$ objects. However, the fractional abundances of the taxonomic complexes are allowed to vary between the $T_J < 3$ and $T_J > 3$ groups. This debiasing is the same as the magnitude-limited debiasing described in section 4.7. The split between the $T_J < 3$ and $T_J > 3$ groups is handled by simply doubling the number of complexes of NEAs, with fewer members in each complex. So, for example, the S-type NEAs are divided into a $T_J < 3$ group and a $T_J > 3$ group with the same albedo, and independent fractional abundances.

Figure 4.20 and Figure 4.21 show the observed and debiased fractional abundances of the taxonomic complexes for the two regions. In both cases the debiasing amplifies the number of NEAs in the dark complexes and reduces the proportion of NEAs in the brighter complexes. In Figure 4.22 the difference between the $T_J < 3$ and $T_J > 3$ NEAs is dramatically apparent with the $T_J < 3$ being much more dominated by very dark objects. Figure 4.21 shows that the debiased fractional abundances in the $T_J > 3$ NEAs are similar to the NEAs as a whole shown in Figure 4.18, though with some shift toward the bright complexes. Table 4.6 lists the overall properties for the two regions. Comparison of Table 4.4 and Table 4.6 shows that the separation of the NEAs into two regions by the Tisserand parameter has a small effect overall, making the total population slightly darker.

	$T_J < 3$	$T_J > 3$	Combined
average albedo	0.084±0.01	0.165±0.06	0.140±0.02
1 km equivalent H magnitude	18.31±0.1	17.57±0.2	17.75±0.1
number bigger than 1 km	295±50	686±110	982±160

Table 4.6 Summary of Average NEA Properties for Debiasing with Tisserand Parameter. Average albedo, absolute magnitude equivalent to a 1 km diameter NEA, and predicted number of NEAs with diameters larger than 1 km for the NEAs with Jovian Tisserand Parameter greater than or less than 3 are given. Comparison to Table 4.4 shows that separating the taxonomic complex by Tisserand parameter causes an slight overall darkening of the average albedo and slight increase in the number of 1 km NEAs.

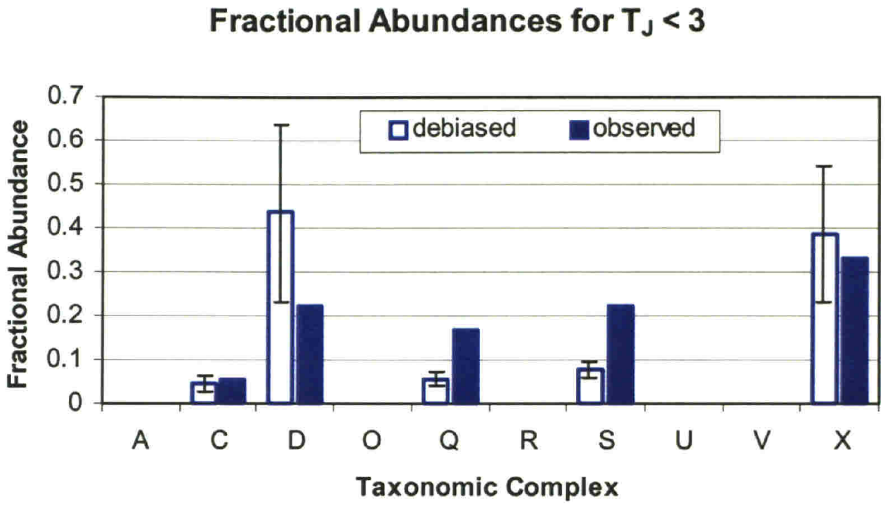

Figure 4.20 Fractional Abundances versus Taxonomy for NEAs with Jovian Tisserand Parameter Less than 3. The observed fractional abundances are simple counts of the $T_J<3$ NEAs with spectra in each complex. Debiased fractional abundances of the taxonomic complexes are computed with the magnitude-limited debiasing of section 4.7. The dark NEA complexes, particularly the D-types dominate in the $T_J<3$ region.

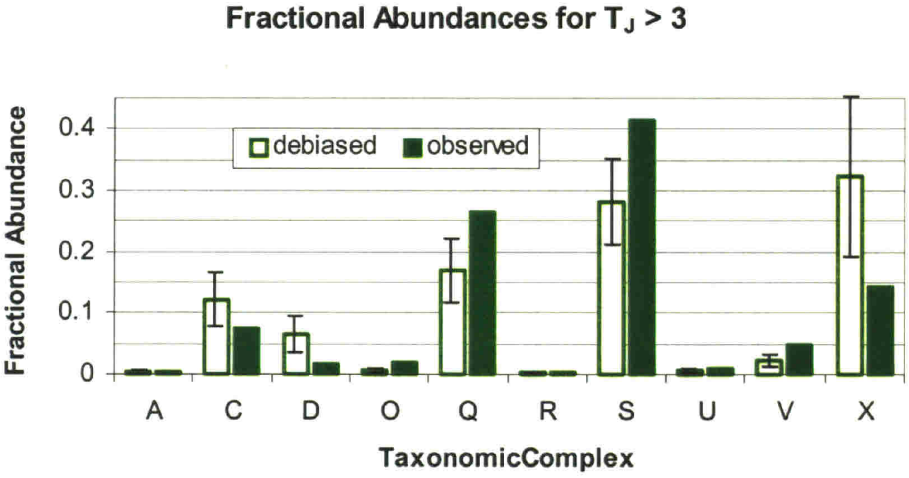

Figure 4.21 Fractional Abundances versus Taxonomy for NEAs with Jovian Tisserand Parameter Greater than 3. The observed fractional abundances are simple counts of the $T_J>3$ NEAs with spectra in each complex. Debiased fractional abundances of the taxonomic complexes are computed with the magnitude-limited debiasing of section 4.7. The bright NEA complexes (S,Q), are abundant in the $T_J>3$ region, but there is a large contribution from the relatively dark X-types.

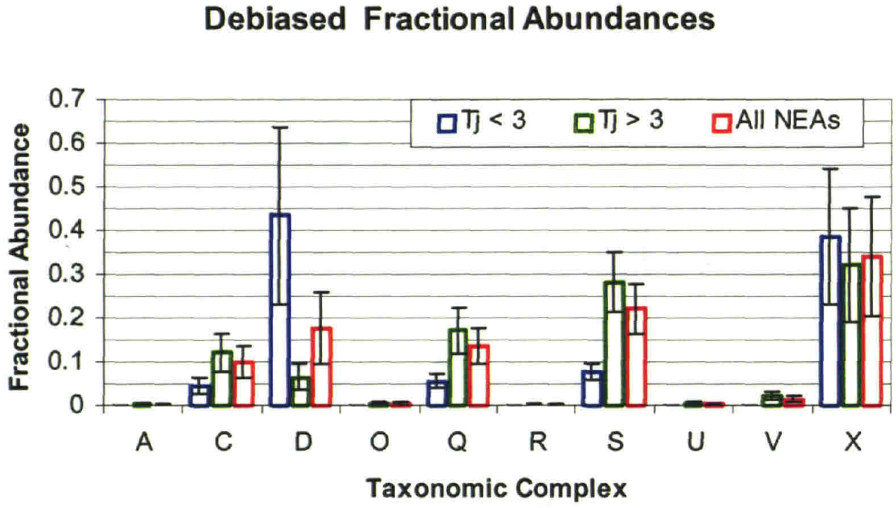

Figure 4.22 Debiased, or Diameter-Limited, Fractional Abundances versus Taxonomy. The NEAs are separated into groups with Jovian Tisserand parameter greater than or less than 3, and shown as a whole. Overall, the S- and X-type NEAs are the most abundant. However, in the T_J<3 region, the dark complexes, particularly the D-types dominate. The bars are in left-right order as indicated in the caption.

There is a compelling case to be made that the fractional abundances of the taxonomic complexes differ between the NEAs with T_J<3 and T_J>3 (Figure 4.7, Figure 4.8, Figure 4.9, and Figure 4.10). Therefore the debiasing that includes this dichotomy is the best result. The final debiased fractional abundances and average albedos of the ten taxonomic complexes are given in Table 4.7.

Taxonomic Complex	Tj<3 Fractional Abundance	Tj>3 Fractional Abundance	Total Fractional Abundance	Albedo
A	0.000+0.000	0.003+0.003	0.002+0.002	0.200+0.020
C	0.046+0.017	0.121+0.044	0.099+0.036	0.101+0.027
D	0.435+0.204	0.065+0.030	0.176+0.082	0.042+0.013
O	0.000+0.000	0.007+0.004	0.005+0.002	0.520+0.156
Q	0.056+0.017	0.171+0.052	0.136+0.041	0.257+0.063
R	0.000+0.000	0.002+0.002	0.001+0.001	0.340+0.034
S	0.078+0.019	0.282+0.070	0.221+0.055	0.244+0.045
U	0.000+0.000	0.006+0.003	0.004+0.002	0.300+0.030
V	0.000+0.000	0.022+0.010	0.015+0.007	0.364+0.128
X	0.385+0.156	0.322+0.130	0.341+0.138	0.072+0.025

Table 4.7 Fractional Abundances and Albedos. This table gives the best estimate for the fractional abundances and albedos of the ten taxonomic complexes using the magnitude-limited debiasing method and separating each of the complexes according to the Jovian Tisserand parameter. The T_J<3 and T_J>3 columns are each normalized to unity. Summing over the taxonomic complexes, the NEAs with T_J<3 account for 30% of the NEAs, and those with T_J>3 account for 70% in a debiased, diameter-limited sample. These numbers are represented graphically in Figure 4.17, Figure 4.20, Figure 4.21, and Figure 4.22.

4.10 Diameter Distribution of the NEAs

So far, this analysis of the albedos and taxonomic categories of the NEAs has assumed that the number of NEAs is an exponential function of the absolute magnitude. The absolute magnitude distribution was given in Figure 2.8, and the best fit for the cumulative distribution was found to be $N(<H) = 10^{-3.88+0.39H}$. This power law is obtained from a fit to the binned, non-cumulative absolute magnitude distribution (Figure 2.7) which is not exactly a simple exponential function. Using the albedos and fractional abundances from Table 4.7, I convert the binned, non-cumulative absolute magnitude distribution into a diameter distribution without first simplifying it to an exponential form. This is done as follows:

1. Assume that each taxonomic complex follows the binned, non-cumulative absolute magnitude distribution in Figure 2.7.
2. For each complex, use the debiased, average albedo and fractional complex abundance, from Table 4.7 to convert the absolute magnitude distribution to a binned, non-cumulative diameter distribution. This is done by using equation (A.2) to convert the absolute magnitude of each bin to a diameter, and to use the fractional abundances to scale the number of NEAs in the bin to the proper number of NEAs for each complex. This produces 20 separate binned diameter distributions, one for each taxonomic complex, with the $T_J < 3$ and $T_J > 3$ groups separated as well.
3. Sort all of these bins from all 20 diameter distributions in order from largest to smallest diameter, and then create a cumulative sum.

The resulting cumulative diameter distribution is shown in Figure 4.23.

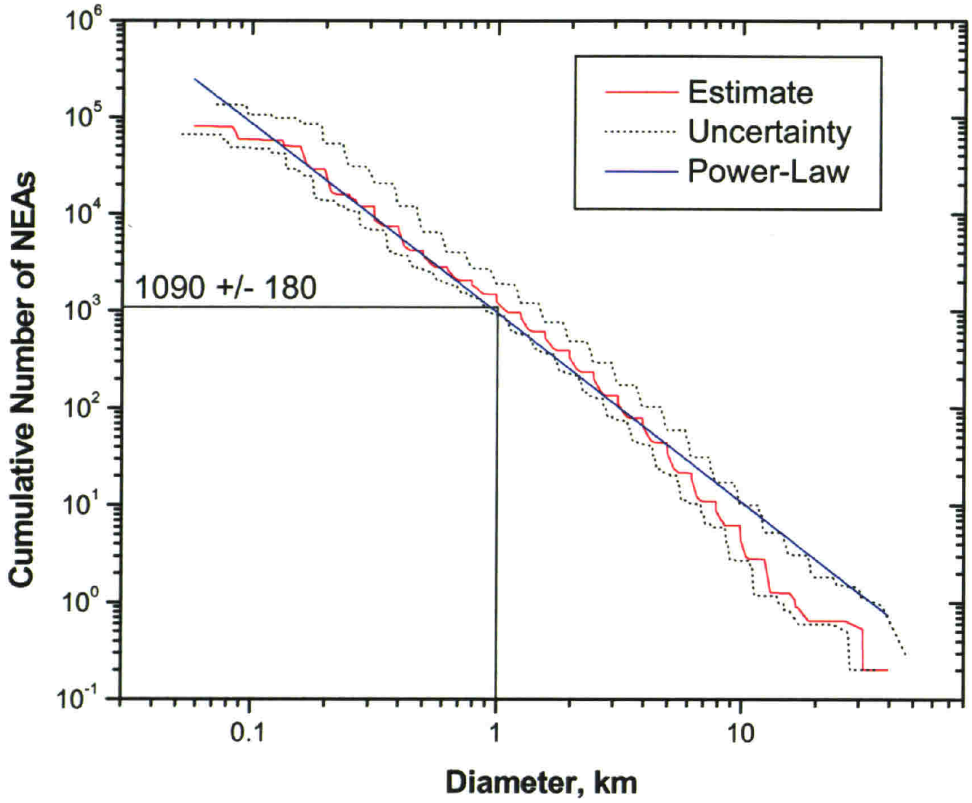

Figure 4.23 Cumulative Diameter Distribution. The central red curve shows the cumulative number of NEAs larger than a given diameter. The absolute magnitude distribution from **Figure 2.8** is converted to a diameter distribution using the albedos and fractional abundances for the taxonomic complexes from Table 4.7. The dotted lines represent an approximate error envelope. The upper side of the error envelope is computed by allowing the number of NEAs in each absolute magnitude bin to be one standard deviation above the best estimate for that bin, and allowing the albedo of each taxonomic complex to be one standard deviation lower than the best estimate for that complex and following the same procedure used to calculate the central red curve (described in the text). The lower side of the error envelope is similarly calculated by allowing the number of NEAs in each H bin to be one standard deviation low, and the albedo of each taxonomic complex to be one standard deviation high. Since the two sources of error are not added in quadrature, the error envelope is somewhat larger than one standard deviation. The straight blue line is not a fit to the red curve, but is the power-law distribution derived by assuming an exponential absolute magnitude distribution. The blue line has a power-law slope (α from equation (4.2)) of –1.95, and 962 NEAs larger than 1 km, as in Table 4.6. The number of NEAs with diameters larger than 1 km is 1090±180.

This final cumulative diameter distribution for the NEAs suffers from two problems. One problem is minor, the other is unavoidable. The first problem is that the analysis leading to the average complex albedos and the debiased fractional abundances assumed an exponential form for the number of NEAs as a function of absolute

magnitude. The real absolute magnitude distribution was then added back in at the end of the analysis to obtain a diameter distribution. A more rigorous approach would be to use the full absolute magnitude distribution from the beginning. However, this would eliminate the possibility of using the magnitude-limited debiasing equations given in section 4.6, because the derivation of those equations requires an analytical form for the absolute magnitude distribution. Including the full absolute magnitude distribution in the calculations of the observational bias is not warranted because it would be a minor effect on the bias correction factors and the resulting debiased fractional abundances and average albedos. This more complicated approach also suffers from the second, unavoidable problem.

The second problem with using the binned, noncumulative absolute magnitude distribution along with the debiased fractional abundances and average albedos to generate a diameter distribution is that it reverses the proper causal order. Using this method makes the assumption that all of the taxonomic complexes have the same absolute magnitude distribution with its various bumps and wiggles lined up at the same place in absolute magnitude. Those bumps and wiggles then get shifted when the absolute magnitude distribution is converted to a diameter distribution for each taxonomic complex. When the diameter distributions for the complexes are summed to obtain the cumulative diameter distribution, the bumps and wiggles that were all lined up in absolute magnitude space get averaged out in diameter space. This is very unlikely to be the case in the real world. The more likely scenario is that the taxonomic complexes have differently shaped diameter distributions reflecting differences in material properties. Alternatively, all of the taxonomic complex could have the same diameter distributions. Any bumps and wiggles in the diameter distribution would get smoothed out when converting to an absolute magnitude distribution. In either case, the absolute magnitude distributions for the different taxonomic complexes are very unlikely to be perfectly aligned. However, there is really no alternative to making this assumption. Every NEA that has been discovered has a measured absolute magnitude, whereas only about 3% of them have measured diameters. The absolute magnitude distribution is better constrained than the diameter distribution. Until the albedos and diameters of

nearly all of the NEAs have been measured, the best estimate of the diameter distribution will have to based on the absolute magnitude distribution.

The cumulative diameter distribution shown in Figure 4.23 represents the best current estimate of the overall diameter distribution for the NEAs. In the absolute magnitude distribution used to make the diameter distribution, the bin with the largest absolute magnitude was $H=22.5$. For the complex with the lowest albedo, (D-types with albedo of 0.04) that absolute magnitude bin corresponds to a diameter of 0.18 km. Below that size, the diameter distribution shown in Figure 4.23 is artificially incomplete because of the truncation of the absolute magnitude distribution. This method of computing the diameter distribution gives a slightly higher estimate for the number of NEAs larger 1 km than the estimate given in Table 4.6. The cumulative diameter distribution pegs the number of NEAs with diameters larger than 1 km at 1090±180.

4.11 Summary

I have presented several different methods for debiasing the albedos and complex abundances of the NEAs. Here is a summary to highlight the techniques and assumption that were eventually used to arrive at the final, best answer (Table 4.7 and Figure 4.23). First, the equations of section 4.7 that describe debiasing an absolute-magnitude limited sample were found to give nearly identical results to the various simulations of observational bias, and so those equations were chosen as the best method for debiasing. The measured albedos in each taxonomic complex were then assumed to be an absolute-magnitude limited sample. Equation (4.7) was then used to obtain an average, debiased albedo within each complex.

Next, I found that the taxonomic abundances differ for objects on different sides of the T_J=3 boundary. Because of the scarcity of albedo measurements, there is no way to separately debias the albedos of each complex while also separating according to the T_J=3 boundary. Therefore, the albedos within each complex were assumed to be the same on either side of the boundary. All of the NEAs on the $T_J < 3$ side were assumed to be an absolute magnitude-limited sample, with each complex having its own albedo, and the fractional abundances of the complexes were debiased with equation (4.5). The same procedure was performed separately for the NEAs with $T_J > 3$. After debiasing, the two

regions can be recombined to give the fractional abundances of the taxonomic complexes for the NEAs as a whole. Those three sets of fractional abundances, for $T_J < 3$, $T_J > 3$, and all NEAs are given in Figure 4.22 and Table 4.7.

Lastly, I addressed the issue of the diameter distribution of the NEAs. The foregoing debiasing calculations assumed that the absolute magnitude and diameter distributions of the NEAs follow simple formulas (equations (4.3) and (4.4)). To partially relax that assumption, the binned, absolute-magnitude distribution from section 2.7, Figure 2.7 was converted to diameter distributions using the debiased albedos and fractional abundances of each of the taxonomic complexes, while also accounting for the separation between $T_J < 3$ and $T_J > 3$ NEAs. Those diameter distributions were then summed to compute a cumulative diameter distribution (Figure 4.23) for the NEAs.

4.12 Discussion

I've presented the results of debiasing the measured albedos of the NEAs. Two different methods were presented for accounting for the observational bias, and several variations on one of the methods was presented to gauge the effects of parameters that were uncertain in the simulations. The debiasing technique uses an averaging algorithm that ensures that the number of NEAs bigger than a given size will be the same as the number of NEAs brighter than the equivalent absolute magnitude limit. For the purpose of counting asteroids, this type of average is an improvement over the geometric mean which is more appropriate when averaging the observed magnitude of objects with different albedos.

The two debiasing methods and all of the variations produce essentially equivalent results. The average albedos for the taxonomic complexes come out being similar to the main-belt but generally a little bit higher than the main-belt averages. Table 4.8 summarizes this for the three complexes for which there are an appreciable number of both MBA and NEA albedos available. For the C-types, the NEAs are nearly twice as reflective as their main-belt counterparts, while the S-type NEAs are only slightly brighter, and the X-types are statistically the same. That the NEAs tend to be slightly brighter than MBAs could be indicative of a correlation between albedo and size. Observed NEAs tend to be smaller than observed MBAs (because the greater distance of

the MBAs makes the small ones too faint to observe). A correlation between size and albedo was not evident over the relatively small range of sizes of the NEAs analyzed in this paper. If there is a trend that asteroids tend to be brighter at smaller sizes, then it may only be evident in an analysis that combines large MBAs with small NEAs. However, such a trend could also be indicative of a difference in albedo between MBAs and NEAs that is independent of size. The NEAs are a highly selective subsample of the MBAs from regions near resonances. Asteroids near those regions could have brighter albedos than the overall main-belt population.

Taxonomic Complex	Main-Belt Albedo	NEA Albedo
C	0.06±0.04	0.101±0.027
S	0.20±0.06	0.244±0.045
X	0.10±0.09	0.072±0.025

Table 4.8 Comparison of Main-Belt and NEA Albedos. The albedos for the main-belt are as defined in footnote (2, pg. 76). The albedos for the NEAs are the debiased average albedos for the complex as in Figure 4.17. The debiased albedos for the S and X complexes are indistinguishable from the average main-belt values, however the C-type NEAs are somewhat darker than their main-belt counterparts.

The debiased fractional abundances of the NEAs do not match with the debiased fractional abundances of large MBAs. Bus and Binzel (2002b) present, in figure 19, debiased fractional abundances of the taxonomic complexes within the main-belt. The fractional abundances for the NEAs presented here do not match very well with the abundances for the MBAs. This is not surprising. The fractional abundances for MBAs as presented by Bus and Binzel (2002b) are for asteroids with diameters larger than 20 km. A collisional family of asteroids with diameters smaller than 20 km near one of the major resonance zones could contribute a substantial number of asteroids to the NEA population with taxonomic complexes that are not characteristic of the large asteroids near the same resonance zone. Indeed, the taxonomic abundances of the NEA population may be the best way to reconstruct the spectral characteristics of the small asteroids that feed the resonance zones, if the NEAs can be traced back to their origins in the main-belt.

The debiasing procedure I used assumed that there was no correlation between the albedos or spectra and the orbital parameters or size, other than the trend produced by the Tisserand parameter. I made this assumption after inspecting the spectral and albedo data to look for trends. I found no convincing evidence for such trends. If such correlations are found in the future when more spectral or albedo data are available, a more

sophisticated debiasing technique will be needed to correct for observational bias while taking into account these trends. With sufficient data, it may be possible to divide the orbital parameter space and absolute magnitude space into a number of cells and perform a survey simulation within each cell (similar to the technique used to define the (a,e,i,H) population) and debias the taxonomic complexes and albedos within each cell. This would require a substantial increase in the number of measured spectra and albedos.

The X-types form a substantial fraction of the NEAs. As can be seen in Figure 4.18, the relatively low average albedo of the X-types significantly boosts their fractional abundance after debiasing. Since the albedos of the X-types span a large range (from 0.023 to 0.55) the debiased albedo for the complex is particularly dependent upon the small number of measurements of very dark objects. However, the resulting average albedo (0.072±0.025) is similar to values for the main-belt X-types (0.10, using IRAS albedos for E, M, and P type asteroids within SMASSII, and averaging with equation (4.8), assuming that the IRAS sample is diameter limited and that the population slope parameter $\beta = 0.5$, which is equivalent to a collisionally evolved population with diameter population slope parameter $\alpha = 2.5$), so the debiasing technique is producing a reasonable estimate for the average NEA albedos. It would be useful to obtain more albedo measurements of the X-type NEAs to further refine this average.

If I combine the taxonomic complexes into two groups (complexes A, O, Q, R, S, U, and V become the bright group, and C, D, and X become the dark group), the bright objects account for 38% of the NEAs, and the dark objects account for 62%. This produces a dark:bright ratio of 1.60. The observed dark:bright ratio (before debiasing) is 0.35. The overall observational bias (factor by which bright objects are observationally favored over dark objects) is 1.46/0.35=4.61. In section 3.5, I calculated a similar bias ratio between S- and C-type NEAs (Table 3.3). The debiased S:C ratio from Table 4.7 is 2.22, and the observed S:C ratio is 4.0. Thus the observational bias is $B_{S:C}$=2.50. This is slightly larger than the value of $B_{S:C}$ given in Table 3.3 (1.79 ± 0.03 for the α=2.0 case). That simulation modeled the discovery of the LINEAR survey on a population of NEAs with diameters from 1 to 5 km. It did not model the population to sizes as small as those sampled by the SMASS NEA survey and those results were dependent on the overall completeness level of the survey. Since that model survey discovered a high percentage

of all of the NEAs in the model population, the resulting observational bias factor was closer to unity than for the SMASS NEA sample which is less complete.

Other researchers recently found a different dark:bright ratio among the NEAs of 0.87 (Morbidelli *et al.* 2002b). That work debiased the albedos of the NEA population using a dynamical model of transport of NEAs from the main-belt to near-Earth space along with a model of the albedo distributions of the small main-belt asteroids within the main-belt source regions that are thought to supply the NEAs. Those authors further find that the absolute magnitude threshold that corresponds to a 1 km diameter NEA is 17.85, or an average albedo 0.13. That value is similar to the value found here (0.140±0.02).

I have presented an average albedo for the NEAs as a whole so that the estimates of the NEA population that are presented as a function of absolute magnitude may be converted to population estimates as a function of diameter. The average albedo is slightly brighter than the generally assumed value of 0.11. Because most recently published estimates of the number of 1 km NEAs assumed the value of 0.11 when converting absolute magnitude to diameter, the estimates for the number of 1 km NEAs has been somewhat high. I have found that there are about 1090 (±180) NEAs with diameters larger than 1 km. Currently (18 April 2003), Minor Planet Center catalog lists 543 known NEAs with absolute magnitudes $H<17.75$. This implies that the current catalog of known NEAs larger than 1 km in diameter is about 50% complete for NEAs bigger than 1 km.

Chapter 5 The NEA Impact Hazard

5.1 Abstract

With a new model of the orbital distribution and sizes of the near-Earth asteroids, it is useful to revisit the issue of asteroid impacts on the Earth and Moon. This issue has been addressed many times in the last few decades (Shoemaker *et al.* 1990, Morrison 1992, Morbidelli *et al.* 2002b). However, the answer is dependent upon the model one chooses for the NEA population. A new model of the NEA population warrants a new analysis of the NEA impact threat. The ability to predict the lunar crater record, under the assumption of a steady-state population of NEAs, is a critical test for a new NEA population model. The analysis proceeds in three major steps. Step one is to analyze the probability of impact for NEAs into the Earth or Moon. This step depends upon the orbital element distribution of the NEA population, and when combined with the size distribution yields estimates of the frequency of impacts as a function of impactor diameter, or impact energy. The second step is to determine the sizes of craters produced by impactors with specific parameters and to combine this with the impact probabilities to obtain the expected rate of production of craters of various sizes. The third step is to determine how many craters have already been made on the Earth and Moon and to compare this historical cratering record with the predicted rate of crater formation from the current NEA population.

5.2 Introduction

The first step in understanding the NEA impact hazard to the Earth is to establish the frequency with which NEAs collide with the Earth. For an individual NEA with a well determined orbit, the future trajectory can usually be calculated with enough accuracy to rule out the possibility of an impact within the next century, or to provide an estimate of the likelihood of that NEA hitting the Earth at specific times in the future. In this work, however, I seek to understand the long term collision hazard from all of the NEAs. Many of the NEAs have not yet been discovered or had orbits accurately determined, so I cannot use the precise methods of orbit propagation to predict future impact events. Rather, I will use analytical formulas that give the probability of an NEA hitting the Earth over long time spans. These formulas depend only on the NEA's

semimajor axis, eccentricity, and inclination. The distribution of NEAs over those orbital parameters was determined in section 2.7. Those results can be combined with the collision probabilities to obtain the overall collision probability for the entire population of NEAs.

Öpik (1951) first developed a statistical model for calculating the probability of a test object in a Keplerian orbit hitting a target in a circular Keplerian orbit. Öpik's theory assumes that the test object and the target (e.g. an asteroid and a planet) both have uniformly distributed mean anomaly, argument of perihelion, and longitude of the ascending node. Öpik's theory also assumes that when the test object is very near to the target object, the motion of the two bodies is linear, and that the test object's orbit is not perturbed, either by close approaches to the target, or by secular perturbations from other sources. Öpik also introduced some correction factors to apply his theory to cases in which the target's orbit is eccentric. Wetherill (1967) provided a more rigorous extension to the case when both bodies are on eccentric orbits. Shoemaker *et al.* (1979) present a method of calculating impact probability, an extension of Wetherill's approach, that includes corrections for secular perturbations of the test object's eccentricity, inclination, and argument of perihelion. The corrections for secular perturbations are important when assessing the long-term collision hazard from a small number of NEAs, but are not important when averaging the impact probabilities from a large number of NEAs in an orbital distribution that is presumed to be in steady-state. Effects of secular perturbations are not included in the impact probability calculations used here. Greenberg (1982) improved upon Wetherill's calculation by removing the need for a stochastic integration technique to deal with certain singularities in the calculation. The singularity arises when the potential collision occurs at an apse of the particle's orbit, and is a result of the approximation that the motion near the intersection point is linear. Greenberg's rederivation of the calculation is symmetrical enough in its treatment of the two bodies that one may simply switch the labels between the test object and the target body for part of the integration until the singularity is passed. Namiki and Binzel (1991) point out an error in the equations presented in Greenberg (1982) and use a similar approach to derive impact probabilities. Bottke and Greenberg (1993) also point out the same error in Greenberg's presentation, and further point out that the method of Namiki and Binzel

does not correct for the singularity in the integration. Farinella and Davis (1992) present a similar method for calculating collision probabilities in which they deal with the singularity by choosing sufficiently small integration step-sizes to achieve, in principle, arbitrarily good precision. Manley *et al.* (1998) present a scheme similar to Greenberg's that produces the same results as Greenberg's method.

5.3 Impact Probability Calculations

I use Greenberg's method to calculate the collision probabilities and collision velocities of NEAs into the Earth and the Moon. Greenberg's method simplifies dramatically when the target body is in a circular orbit, and so I assume that the Earth is in a circular orbit 1 AU from the sun. In fact, this simplification obviates the numerical integration, and the solution reduces to a simple analytical formula that can be evaluated very quickly for all of the *a-e-i* bins that were used to estimate the NEA population in Chapter 2. For each bin, the *a*, *e*, and *i* values from the center of the bin were used to calculate the collision probabilities for all the asteroids within the bin. The bins with center values of a=1.05, e=0.05 were the closest to having a problem with the singularity mentioned above. In those bins, the collision occurs at a mean anomaly of 2.8°, which is far enough away from perihelion that there is no difficulty with the singularity. Therefore, there is no problem with singularities in any of the bins for which I am calculating collision probabilities. Also, *a-e-i* bins which do not actually cross the Earth's orbit (perihelion is greater than 1 AU) have zero probability of colliding with the Earth, and are simply skipped in the calculations.

For the case of an NEA colliding into the Earth or the Moon, the target body is sufficiently more massive than the test object, that I ignore the geometrical size and the gravity of the NEA. The collision probability and collision velocity depend upon the size and mass of the target body. The collision probability is directly related to the capture cross-section of the target body which is defined as $\sigma = R^2\left(1+\frac{v_{esc}^2}{v_{enc}^2}\right)$, where R is the radius of the target body, v_{enc} is the encounter velocity between the two bodies, or the relative velocity before accounting for the gravitational attraction of the target body, and v_{esc} is the escape velocity of the target body ($v_{esc}^2 = 2GM/R$, where G is the universal

constant of gravitation, and M is the mass of the target body). The actual collision velocity is $v_{coll}^2 = v_{esc}^2 + v_{enc}^2$. The escape velocity for the Earth is 11.2 km/s, and for the Moon it is 2.38 km/s. For both the capture cross section and the collision velocity, the effect of the gravitational attraction of the target body is largest when the encounter velocity, v_{enc}, is low. For collisions in which the encounter velocity is much larger than the escape velocity, the target body's gravity has very little effect on either the collision probability or the collision velocity. If the test body is too large to ignore its gravity, then the capture cross-section, and the escape velocity (and hence the collision velocity) can be calculated by simply using the combined radius and mass of the two objects ($R = R_1 + R_2, M = M_1 + M_2$).

For a complete derivation of the equations for calculating impact probabilities, with descriptions of their meanings, see Greenberg (1982). I will present the equations that I used for calculating the impact probability that are heavily based on Greenberg's equations, but with simplifications to account for the fact that the target body is in a circular orbit. While I have generally used astronomical units as the unit of length in discussing orbits, it more convenient to do the impact probability calculations in meters or kilometers so that the resulting velocities are in standard units. If the radius of the target body is expressed in the same length units, and the orbital periods are calculated in seconds, the final probability has units of inverse seconds. Let a_I, e_I, i_I be the semi-major axis, eccentricity, and inclination of the test asteroid (i.e. one of the bin centers from the *a-e-i* bins defined in Chapter 2). Let a_E = 1 AU be the semi-major axis of the Earth, with the Earth's eccentricity and inclination both assumed to be 0. Let the heliocentric gravitational constant be G_S (this is where one must be careful of the units to ensure consistency). The orbital periods of the asteroid and Earth, respectively, are

$$T_1 = \frac{2\pi a_1^{2/3}}{\sqrt{G_S}}$$
$$T_E = \frac{2\pi a_E^{2/3}}{\sqrt{G_S}} \qquad (5.1)$$

The semilatus rectum of the asteroid's orbit is $p_1 = a_1\left(1-e_1^2\right)$. The cosine and sine of the true anomaly at which impact occurs are $C_1 = \dfrac{\dfrac{p_1}{a_e}-1}{e_1}, S_1 = \sqrt{1-C_1^2}$. Greenberg defines a coordinate system that is local to the collision point. The following Cartesian coordinates all refer to that coordinate system. The projections of the collision angle, α_1 and its trigonometric functions, are calculated as

$$\begin{aligned}
\alpha_{1,y} &= 1+e_1C_1 \\
\alpha_{1,x} &= e_1S_1 \\
\alpha_{1,z} &= \sqrt{1+2e_1C_1+e_1^2} \\
\cot(\alpha_1) &= \frac{e_1S_1}{\alpha_{1,y}} \\
\sin(\alpha_1) &= \alpha_{1,y}/\alpha_{1,z} \\
\cos(\alpha_1) &= \alpha_{1,x}/\alpha_{1,z}
\end{aligned} \tag{5.2}$$

The heliocentric velocity, and its projections onto the local coordinate system can now be calculated as

$$\begin{aligned}
u_1 &= \alpha_{1,z}\sqrt{G_S/p_1} \\
u_{1,x} &= u_1\cos(\alpha_1) \\
u_{1,y} &= u_1\sin(\alpha_1)\cos(i_1) \\
u_{1,z} &= u_1\sin(\alpha_1)\sin(i_1)
\end{aligned} \tag{5.3}$$

In the local coordinate system, the Earth's velocity is always the same, $u_E = \sqrt{G_S/a_E}, u_{E,x} = 0, u_{E,y} = u_E, u_{E,z} = 0$. The relative encounter velocity is then just the difference between the asteroid's velocity and the Earth's velocity:

$$\begin{aligned}
V_x &= u_{E,x}-u_{1,x} \\
V_y &= u_{E,y}-u_{1,y} \\
V_z &= u_{E,z}-u_{1,z} \\
V &= \sqrt{V_x^2+V_y^2+V_z^2}
\end{aligned} \tag{5.4}$$

The encounter cross sectional area, σ, is a function of the target size and mass, and the encounter velocity and is defined in the paragraph above. Finally, the collision probability is

$$p_c = \sigma \frac{A}{p_1 e_1 S_1 \sin(i_1)} (1 + e_1 C_1)^2 \frac{2V}{T_1 T_E u_E \sqrt{V^2 - V_y^2}} \tag{5.5}$$

The probability of collision in each *a-e-i* bin is then multiplied by the fraction of NEAs in that bin (technically, I should use $1-(1-p_c)^N$, but the probabilities are small enough that the difference is negligible), and the *a-e-i* bins are summed to obtain the probability of collision averaged over all of the NEAs. Since my population model found no correlations between size and orbital parameters, this average collision probability can then be multiplied by the total number of NEAs larger than a given size (or brighter than a given absolute magnitude) to obtain the total collision probability for NEAs larger than the specified size.

The methods for calculating collision probability outlined above are for the case of a target body in a heliocentric orbit, not for a satellite in orbit around a planet. However, the collisional environment of the Moon should be nearly identical to that of the Earth. The only significant difference is that the Moon is much smaller than the Earth. To calculate the collision probabilities and velocities for the Moon, I used the same method as for the Earth, but with the smaller mass and radius of the Moon when calculating the capture cross section and escape velocity. The impact probabilities calculated for the Moon are really for a target body the same size and mass as the Moon in an Earth-like circular orbit 1 AU from the Sun. The Earth and Moon provide some "shadowing" to each other, because some objects that might hit the Earth will hit the Moon and vice-versa. This is a very small effect. For typical encounter velocities of NEAs and the Earth, the Earth's gravitational capture cross section, when viewed from the Moon, subtends less than 1% of the sphere. The Moon's gravitational capture cross section is 18 times smaller. The shadowing effect is also offset by a small amount of gravitational focusing because the combined masses of the Earth and Moon will pull in some objects that would barely miss either the Earth or the Moon separately. These corrections are all small enough to ignore in calculating average collision probabilities.

In summary, the impact probability calculations make the following simplifying assumptions:

- that the longitude of the ascending node, the longitude of perihelion, and the mean anomaly are uniformly distributed from 0 to 2π,
- that the orbital elements do not change over time (equivalent to assuming a steady-state population for the NEAs since I am averaging the impact probability over all the NEAs),
- that the target body (Earth or Moon) is in a circular orbit 1 AU from the Sun,
- and that motion near the collision point is linear.

In section 5.6, the impacting population will be compared with the cratering record on the Moon. For that comparison, a further assumption is made that NEA population has been in a steady-state over the lunar cratering record, which spans 3 Gyr.

The calculations of collision probability for a test asteroid into the Earth or Moon also produce the impact velocities. The velocity is necessary to calculate impact energy and to estimate crater diameter, discussed below. When the calculated impact velocities are weighted by the impact probability, and by the NEA population model from section 2.7, the root-mean-square impact velocity for NEAs hitting the Earth is 20.9 km/s. For that impact velocity, the gravitational capture radius of the Earth is 7540 km, as opposed to the Earth's equatorial radius which is 6378 km. The root-mean-square impact velocity for the Moon is 19.2 km/s, and the corresponding gravitational capture radius is 1751 km, compared to 1738 km for its geometric radius.

The population model from section 2.7 is fairly spiky, that is, many *a-e-i* bins have no NEAs in them and some bins have many NEAs. I also used a smoothed version of that population model to gauge the effects of this spikiness on the collision probability. The difference in the overall collision probability between the smoothed and unsmoothed population is only about 1%, a negligible amount. I use the unsmoothed version in the subsequent analysis and in the plots of collision probability.

When these impact probability calculations are averaged over the NEA orbital element distribution from section 2.7, the average impact probability for one NEA hitting the Earth is 1.50×10^{-9} yr^{-1}. Morrison *et al.* (2002) have also calculated the average impact probability, but with a different method. They used the 244 NEAs with absolute magnitudes less than 18 and perihelion distances less than 1.0 AU (*i.e.* those that cross

the Earth's orbit) that had been discovered as of July 3, 2001 to represent the NEA orbital element distribution. The orbits of those 244 NEAs were propagated for 100 years and all approaches to within 0.1 AU of the Earth were recorded. The encounter velocity of each approach was used to determine the Earth's gravitational capture cross-section for that encounter. The number of encounters was then scaled by the ratio of the gravitational capture cross-sectional area to the cross-sectional area of the study sphere (0.1 AU radius). Morrison *et al.* found that the "per NEA" impact probability is 1.68×10^{-9} yr^{-1}. Morrison *et al.* also found that the weighted, RMS impact velocity is 20.2 km/s, as opposed to 20.9 km/s calculated above. As discussed in Chapter 2 the known population of NEAs is somewhat biased, particularly toward low inclination asteroids. Thus, the high inclination NEAs are underrepresented in the sample used by Morrison *et al.* High inclination NEAs are less likely to strike the Earth than low inclination NEAs [equation (5.5)], and they have higher impact velocities. Thus, it is to be expected that the method used by Morrison *et al.* would yield an average impact probability that is slightly higher and an RMS impact velocity that is slightly lower than the method described above, which uses a debiased NEA population model.

5.4 Reassessing the Earth Impact Hazard

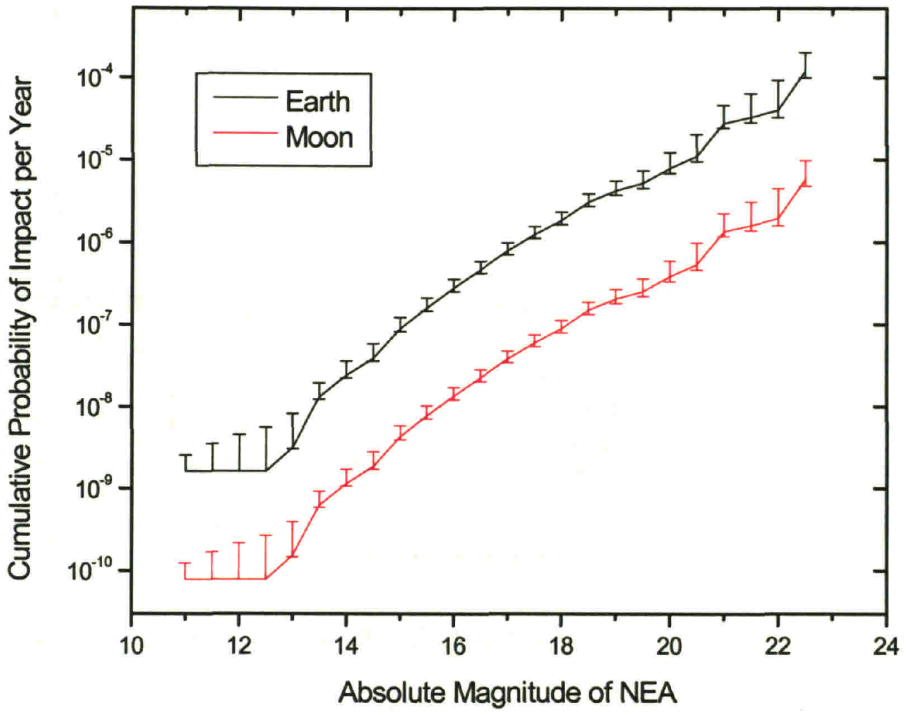

Figure 5.1 Probability of NEA Impact Versus Absolute Magnitude. The distribution of orbital elements and absolute magnitudes for the NEAs (section 2.7) is combined with impact probability calculations (section 5.3) to obtain the cumulative probability of impact for NEAs brighter than a specified absolute magnitude.

Figure 5.1 and Figure 5.2 show the cumulative collision probability for the Earth and Moon as a function of absolute magnitude and diameter, using the NEA population model of section 2.7, and the diameter distribution of section 4.10. The overall collision hazard for the Earth for asteroids with absolute magnitudes less than 18 is $1.8^{+0.5}_{-0.2} \times 10^{-6}$ per year, which translates to an average of 1 impact every $0.54^{+0.06}_{-0.1}$ Myr. In terms of impactor diameter, the collision hazard for the Earth is that impacts of 1 km or larger have a probability of $1.67^{+0.4}_{-0.3} \times 10^{-6}$ per year, or 1 impact every 0.60±0.1Myr.

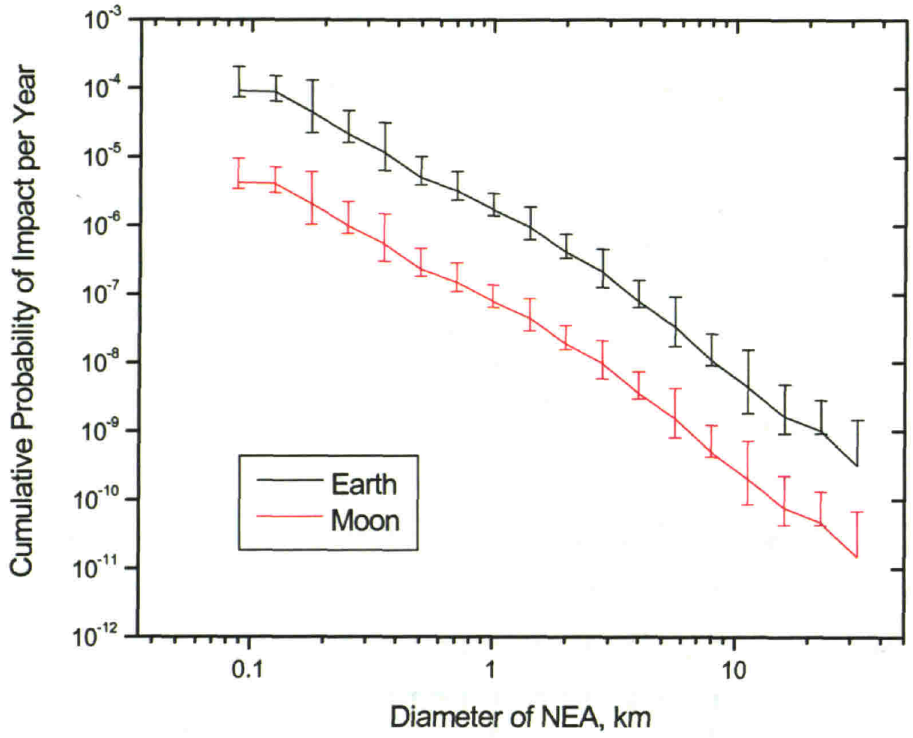

Figure 5.2 Probability of NEA Impact Versus Diameter. The distribution of orbital elements for the NEAs (section 2.7) is combined with the debiased diameter distribution (section 4.10), and impact probability calculations (section 5.3) to obtain the cumulative probability of impact for NEAs larger than a specified diameter.

The real determinant of the damage from an asteroid impact is the total impact energy. In order to calculate the impact energy, one must know the mass of the asteroid, not the diameter. Converting from diameter to mass requires knowledge of the bulk density (and for better accuracy, a complete shape model, rather than just a diameter). The densities of asteroids are even less well sampled than their diameters. However, for C-type and S-type asteroids, there does appear to be a fairly consistent trend (Britt *et al.* 2002). C-type asteroids have bulk densities clustered around 1400 kg/m^3, whereas S-type asteroids have bulk densities clustered around 2700 kg/m^3. This agrees with the broad understanding of asteroid formation and mineralogy, that C-types formed further out in the asteroid belt of lighter, fluffier material, and S-types formed at higher temperatures on the inner edge of the asteroid belt and are made of rockier material. Individual asteroids could have bulk densities as high as 8000 kg/m^3 if they have high metal content, or much

lower if they have high internal porosity as result of being a loosely bound accumulation of boulders. The bulk densities of taxonomic categories other than S-types and C-types are entirely unconstrained by actual measurements. Britt *et al.* (2003) list density measurements for one V-type, one P-type, two M-types, one F-type, and one G-type asteroids. Those are all large main-belt asteroids that may have very different internal porosities than NEAs. In the absence of more density measurements I assume that all of the "dark" taxonomic types (C,D,X) have bulk densities of 1400 kg/m^3, and that all of the "bright" types (A,O,Q,R,S,U,V) have densities of 2700 kg/m^3. At about 200 m, asteroids probably change from being gravitationally bound rubble piles to being monoliths (Pravec and Harris 2000). Since a rubble pile has more internal porosity than a monolith, asteroids smaller than 200 m may have substantially higher densities than large asteroids. Most of the results presented here concern large asteroids, and there are no density measurements for asteroids smaller than 200 m, therefore, I've assumed that the bimodal density distribution applies at all sizes.

Using that density assumption, and the fractional abundances of the taxonomic types from Table 4.7, the probability of collision can be calculated as a function of impact energy, shown for the Earth and Moon in Figure 5.3. To simplify the calculations, the curves in Figure 5.3 use the power-law distribution (straight blue line in Figure 4.23) rather than the full cumulative distribution (red curve in Figure 4.23) as was used for Figure 5.2. The large uncertainty involved in assuming a density distribution does not warrant the extra precision to be gained from using the full cumulative distribution. The flattening in the cumulative probability at the smallest energies is a result of limiting the calculations to asteroids larger than 25 m in diameter. The steep falloff in the probability at the largest energies is real, however, and results from a lack of NEAs large enough to produce more energetic impacts.

A recent report by a task force of the government of the United Kingdom of Great Britain (UK NEO Task Force 2000) focused on impacts larger than 4x10^{18} J (4 EJ) as being the most significant threat to humanity. These would be from impactor diameters of about 200 m or larger. I find that impacts of that energy strike the Earth every 47,000 ± 6,000 years. Recent estimates of this value range from once every 63,000 ± 8,000 years (Morbidelli *et al.* 2002b) to approximately once every 15,000 years (Morrison *et al.*

1994). The differences in these estimates are due almost entirely to differences in the estimates of the number of NEAs larger than 200 m.

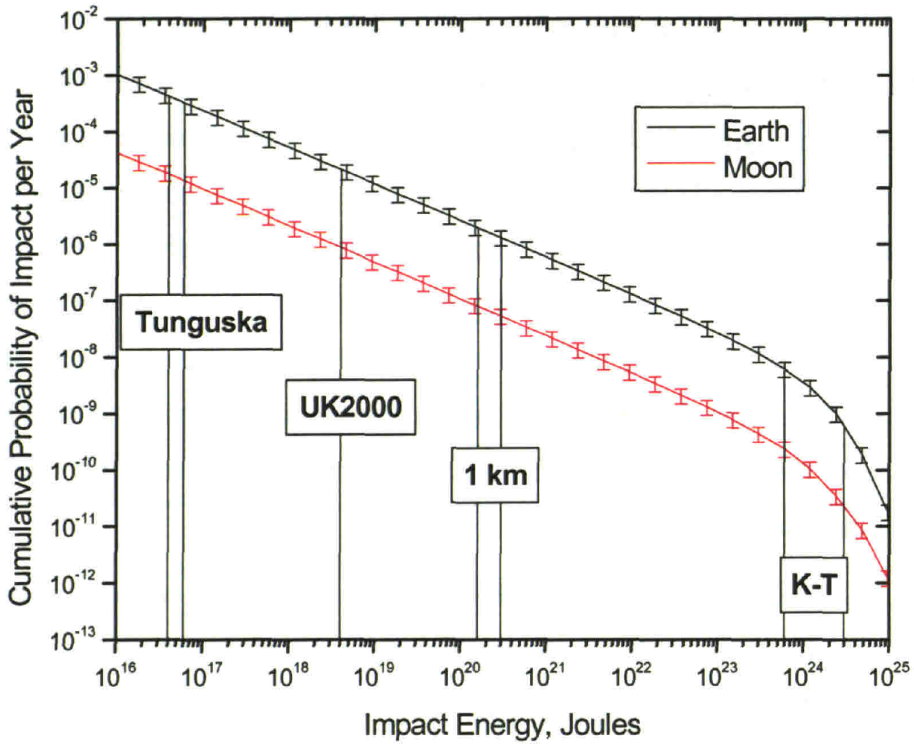

Figure 5.3 Probability of NEA Impact versus Impact Energy. The distribution of orbital elements for the NEAs (section 2.7) is combined with the debiased diameter distribution (4.10), the impact probability calculations from section 5.3, and a bimodal density distribution to obtain the cumulative probability of impact for NEAs with impact energy greater than a given energy. For comparison, 1 megaton of TNT is 4.18×10^{15} J. The diameter distribution used for this plot is the simple power-law (straight blue line in **Figure 4.23**). Vertical lines represent the energy or possible range of energies for various events. The energy from the Tunguska event is estimated as $4–8 \times 10^{16}$ J (Sekanina 1998). The UK NEO Task Force identified 4×10^{18} J as a threshold for large-scale regional destruction (UK NEO Task Force 2000). Impact by a 1 km diameter asteroid at the RMS, Earth-impact velocity of 20.9 km/s with a density of 1400 km/m^3 or 2700 km/m^3 would deliver an energy of 1.6×10^{20} J or 6×10^{20} J, respectively. The energy of the K-T impact event that formed the Chicxulub crater is estimated as $6 \times 10^{23} – 3 \times 10^{24}$J (Pope *et al.* 1997).

The Tunguska event that devastated a region of Siberian forest in 1908 is estimated to have delivered $4–6 \times 10^{16}$ J of kinetic energy with 5×10^{16} J being the most likely value (Sekanina 1998). This range of energies corresponds to an event that should happen, on average, every 2000 – 3000 years, using the impact frequencies derived here and shown in Figure 5.3. However, some researchers have suggested, based on an analysis of the Shoemaker-Levy 9 impacts into Jupiter, that the Tunguska energy could have been as low

as $1x10^{16}$ J (Boslough and Crawford 1997). If this is the correct energy for the Tunguska event, then these events could occur as frequently as every 1000 years. This estimate uses an extrapolation of the exponential fit to the number of NEAs versus absolute magnitude (Figure 2.8), and so it does not account for deviations from that simple function that might occur in the population of small NEAs. Harris (2002) and Morrison *et al.* (2002) estimated the frequency of Tunguska-type impactors as once every 1000-3000 years. That estimate assumes that the average albedo of NEAs is 0.11, somewhat darker than the value of 0.14 found in section 4.9. They also assumed a mean density of asteroids of 2500 kg/m^3, which is higher than the 2050 kg/m^3 used here (2050 kg/m^3 is an impact probability-weighted average, that is the average density when 2700 kg/m^3 for bright complexes and 1400 kg/m^3 for dark complexes are averaged after being weighted by taxonomic abundances in Table 4.7 and by impact probabilities for NEAs with $T_J<3$ or $T_J>3$). Thus, the estimate by Harris and Morrison *et al.* of the number of Tunguska-type impactors and the frequency of Tunguska-type events is higher than the estimate given here because of the different values for NEA albedo and density.

5.5 Cratering Dynamics

A great deal of work has been done by many researchers to understand the dynamics of impact cratering. This work has included observations of naturally occurring impact craters, hydrocode computer simulations of impact events, and laboratory experiments with high velocity guns and high explosives. The best review of this work is the book *Impact Cratering: A Geologic Process* by H. J. Melosh (Melosh 1988). Despite the extensive amount of work done in this area, formation of craters larger than what can be simulated in a laboratory remains poorly understood. The current state of the art is to use empirical relationships, derived from laboratory experiments, that calculate the crater diameter given the kinetic energy and density of the impactor, along with the density and gravity of the target body. These empirical relationships have been scaled up from laboratory impact experiments to the large sizes I am interested in here (kilometer-sized craters) and the results have been compared with hydrocode simulations. Additional ad-hoc relationships are used to decide when the crater formation moves from a strength-dominated regime in which the crater formation dynamics are dominated by effects derived from the material cohesiveness of the target, to the gravity regime where

the gravity of the target is the dominant force controlling crater formation. Moving to even larger sizes, additional ad-hoc rules are used to determine when simple, roughly hemispherical craters, undergo a variety of collapse mechanisms to become complex craters with collapsed walls, central uplifts, and multi-ring basins. For a review of these empirical rules, see Melosh's book, Ivanov *et al.* (2001), Grieve and Cintala (1992), Grieve and Shoemaker (1994), Shoemaker *et al.* (1990), and Holsapple (1993). Here, I am concerned only with large craters formed in rock, so only crater formation in the gravity regime on rocky surfaces will be considered.

Chapter 7 of *Impact Cratering: A Geologic Process* by H. J. Melosh gives an excellent overview of the various steps in calculating crater formation. Furthermore, a web-site run by Melosh (http://www.lpl.arizona.edu/tekton/crater.html) provides an interactive implementation of Melosh's equations, and provides Fortran code that can be downloaded. When a hypervelocity impact occurs, the excavated hole that forms seconds to minutes after the impact is referred to as the transient crater, and the diameter is customarily measured at the level of the pre-impact surface. The transient crater then undergoes collapse (even for simple, bowl-shaped craters) with some of the material from the walls slumping down into the bottom of the crater. This slumping increases the diameter of the final crater, and Melosh suggests using a factor of 1.25 to correct for this. The impact event also causes uplift around the crater so that the crater rim is above the original surface, and the rim-to-rim diameter is larger than the diameter as measured at the pre-impact surface. Melosh suggests using another factor of 1.25 to correct for this effect. Combined, the final crater diameter is 1.56 times larger than the transient crater diameter given by most crater scaling equations. All of the crater scaling equations presented below give transient crater diameter that must be multiplied by 1.56 to convert to final rim-to-rim diameter. One of the equations given below, the one from Shoemaker *et al.* 1990, did not have this factor as presented by Shoemaker *et al.*, and yet in that paper, Shoemaker *et al.* treats the results of the equation as a final rim-to-rim diameter. I have added the factor of 1.56 when using Shoemaker's equation, because otherwise it gives results quite far off from the other crater scaling equations. For large craters, additional modification occurs that increases the final crater diameter beyond the factor of 1.56. These are generally referred to as complex craters, and instead of having a

simple bowl shape, they have central uplifts, or, for very large craters, multiple uplifted rings. The diameter at which the transition from simple to complex craters occurs is not accurately known. Most authors consider that modification to complex craters occurs around 15-20 km on the Moon, with the threshold diameter scaling inversely with gravity. Melosh uses 18 km for the Moon and has the threshold scaling inversely with gravity, and inversely with the density of the target rock. Here, I use Melosh's value of 18 km for the Moon, which scales to 3 km for the Earth. For craters whose rim-to-rim diameters are above this threshold, the final diameter will be increased. Most authors suggest using the scaling equation of Croft (1985). The final crater diameter, D_f is calculated from the initial rim-to-rim diameter, D_r as

$$D_f = \frac{D_r^{1.18}}{D_*^{0.18}} \tag{5.6}$$

if D_r is larger than the threshold for transition to complex craters, D_*. Shoemaker (1990) suggests that a slightly simpler crater collapse factor of 1.3 can be applied above the threshold diameter to account for the increased diameter of complex craters. Here I use Croft's scaling rule.

Various authors use different factors to account for the effects of oblique impact. All agree that a factor of $(\sin\alpha)^\beta$ should be used, where α is the impact angle, measured such that a vertical impact has α=90°. However, authors differ on what the value of β should be. In my calculations of crater diameters in which I compare the results of different scaling equations, I've used the value of β presented by the author associated with each equation. The statistical calculations for collision probability and velocity presented above are not accurate enough to give actual impact angles, calculation of which would require extremely well defined orbital parameters for the impactor and the target. However, for a set of impacting bodies with stochastic orbits, the direction from which impacts occur should be uniformly distributed over the surface of a hemisphere. When a distribution that is uniform over a hemisphere is converted to a single impact angle, the resulting distribution of impact angles is proportional to $\sin(2\alpha)$, which has a maximum at α =45° and a goes to zero at α = 0° and at α =90°. Averaging over impact angles results in an average reduction in the crater diameter by a factor dependent upon β.

So, the factor of $(\sin\alpha)^{\beta}$ in equations (5.7), (5.8), (5.10), and(5.11), may be replaced by a factor of 0.86, 0.82, or 0.75 depending upon whether the exponent, β is 1/3, 0.43, or 2/3, respectively. This factor is slightly different from using the modal correction factors of $\sin(45^{\circ})^{\beta}$, which are 0.89, 0.86, and 0.79, respectively.

Various authors use different units (cgs, mks, megatons of TNT equivalent, kilometers) in their equations. I've converted all of the units in the following equations to the mks system to make comparison easier. The first three scaling laws presented below are all from Melosh's Fortran code and Chapter 7 of his book.

Pi Scaling. The method preferred by Melosh, and referred to as Pi-scaling, ultimately derives from the centrifuge-mounted gun experiments of Schmidt and Housen (1987):

$$D_t = 1.16\left(\frac{\rho_i}{\rho_T}\right)^{1/3} D_i^{0.78} v^{0.44} g^{-0.22} (\sin\alpha)^{1/3} \tag{5.7}$$

where D_t is the transient crater diameter, ρ_i and ρ_t are the bulk densities of the impactor and target, respectively, v is the impact velocity, and g is the acceleration due to gravity at the surface of the target body.

Yield Scaling. Melosh also gives a crater scaling equation from Nordyke, 1962. Melosh's version includes a correction for the depth to which the projectile penetrates.

$$D_t = \left(0.0133 W^{1/3.4} + 1.51\sqrt{\frac{\rho_i}{\rho_T}} D_i\right)\left(\frac{g_e}{g}\right)^{1/6} (\sin\alpha)^{1/3} \tag{5.8}$$

where g_e is the acceleration due to gravity on the Earth, and W is the kinetic energy of the impactor ($W = \frac{1}{2}mv^2$, in Joules in the mks system).

Gault Scaling. The third crater scaling formula that Melosh presents is due to Gault, 1974.

$$D_t = \Upsilon \frac{\rho_i^{1/6}}{\rho_t^{1/2}} W^{\psi} \left(\frac{g_m}{g}\right)^{1/6} (\sin\alpha)^{\zeta} \tag{5.9}$$

where $\Upsilon = 0.25, \psi = 0.29, \zeta = 2$ for transient craters smaller than 100 m in diameter, and $\Upsilon = 0.27, \psi = 0.28, \zeta = 1$ for transient craters bigger than 100 m, and g_m is the acceleration due to gravity at the surface of the Moon.

Shoemaker's Scaling Law. The crater scaling formula given in Shoemaker *et al.* 1990 is as follows:

$$D_t = 0.01436 c_r \left(W \frac{\rho_i}{\rho_t} \right)^{1/3.4} \left(\frac{g_e}{g} \right)^{1/6} (\sin\alpha)^{2/3} \tag{5.10}$$

where c_r is the crater collapse factor, given as 1.3 for crater diameters larger than 4 km on Earth, with the minimum size for complex crater collapse scaling inversely with gravity. This formulation is quite similar to Melosh's yield scaling, but without the correction for the penetration depth, and with slightly different treatment of the impactor and target densities.

Pierazzo's Scaling Law. The last equation for estimating impact crater diameter is from Pierazzo *et al.* (1997). This is quite similar to Melosh's Pi-Scaling, as it is also ultimately derived from Schmidt and Housen (1987).

$$D_t = 1.16 \left(\frac{\rho_i}{\rho_t} \right)^{1/3} D_i^{0.78} g^{-0.22} (v \sin\alpha)^{0.43} \tag{5.11}$$

Figure 5.4 and Figure 5.5 compare these scaling relations for impacts into the Earth and Moon.

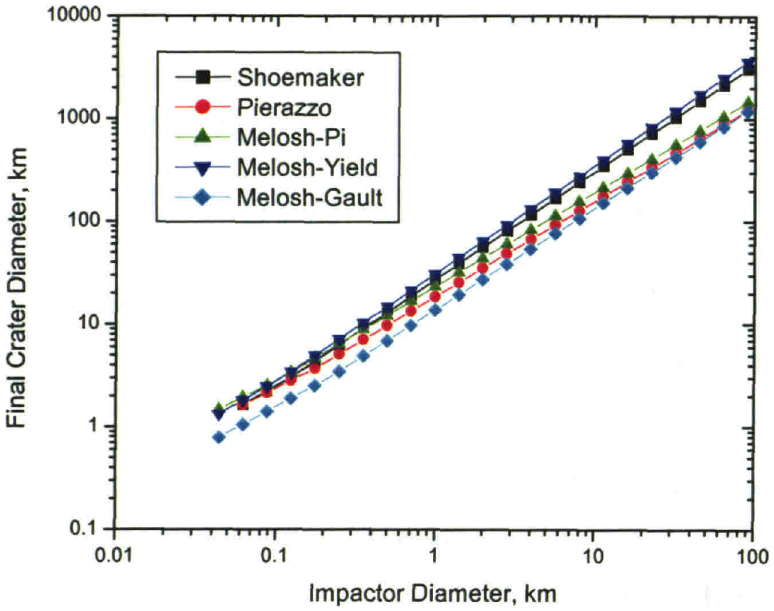

Figure 5.4 Crater Diameter versus Impactor Diameter for the Earth. The impactor is assumed to be spherical with density 2700 kg/m^3, to have final impact velocity equal to the RMS impact velocity for the Earth, 20.9 km/s, and to strike at a 45° angle. The target rock is assumed to be 2700 kg/m^3, similar to continental crust.

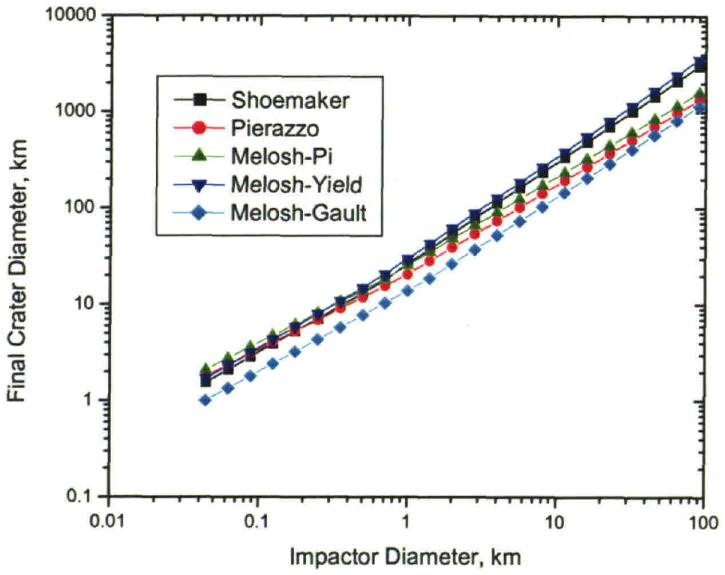

Figure 5.5 Crater Diameter versus Impact Diameter for the Moon. The impactor is assumed to be spherical with density 2700 kg/m^3, to have final impact velocity equal to the RMS impact velocity for the Earth, 19.2 km/s, and to strike at a 45° angle. The density of the target rock is assumed to be 2700 kg/m^3, which is appropriate for lunar maria.

Continuing to use the assumption given above that dark NEAs (C, D, X complexes) have bulk densities of 1400 kg/m^3 and that bright NEAs (S, Q, etc complexes) have bulk densities of 2700 kg/m^3, I can use any of the crater scaling laws to convert the impact rates that are given above as a function of impactor size into crater production rates for craters larger than a specified size, either on the Earth or on the Moon. This rate of crater production represents the current rate of crater production from NEAs. It does not include craters produced by comets. The current rate of crater production, as derived from estimates of the NEA population can be compared with the historical cratering record.

5.6 Crater Counting on the Moon

The lunar maria are a unique resource for measuring the impact environment of the Earth and Moon. The Moon has none of the atmospheric or geological processes that rapidly degrade and obliterate impact structures on the Earth. The lack of an atmosphere on the Moon allows even very small bodies to strike the surface unhindered. Furthermore, each mare is thought to have been created in a geologically quick volcanic flow (most samples are 3.2-3.5 Ga, Stöffler and Ryder 2001), and to be little changed since then, except for the effects of impacts. Thus the maria are nearly ideal surfaces that were "wiped clean" aeons ago and that have been accumulating impact craters ever since.

There are, however, several problems with interpreting the cratering record on the lunar maria.

- Even on the Moon, there are erosional processes that effect craters. The craters on the lunar maria are under constant bombardment by small impacts that tend to make the craters shallower and broader.
- Another problem for counting small craters is confusion between primary craters, generated directly by an asteroid or comet impact, and secondary craters, created by falling ejecta from a nearby, larger primary crater. Erosion from microbombardment, and confusion between primary and secondary craters preferentially affects small craters such that some authors suggest using only craters with diameters larger than about 2 km.

- At larger sizes, there are so few craters on any given mare that simple Poisson statistics yield large uncertainties. The size above which the data become too uncertain varies depending upon the size and age of the particular mare, from 11 km to 50 km.
- The maria give us a record of the impact history of the Moon that is integrated over 3 to 3.5 Gyr, resulting in two problems. First, any recent changes in the rate of crater formation will not be evident. Second, to obtain an estimate of the rate of crater formation, as opposed to observed crater density, one must know the age of the geologic province. Several of the front-side lunar maria were visited by Apollo spacecraft, and rock samples were returned to Earth. Very accurate dates are known for those rocks but it is not clear whether those returned samples, which are quite limited in collection location and depth, are truly representative of the formation age of the entire mare at a depth that is appropriate for multi-kilometer impact craters.

The most comprehensive assessment of the post-mare cratering rate is Chapter 8 of the book *Basaltic Volcanism on the Terrestrial Planets* (Hartmann *et al.* 1981, henceforth referred to as BVTP). BVTP does not explicitly give uncertainties for their estimated cratering rates but suggest that crater counts by different authors differ by about 30%. Uncertainties in the area in which craters are counted and in the ages of geological provinces would increase the uncertainty in the crater rate to more than 30%. A recent analysis by Stöffler and Ryder (2001), indicates that the ages used in BVTP for the maria are too old by about 4% on average. This correction would increase the BVTP cratering rate by 4% at all crater diameters. This correction has not been applied here in comparing the BVTP crater production function with the NEA population. The BVTP crater production function used for comparison here has been taken directly from Table 8.4.1 of BVTP. The cumulative crater density of the average of lunar frontside mare is divided by the average age of the returned lunar mare samples, 3.45 Gyr.

Recent presentations of the lunar cratering rate by Neukum, Ivanov, and coauthors (Ivanov *et al.* 2001, Werner *et al.* 2002, Neukum and Ivanov 1994) include the craters on the older lunar highlands. The lunar highlands formed before the end of the period of Late Heavy Bombardment, and Neukum/Ivanov crater production function is dominated by impacts from that period (C. Chapman, personal communication). Since there is little

reason to believe that the impactor flux is currently the same as during the period of Late Heavy Bombardment, I prefer to use the post-mare lunar cratering rate as presented in BVTP to compare against the current cratering rate. I also compare the lunar crater production function based on the NEA population model to the highlands production function of Neukum and Ivanov.

5.7 Comparison with the Lunar Crater Record

Figure 5.6 shows the BVTP crater production function for the average of front-side lunar maria, and the highlands crater production function of Neukum and Ivanov compared with the current cratering rate as predicted by my population model and various crater scaling laws. The predicted crater production function from the NEA population model is quite similar to the function derived by counting craters on the lunar maria. This is consistent with the NEA population being in steady-state, and with the rate of lunar crater production being constant for the last 3 Gyr. It also agrees with other recent analyses of the rate of comet impacts and suggests that comet impacts are a minor contributor to the total impactor flux (Weissman *et al.* 2002). The crater production function of Neukum and Ivanov matches the crater production function derived from the NEA population for crater diameters larger than 10 km. However, there is a significant mismatch in the range of 1 to 10 km. The largest difference is that the Neukum/Ivanov production function is a factor of 7 lower than the NEA production function at crater diameters of 2.8 km.

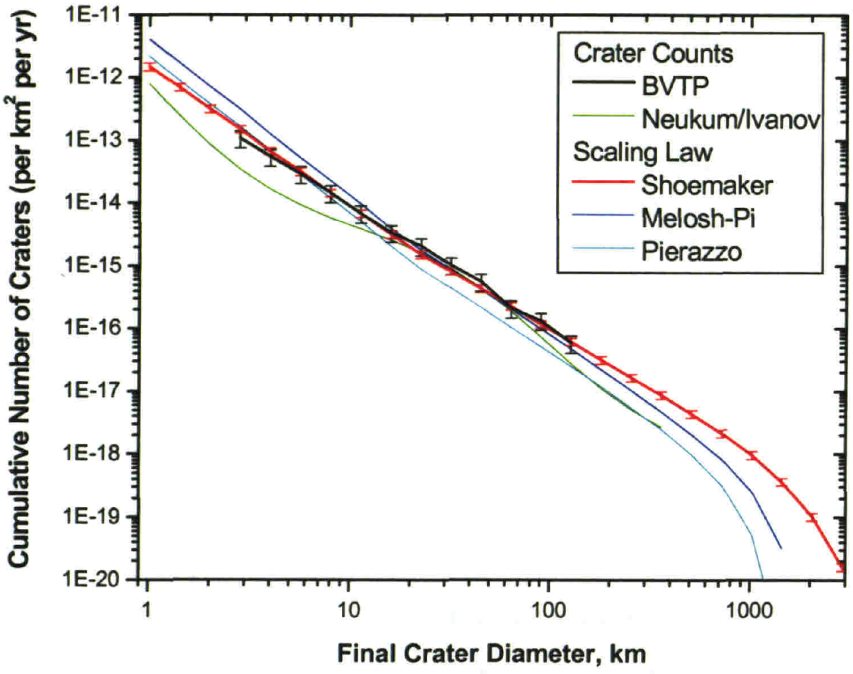

Figure 5.6 Lunar Cratering Rate. The rate of formation of craters on the lunar maria (taken from BVTP) is compared with the expected rate of crater formation from the NEA population models presented here. The three curves showing the NEA model results use different crater scaling laws to derive crater diameters, but all use the same NEA population model from section 2.7. The crater scaling law by Shoemaker [equation **(5.10)**]gives the best match to the BVTP production function. The uncertainties shown for the preferred model, Shoemaker scaling, are calculated by increasing or decreasing the number of NEAs in the population model by 1σ (or 180 NEAs at 1 km). These uncertainties do not include uncertainties in densities or crater scaling laws. The overall rate of lunar crater formation as derived from the NEA population model, with the Shoemaker scaling law, matches the rate predicted by counting craters on the lunar maria (BVTP) over crater diameters from 2 km to over 100 km. The lunar crater production function from Neukum and Ivanov is also shown for comparison (Ivanov *et al.* 2001). This matches quite well with the NEA production function (Shoemaker scaling) from diameters of about 20 km to 60 km. However, outside that range, there is a severe mismatch with the highlands crater production function being a factor of 4 or more lower than the production function based on the NEA population model.

The number of craters on the Moon matches the expected rate of crater formation from the NEA population model (Figure 5.6) with both the Melosh-Pi scaling law [equation (5.7)], and the Shoemaker scaling law [equation (5.10)]. However, the Shoemaker formula produces a closer match. A linear least-squares fit to the logarithm of the BVTP cratering record, assuming 30% uncertainties for the BVTP crater counts, produces a logarithmic slope of –1.95±0.07. Melosh's Pi-Scaling formula produces a distribution of crater diameters with a slope of -2.34±0.08. Assuming simple Gaussian statistics for these slopes, -2.34±0.08 is 3.5σ away from the BVTP slope of -1.95±0.07.

Thus the crater size distribution derived from the NEA population and Melosh's Pi-Scaling formula is significantly steeper than the crater size distribution found in the BVTP. The formula from Shoemaker produces a crater diameter distribution with a slope of -2.08 ± 0.07. This result is 1.2σ away from the BVTP slope, and is therefore statistically consistent with the slope of the BVTP crater size distribution. The NEA population model derived here, combined with the Shoemaker crater scaling formula produces a good match to the BVTP crater production function.

Werner *et al.* (2002) performed a similar comparison between the Neukum/Ivanov lunar crater production function, and the NEA population estimates of D'Abramo *et al.* (2001) and Rabinowitz *et al.* (2000). They performed the calculations in the opposite direction, converting the lunar crater production function into a impactor size-frequency distribution. This approach has the disadvantage that it must use an average impact velocity and impactor density. It cannot use a distribution of impact velocities or a distribution of impactor densities, as was done here, because there is no way to estimate those quantities from an observed crater. Werner *et al.* found reasonably good agreement between the Neukum/Ivanov crater production function and the NEA population estimates of D'Abramo *et al.* and Rabinowitz *et al.* As discussed in section 2.8, those two NEA population estimates are lower than the NEA population estimate derived in section 2.7. The Neukum/Ivanov crater production function is also lower than the BVTP crater production function for crater diameters from ~3 km to ~15 km.

5.8 Comparison with the Terrestrial Crater Record

Geologic processes of erosion and plate subduction make calculations of cratering rates on the Earth much more problematic than on the Moon. Small craters on the Earth are erased quickly, very little of the Earth's crust is old enough to have accumulated enough large craters to count, and much of the Earth is covered by oceans in which permanent craters do not form at all. However, the craters that are observed on the Earth are available for close scrutiny. Accurate ages can be obtained for each crater, and the crater rim and floor can be studied to characterize slumping and formation of complex crater features such as central uplifts. The cratering record on the Earth has been studied extensively in the last few decades, especially since the Cretaceous-Tertiary extinction

event was linked with an impact (Alvarez *et al.* 1980). Figure 5.7 shows the rate of production of impact craters on the Earth (Hughes 2001) as determined by counting and dating impact structures, compared to the rate predicted from the NEA population. I have used Melosh's Pi-Scaling method to calculate the size of the impact craters, and I've assumed a density of 2700 kg/m^3 for terrestrial target rocks. As with the lunar crater production predictions, the sharp turnover in the predicted number of large craters on the Earth is because of a lack of NEAs large enough to produce such large craters. On the Earth, however, the reduction in the number of very small craters, less than about 1 km diameter, is probably real. The simulation included NEAs down to 50 m in diameter. At sizes below 50 m, the atmosphere shields the surface of the Earth from impact.

Above crater sizes of about 15 km, the observed cratering rate on the Earth matches the rate predicted from the NEA population models. Below 10 km, there is a pronounced deficit of observed craters. Most researchers (Grieve and Shoemaker 1994, for example) attribute the deficit of small craters to erosion that erases them from the crater record, and assume that, in the absence of erosion, the production rate of craters should continue upward roughly as a power law. Hughes (2001), however, argues that the deficit of small craters is a real feature of the rate of production of craters, and not due to some size-dependent erosional process. It is impossible to reconcile that view with observational data of NEAs. A deficit of craters in the 10 km range would require a sharp deviation from a power law in the number NEAs starting at sizes around 1 km. This marked reduction in the number of 1 km NEAs is not observed. It is also impossible to reconcile this deficit of craters smaller than 10 km with the cratering record on the Moon which matches the observed population of NEAs down to crater sizes of 2 km.

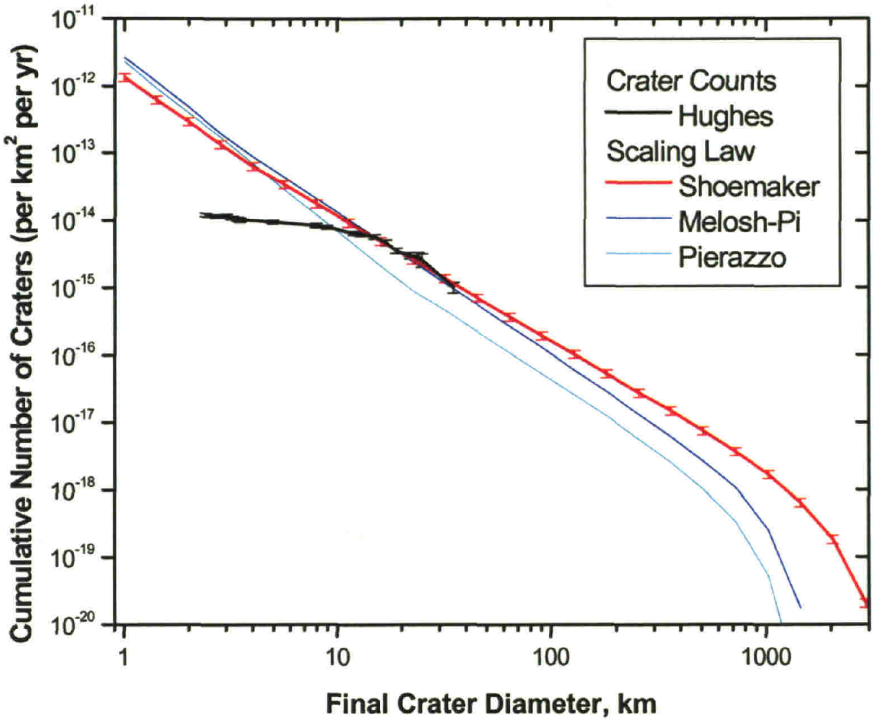

Figure 5.7 Terrestrial Cratering Rate. The rate of production of craters on the Earth as catalogued by Hughes (2001) is compared with the expected rate of crater formation from the impact of NEAs. The NEA population model from section 2.7 is combined with three crater scaling laws to estimate the current crater production function on the Earth. The preferred scaling law [Shoemaker, equation **(5.10)**] is shown with uncertainties computed by changing the number of NEAs in the population model by 1 standard deviation, and do not include uncertainties in NEA density or crater scaling laws. The NEA population model combined with either the Shoemaker or Melosh-Pi scaling laws [equation **(5.7)**] matches the crater production function determined from counting craters on the Earth in the size range from 15 km to 35 km. Below 15 km, craters on the Earth are eroded by weather and so the counts of small craters are severely depleted.

5.9 Conclusions

The model of the NEA population developed in Chapter 2 and Chapter 4 has been used to predict the rate of impacts of NEAs into the Earth and Moon. The Earth suffers globally catastrophic NEA impacts (larger than 1 km diameter impactor) every 500,000 to 700,000 years, and regionally devastating impacts (4 EJ or more of impact energy) every 41,000 to 53,000 years. Impacts with energies near that of the Tunguska impactor occur every 2000 to 3000 years. The rate of crater formation on the Earth and Moon, as predicted by the NEA population model combined with a simple NEA density

assumption, impact probability estimates, and crater scaling laws, is consistent with the observed number of craters on the Earth and Moon.

The observed terrestrial cratering rate matches the current cratering rate from NEAs. The observed cratering rate on the lunar maria also matches the current cratering rate from NEAs. Therefore, the terrestrial cratering rate matches the lunar cratering rate. The terrestrial cratering rate shown in Figure 5.7 is for recent geological time, approximately 125 Myr (Hughes 2001). The cratering rate from the lunar maria extends over 3 Gyr (BVTP). This suggests that the 3 Gyr cratering rate from the lunar maria is from a similar NEA population to the population that produced the terrestrial cratering rate. This is consistent with the idea that the NEA population has been in steady-state since the end of the Late Heavy Bombardment 3 Gyr ago. It is inconsistent with evidence that the cratering rate has increased in the last ~100 Myr (Grieve and Shoemaker 1994, Culler *et al.* 2000).

Chapter 6 Conclusions and Future Work

6.1 Conclusions

There are 1227^{+170}_{-90} NEAs with absolute magnitudes brighter than 18.

The primary result of Chapter 2 is an estimate of the number of NEAs as a function of absolute magnitude (section 2.7). The NEAs are best fit by a cumulative distribution of $N(<H)=10^{-3.88+0.39H}$ (Figure 2.8). This estimate means that the current catalog of NEAs (as of 18 April 2003) is 50% complete for $H<18$.

The NEAs are more highly inclined than previously thought.

The debiasing of the LINEAR NEA detections presented in Chapter 2 shows that even a wide area survey is significantly biased against NEAs with high inclinations. In addition to the easily observed peak at ~5°, the debiasing shows that the inclination distribution of the NEAs has a second, large peak near 25° (Figure 2.9). This may be a signature of NEAs that originated in the Hungaria and Phocaea regions of the inner main belt, where asteroids have inclinations of 20°-30°. The NEA inclination distribution also has broader tail than expected, with an unexpectedly large number of NEAs with inclinations up to 50°.

Phase darkening is not a significant factor in bias corrections of ground-based discovery surveys of NEAs.

As shown in Chapter 1, the effect of differential phase darkening is real for NEAs and increases the selection bias against lower albedo NEAs because lower albedo NEAs tend to have lower values for the phase slope parameter, G, than do NEAs with higher albedos. However, the size of the selection bias due only to differential phase darkening is smaller than the uncertainties in the albedos of the NEAs, and is smaller than the amount of

bias caused by the completeness level of a survey (section 3.4). Most current analyses of selection bias in NEA surveys use Monte-Carlo simulations in which it is simple to include the effects of phase darkening. The lack of measured values of G for most NEAs should not be problematic in statistical models of the NEA population because the effect of changes in G is minor.

The taxonomic complexes S, Q, C, X, and D account for almost all of the NEAs.

Chapter 4 corrects for observational bias relating to differences in albedo, and finds that these five classes include ~97% of the NEAs in a diameter-limited sample. The C-types are the smallest of the five classes with ~10% of NEAs. The Q-types account for 14%, and the D-types for 18%. The two largest classes are the S- and X-types with 22% and 34%, respectively. (Figure 4.22 and Table 4.7)

The NEAs with $T_J<3$ differ in their taxonomic abundances from the NEAs with $T_J>3$.

The NEAs with $T_J<3$ have a significantly higher proportion of their members in the D- and X-type taxonomic complex than NEAs with $T_J>3$ (section 4.9). This result combines dynamics and taxonomy into a consistent picture. The NEAs that are dynamically linked to Jupiter ($T_J<3$) are more enriched in possible extinct comets (D-types) than are the NEAs that are not dynamically linked to Jupiter ($T_J>3$).

After accounting for observational biases, in a diameter-limited sample, the NEAs with $T_J<3$ account for 30% of the total NEA population.

The average albedo of the NEAs is 0.140±0.02.

When the albedos of the taxonomic complexes are weighted according to their relative abundances, the overall average albedo of the NEAs is slightly brighter than the generally assumed value of 0.11. This means that the average absolute magnitude threshold for 1 km or bigger asteroids is $H<17.75\pm0.1$ (section 4.9). Separating the NEAs into two groups according to the Jovian Tissearnd parameter, I find that the NEAs with $T_J<3$ have an average albedo of 0.084 ± 0.01, while the NEAs with $T_J>3$ have an average albedo of 0.164 ± 0.06.

There are 1090±180 NEAs bigger than 1 km diameter.

The primary result from this thesis, given in section 4.10, is the debiased diameter distribution of the NEAs. The absolute magnitude distribution (Figure 2.7) is converted to several diameter distributions using the albedos and abundances of the taxonomic complexes. The diameter distributions for the complexes are summed to obtain the overall diameter distribution for the NEAs (Figure 4.23).

As of 18 April 2003, 543 NEAs have been discovered with $H<17.75$. Using the result that this corresponds to a diameter of 1 km, 50% of the 1 km NEAs have been discovered.

Impacts of NEAs larger than 1 km occur every 500,000 to 700,000 years on the Earth.

The orbital element distribution from section 2.7 is combined with the diameter distribution from section 4.10, along with estimates of collision probability for NEAs (section 5.3) to derive the rate of impact of NEAs into the Earth (Figure 5.2). Impacts of this size are believed to have global consequences by filling the atmosphere with enough dust to affect climate worldwide.

Impacts larger than $4x10^{18}$ J occur every 41,000 to 53,000 years on the Earth.

The impact rate of NEAs into the Earth is combined with an assumption about the densities of asteroids to obtain rates of impact as a function of impact energy (Figure 5.3). Impacts larger than $4x10^{18}$J are likely to produce widespread regional destruction (UK NEO Task Force 2000).

Impacts in the energy range of the Tunguska event occur every 2,000 to 3,000 years on the Earth.

The impact rate of NEAs into the Earth is combined with an assumption about the densities of asteroids to obtain rates of impact as a function of impact energy (Figure 5.3). Impacts in the energy range of the Tunguska event ($4\text{-}6x10^{16}$ J) occur every 2,000 to 3,000 years. This rate could be as high as every 1000 years if the Tunguska event was only $1x10^{16}$ J.

The current rate of crater production on the Moon matches the 3 Gyr post-mare crater record.

The NEA orbital element distribution (section 2.7), and the diameter distribution (section 4.10) has been used, along with several methods for determining crater diameter, to determine the rate of formation of craters on the Moon (section 5.5). The rate of crater formation, based on the NEA population derived here, matches the observed lunar cratering rate for craters from 2 to 100 km diameter (Figure 5.6).

The current rate of crater production on the Earth matches the 125 Myr crater record on the Earth.

The NEA orbital element distribution (section 2.7), and the diameter distribution (section 4.10) has been used, along with several methods for determining crater diameter, to determine the rate of formation of craters on the Earth (section 5.5). The rate of crater formation, based on the NEA

population model derived here, matches the observed terrestrial cratering rate over the range of crater sizes that is not severely affected by erosion (craters larger than 15 km) (Figure 5.7).

The cratering rate on the Earth and Moon have been constant for 3 Gyr.

The crater density observed on the lunar mare is the cratering rate integrated over the 3 Gyr since the mare formed. That rate matches the current cratering rate from NEAs. This match is consistent with the cratering rate being constant for 3 Gyr, and with the NEAs being in a steady-state for that time. (section 5.9)

Comets do not make a significant contribution to the impact rate on the Earth and Moon.

The lunar crater density is consistent with the cratering rate expected from the NEAs (Figure 5.6). There is no large excess of craters on the Moon that could be caused by long-period comets.

6.2 Future Work

LINEAR (and other asteroid search programs) continue to scour the skies and detect more asteroids. These continuing data can be incorporated into the NEA population estimates to improve estimates of the size and shape of the NEA population. In addition to improving the accuracy of the estimate, more data should allow an estimate at dimmer absolute magnitudes (smaller sizes) and at higher inclinations. Improvement can also be made in the photometric calibration of the LINEAR sensor. A better understanding of LINEAR's limiting magnitude, how it is affected by weather, stellar background, seasons, equipment changes, and asteroid colors will improve the accuracy of the population estimate.

The LINEAR program also detects and catalogs a large number of main-belt asteroids. A debiased estimate of the number of main-belt asteroids based on LINEAR data would be a useful addition to our understanding of the main belt. It would also be

useful to combine this new estimate of the number of main-belt asteroids with estimates of the number of Mars crossers and NEAs. A consistent picture of these three groups, could provide better understanding of the dynamical processes that transport asteroids around the inner solar system, and would help to determine which of the main belt resonance zones are the most important suppliers of NEAs.

Estimates of the fractional abundances of the various taxonomic classes would be improved by more albedo measurements of NEAs. More measured albedos will also improve the conversion of the absolute magnitude distribution to a diameter distribution. Two of the taxonomic classes are of particular concern. The albedos of the X-type NEAs can vary over a wide range, resulting in a large uncertainty in their average albedo and fractional abundance. More albedo measurements of X-type NEAs would help to define how many of the X-types are very dark and how many are relatively bright, thus reducing the uncertainty in the fractional abundance of the X-types. The D-type NEAs, particularly those with Jovian Tisserand parameter less than three, are potentially very dark objects. More albedo measurements for the D-type NEAs will help to determine whether this class contributes many additional large NEAs to the total population.

The slight mismatches between the expected lunar cratering rate from NEAs and the observed crater counts suggests that the dynamics governing the formation of large craters is not perfectly understood. An experiment to observe the formation of a large crater is needed to refine the scaling laws and to calibrate hydrocode simulations. Several NEAs measuring in size from tens of meters to hundreds of meters should be intensively studied by orbiting spacecraft (similar to the NEAR-Shoemaker mission) and then diverted into trajectories that impact the Moon. The geology of the impact sites should be carefully studied beforehand, as well. During the impact, a suite of sensors on the Moon and above the impact sites would yield invaluable real-time information to refine models of impact crater formation. Post-impact analysis of the geological changes produced by the impact would further enhance our knowledge of impact dynamics. Of course, care must be taken to avoid mishap and misuse of asteroid deflection technologies (Harris *et al.* 1994).

References

(Alvarez *et al.* 1980)
Alvarez, L.W.; Alvarez, W.; Asaro, F.; Michel, H.V. Extraterrestrial Cause for the Cretaceous Tertiary Extinction. *Science* 208, p.1095. 1980.

(Barucci *et al.* 1987)
Barucci, M.A.; Capria, M.T.; Coradini, A.; Fulchignoni, M. Classification of asteroids using G-mode analysis. *Icarus* **72**, p.304-324. Nov 1987.

(Bauluz *et al.* 2000)
Bauluz, B.; Peacor, D.R.; Elliott, W.C. Coexisting altered glass and Fe-Ni oxides at the Cretaceous-Tertiary boundary, Stevns Klint (Denmark): direct evidence of meteorite impact. *Earth and Planetary Science Letters* **182-2**, p.127-136. 2000.

(Benner *et al.* 2001)
Benner, L.A.M.; Ostro, S.J.; Nolan, M.C.; Margot, J.-L.; Giorgini, J.D.; Hudson, R.S.; Jurgens, R.F.; Slade, M.A.; Campbell, D.B.; Yeomans, D.K. Radar Observations of Asteroid 1999 JM8. American Astronomical Society, DPS meeting #33, #61.06. 2001.

Bessell, M.S. UBVRI passbands. *Publications of the Astronomical Society of the Pacific* **102**, p.1181-1199. 1990.

(Bevington 1969)
Bevington, P.R.; Data Reduction and Error Analysis for the Physical Sciences. McGraw-Hill Book Company, New York, NY. 1969.

(Binzel *et al* 1992)
Binzel, R.P.; Xu, S.; Bus, S.J.; Bowell, E. Origins for the near-earth asteroids. *Science* **257-5071**, p. 779-782. 7 Aug 1992.

(Binzel and Xu 1993)
Binzel, R. P., Xu, S. Chips off of asteroid 4 Vesta - Evidence for the parent body of basaltic achondrite meteorites. *Science* **260-5105**, p.186-191. 1993.

(Binzel *et al.* 1996)
Binzel, R.P.; Bus, S.J.; Burbine, T.H.; Sunshine, J.M. Spectral Properties of Near-Earth Asteroids: Evidence for Sources of Ordinary Chondrite Meteorites. *Science* **273-5277**, p.946-948. 1996

(Binzel 2000)
Binzel, R. P. The Torino Impact Hazard Scale. *Planetary and Space Science* **48-4**, p. 297-303. 2000.

(Binzel *et al.* 2002a)
Binzel, R.P.; Lupishko, D.F.; Di Martino, M.; Whiteley, R.J.; and Hahn, G.J. Physical Properties of Near-Earth Objects. in Asteroids III (W.F. Bottke, A. Cellino, P. Paolicchi, R.P. Binzel, eds.). The University of Arizona Press, Tucson. 2002.

(Binzel *et al.* 2002b)
Binzel, R.P.; Rivkin, A.S.; Bus, S.J.; Delbo, M.; Harris, A.W.; Harris, A.W. Spectral and Albedo Properties of the Near-Earth Object Population. In Proceedings of Asteroids, Comets, Meteors 2002, ESA Special Publications Series, Berlin. July 2002.

(Bobrovnikoff 1929)
Bobrovnikoff, N. T. The spectra of minor planets. *Lick Observatory bulletin* **407**, p.18-27. University of California Press. 1929.

(Boslough and Crawford 1997)
Boslough, M.B.E.; Crawford, D.A. Shoemaker-Levy 9 and Plume-forming Collisions on Earth. *Annals of the New York Academy of Sciences* **822**, p.236-282. 30 May 1997.

(Bottke and Greenberg 1993)
Bottke, W. F.; Greenberg, R. Asteroidal collision probabilities. *Geophysical Research Letters* **20-10**, p.879-881. 1993.

(Bottke *et al.* 1994)
Bottke, W.F.; Nolan, M.C.; Greenberg, R.; Kolvoord, R.A. Collisional Lifetimes and Impact Statistics of Near-Earth Asteroids. In Hazards Due to Comets and Asteroids, (T. Gehrels, Ed.), The University of Arizona Press, Tucson, p. 337-357. 1994.

(Bottke *et al.* 2000)
Bottke, W. F.; Jedicke, R.; Morbidelli, A.; Petit, J.; Gladman, B. Understanding the Distribution of Near-Earth Asteroids. *Science* **288**, p.2190-2194. 23 Jun 2000.

(Bottke *et al.* 2002)
Bottke, W.F.; Morbidelli, A.; Jedicke, R.; Petit, J.; Levison, H.F.; Michel, P.; Metcalfe, T. S. Debiased Orbital and Absolute Magnitude Distribution of the Near-Earth Objects. *Icarus* **156-2**, p.399-433. 2002.

(Bowell *et al.* 1989)
Bowell, E.; Hapke, B.; Domingue, D.; Lumme, K.; Peltoniemi, J.; Harris, A. Application of Photometric Models to Asteroids (Appendix: The IAU Two-Parameter Magnitude System for Asteroids). In Asteroids II (R.P. Binzel, T. Gehrels, M. Matthews, Eds.), The University of Arizona Press, p.549–556. 1989.

(Britt *et al.* 2003)
Britt, D.T.; Yeomans, D.; Housen, K.; Consolmagno, G. Asteroid Density, Porosity, and Structure. In Asteroids III (W. F. Bottke, A. Cellino, P. Paolicchi, R. P. Binzel, Eds.), University of Arizona Press, Tucson. 2002.

References

(Brown *et al.* 2002)
Brown, P.; Spalding, R.E.; ReVelle, D.O.; Tagliaferri, E.; Worden, S.P. The flux of small near-Earth objects colliding with the Earth. *Nature* **420-6913**, p.294-296. 2002.

(Burbine 2000)
Burbine, T.H. Forging asteroid-meteorite relationships through reflectance spectroscopy. Ph.D. Thesis, Massachusetts Institute of Technology. 2000.

(Burbine *et al.* 2001)
Burbine, T.H., Buchanan, P.C., Binzel, R.P., Bus, S.J., Hiroi, T., Hinrichs, J.L., Meibom, A., McCoy, T.J. Vesta, Vestoids, and the howardite, eucrite, diogenite group: Relationships and the origin of spectral differences. *Meteoritics and Planetary Science* **36**, p.761. 2001

(Bus 1999)
Bus, S.J. Compositional Structure in the Asteroid Belt: Results of a Spectroscopic Survey. PhD. Thesis. Massachusetts Institute of Technology. 1999.

(Bus and Binzel 2002a)
Bus, S.J.; Binzel, R.P. Phase II of the Small Main-Belt Asteroid Spectroscopic Survey: The Observations. *Icarus* **158-1**, p.106-145. 2002.

(Bus and Binzel 2002b)
Bus, Schelte J.; Binzel, Richard P. Phase II of the Small Main-Belt Asteroid Spectroscopic Survey: A Feature-Based Taxonomy. *Icarus* **158-1**, p.146-177. 2002.

(BVTP)
Hartmann, W.K.; Strom, R.G.; Grieve, R.A.F.; Weidenschilling, S.J.; Diaz, J.; Blasius, K.R.; Chapman, C.R.; Woronov, A.; Shoemaker, E.M.; Dence, M.R.; Jones, K.L. Chapter 8: Chronology of planetary volcanism by comparative studies of planetary cratering. In Basaltic Volcanism on the Terrestrial Planets, (Basaltic Volcanism Study Project.) Pergamon Press, Inc, New York. 1981.

(Chapman *et al.* 1971)
Chapman, C.R.; Johnson, T.V.; McCord, T.B. A Review of Spectrophotometric Studies of Asteroids. In Physical Studies of Minor Planets, (T. Gehrels, Ed.), NASA SP-267, p.51-65. 1971.

(Chapman *et al.* 1975)
Chapman, C. R.; Morrison, D.; Zellner, B. Surface properties of asteroids - A synthesis of polarimetry, radiometry, and spectrophotometry. *Icarus* **25**, p.104-130. 1975.

(Croft 1985)
Croft, S.K. The scaling of complex craters. Proceedings of 15th Lunar and Planetary Sciences Conference. *Journal of Geophysical Research* **90**, p.C828-842. 1985

(Culler *et al.* 2000)
Culler, T.S.; Becker, T.A.; Muller, R.A.; Renne, P.R. Lunar Impact History from 40Ar/39Ar Dating of Glass Spherules. *Science* **287-5459**, p.1785-1788. 2000.

(D'Abramo *et al.* 2001)
D'Abramo, G.; Harris, A.W.; Boattini, A.; Werner, S.C.; Harris, A.W.; Valsecchi, G.B. NOTE: A Simple Probabilistic Model to Estimate the Population of near-Earth Asteorids. *Icarus* **153**, p.214-217. 2001

(Delbo *et al.* 2003)
Delbo, M.; Harris, A.W.; Binzel, R.P.; Pravec, P.; Davies, J.K. Keck Observations of Near-Earth Asteroids in the Thermal Infrared. *Icarus*, in preparation.

(Farinella and Davis 1992)
Farinella, P.; Davis, D.R. Collision rates and impact velocities in the Main Asteroid Belt. *Icarus* **97-1**, p. 111-123. 1992.

(Fernández *et al.* 2001)
Fernández, Y.R.; Jewitt, D.C.; Sheppard, S.S. Low albedos among extinct comet candidates. *The Astrophysical Journal,* **553**, p.L197-L200. 1 June 2001.

(Fowler and Chillemi 1992)
Fowler, J.W.; Chillemi, J.R. IRAS Asteroid Data Processing. In The IRAS Minor Planet Survey, Tech. Rep. PL-TR-92-2049, Phillips Laboratory, Hanscom Air Force Base, Massachusetts, p.17-43. 1992

(Frankel 1999)
Frankel, C. The End of the Dinosaurs : Chicxulub Crater and Mass Extinctions. Cambridge University Press, Cambridge, England. 1999.

(Gault 1974)
Gault, D. E. Impact cratering. In A Primer in Lunar Geology (N75-13730 04-91), p.137-175. 1974.

(Gladman *et al.* 2000)
Gladman, B.; Michel, P.; Froeschlé, C. The Near-Earth Object Population. *Icarus* **146-1**, p.176-189. 2000.

(Gradie and Tedesco 1982)
Gradie, J.C.; Tedesco E.F.. Compositional Structure of the Asteroid Belt. *Science* **216-4553**, p.1405-1407. 25 Jun 1982.

(Gradie *et al.* 1989)
Gradie, Jonathan C.; Chapman, Clark R.; Tedesco, Edward F. Distribution of taxonomic classes and the compositional structure of the asteroid belt. In Asteroids II (R.P. Binzel, T. Gehrels, M. Matthews, Eds.), The University of Arizona Press, p.316-335. 1989.

(Greenberg 1982)
Greenberg, R. Orbital interactions - A new geometrical formalism. *Astronomical Journal* **87**, p.184-195. Jan 1982.

(Grieve and Cintala 1992)
Grieve, R.A.F.; Cintala, M.J. An analysis of differential impact melt-crater scaling and implications for the terrestrial impact record. *Meteoritics* **27-5**, p.526-538. 1992.
(Grieve and Shoemaker 1994)
Grieve, R.A.F.; Shoemaker, E.M. The Record of Past Impacts on Earth. In Hazards Due to Comets and Asteroids, (T. Gehrels, Ed.), The University of Arizona Press, Tucson, p.417-462. 1994.

(Halliday 1996)
Halliday, I.; Griffin, A.A.; Blackwell, A.T. Detailed data for 259 fireballs from the Canadian camera network and inferences concerning the influx of large meteoroids. *Meteoritics and Planetary Science* **31**, p.185-217. 1996.

(Harris *et al.* 1994)
Harris A.W.; Canavan G.H.; Sagan C.; Ostro S.J. The deflection dilemma: Use versus misuse of technologies for avoiding interplanetary collision hazards. In Hazards Due to Comets and Asteroids, (T. Gehrels, Ed.), The University of Arizona Press, Tucson, p. 1145-1156. 1994.

(Harris 1998)
Harris, A.W. A Thermal Model for Near-Earth Asteroids. *Icarus* **131**, p.291-301. 1998.

(Harris 2001)
Harris, A.W. Near-Earth Asteroid surveys. In Collisional processes in the solar system, (Y.M. Mikhail, H. Rickman, Eds.), Astrophysics and space science library, Volume 261, Dordrecht: Kluwer Academic Publishers, p.323-332. 2001.

(Harris 2002)
Harris, A. W. A New Estimate of the Population of Small NEAs. American Astronomical Society, DPS meeting #34, #02.02. 2002.

(Harris and Harris 1997)
Harris, A.W.; Harris, A.W. On the Revision of Radiometric Albedos and Diameters of Asteroids. *Icarus* **126**, p.450-454. 1997.

(Harris and Bailey 1998)
Harris, N. W.; Bailey, M. E. Dynamical evolution of cometary asteroids. *Monthly Notices of the Royal Astronomical Society* **297-4**, p.1227-1236. 1998.

(Harris and Davies 1999)
Harris, A.W.; Davies, J.K. Physical Characteristics of Near-Earth Asteroids from Thermal Infrared Spectrophotometry. *Icarus* **142**, p464-475, 1999.

(Harris and Lagerros 2002)
Harris, A.W.; Lagerros, J.S.V. Asteroids in the Thermal Infrared. In Asteroids III (W.F. Bottke, A. Cellino, P. Paolicchi, R.P. Binzel, eds.). The University of Arizona Press, Tucson. 2002.

(Helin and Shoemaker 1979)
Helin, E.F.; Shoemaker, E.M. The Palomar planet-crossing asteroid survey, 1973-1978; *Icarus* **40**, p.321-328, 1979.

(Hicks *et al.* 2000)
Hicks, M. D.; Buratti, B. J.; Newburn, R. L.; Rabinowitz, D. L. Physical Observations of 1996 PW and 1997 SE5: Extinct Comets or D-Type Asteroids? *Icarus* **143**. p.354-359. 2000.

(Holsapple 1993)
Holsapple, K.A. The scaling of impact processes in planetary sciences. *Annual review of earth and planetary sciences* **21**, p.333-373. 1993.

(Howell *et al.* 1994)
Howell, E. S.; Merenyi, E.; Lebofsky, L. A. Classification of asteroid spectra using a neural network. *Journal of Geophysical Research* **99-E5**, p.10,847. 1994.

(Hughes 2001)
Hughes, D.W. A new approach to the calculation of the cratering rate of the Earth over the last 125+/-20Myr. *Monthly Notices of the Royal Astronomical Society* **317-2**, p.429-437. 2001.

(Hughes 2003)
Hughes, D.W. The approximate ratios between the diameters of terrestrial impact craters and the causative incident asteroids. *Monthly Notice of the Royal Astronomical Society* **338-4**, p.999-1003. 2003.

(Ivanov *et al.* 2001)
Ivanov, B.A.; Neukum, G.; Wagner, R.; Size-Frequency Distributions of Planetary Impact Craters and Asteroids. In Collisional Processes in the Solar System, (M.Y. Marov, H. Rickman, Eds.), Kluwer, Dordrecht, p.1-34. 2001.

(Kirkwood 1876)
Kirkwood, D. On the distribution of the asteroids. Salem, Massachusetts, Printed at the Salem press, 1876.

(Kresák 1979)
Kresák, L. Dynamical Interrelations among Comets and Asteroids. In Asteroids (T. Gehrels, ed.). The University of Arizona Press, p.289-309. 1979.

References

(Kuiper 1958)
Kuiper, G.P.; Fugita, Y.; Gehrels, T.; Groeneveld, I.; Kent, J.; van Biesbroeck, G.; van Houten, C.J. Survey of Asteroids. *Astrophysical Journal Supplement* **3**, p.289. 1958

(Lagerkvist *et al.* 1993)
Lagerkvist, C.I.; Fitzsimmons, A.; Magnusson, P.; Williams, I. P. Investigations of D-type asteroids. *Monthly Notices of the Royal Astronomical Society* **260-3**, p.679-680. 1993.

(Levy 1998)
Levy, David H. The Collision of Comet Shoemaker-Levy 9 with Jupiter. *Space Science Reviews* **85-3/4**, p.523-545. 1998.

(Li and Sandorff 1979)
Li Y.; Sandorff P. Project Icarus. Massachusetts Institute of Technology Press, 1979.

(Luu and Jewitt 1989)
Luu, Jane; Jewitt, David. On the relative numbers of C types and S types among near-earth asteroids. *Astronomical Journal* **98**, p.1905-1911. Nov 1989.

(Manley *et al.* 1998)
Manley, S. P.; Migliorini, F.; Bailey, M. E. An algorithm for determining collision probabilities between small solar system bodies. *Astronomy and Astrophysics Supplement*, **133**, p.437-444. 1998.

(McMillan 2000)
McMillan, R.S. Spacewatch Survey of the Solar System. Technical Report, FRS-305430 Lunar and Planetary Lab. 2000.

(Melosh 1988)
Melosh, H.J. Impact Cratering: A Geologic Process. Oxford Monographs on Geology and Geophysics , No 11. Oxford University Press. 1988.

(Migliorini *et al* 1998)
Migliorini, F.; Michel, P.; Morbidelli, A.; Nesvorný, D.; Zappalá, V. Origin of Multikilometer Earth- and Mars-crossing asteroids: a quantitative simulation. *Science* **281**, p.2022-2024. 25 Sep 1998

(Morbidelli *et al.* 2002a)
Morbidelli, A.; Bottke, W.F.; Froeschlé, C.; Michel, P. Origin and Evolution of Near-Earth Objects. In Asteroids III, (W. F. Bottke, A. Cellino, P. Paolicchi, R. P. Binzel, Eds.), The University of Arizona Press. 2002.

(Morbidelli *et al.* 2002b)
Morbidelli, A.; Jedicke, R.; Bottke, W. F.; Michel, P.; Tedesco, E. F. From magnitudes to diameters: the albedo distribution of Near Earth Objects and the Earth collision hazard. *Icarus* **158-2**, p.329-342. 2002

(Morrison 1992)
Morrison, D. The Spaceguard survey : report of the NASA International Near-Earth-Object Detection Workshop. Jet Propulsion Laboratory/California Institute of Technology, 1992.

(Morrison *et al.* 1994)
Morrison, D.; Chapman, C.R.; Slovic, P.; The Impact Hazard. In Hazards Due to Comets and Asteroids, (T. Gehrels, Ed.), The University of Arizona Press, Tucson, p.59-91. 1994.

(Morrison *et al.* 2002)
Morrison, D.; Hariss, A.W.; Sommer, G.; Chapman, C.R.; Carusi, A. Dealing with the Impact Hazard. In Asteroids III, (W. F. Bottke, A. Cellino, P. Paolicchi, R. P. Binzel, Eds.), The University of Arizona Press. 2002.

(Mottola *et al.* 1997)
Mottola, S.; Erikson, A.; Harris, A.W.; Hahn, G.; Neukum, G.; Buie, M.W.; Sears, W.D.; Harris, A.W.; Tholen, D.J.;Whiteley, R.J.; Magnusson, P.; Piironen, J.; Kwiatkowski, T.; Borczyk, W.; Howell, E.S.; Hicks, M.D.; Fevig, R.;Krugly, Y.N.; Velichko, F.P.; Chiorny, V.G.; Gaftonyuk, N.M.; di Martino, M.; Pravec, P.; Sarounova, L.; Wolf, M.; Worman, W.; Davies, J.K.; Schober, H.-J.; Pych, W. Physical Model of Near-Earth Asteroid 6489 Golevka (1991 JX) from Optical and Infrared Observations. *The Astronomical Journal* **114**, p. 1234. 1997.

(Namiki and Binzel 1991)
Namiki, N.; Binzel, R. P. The Evolution of the Surface of 951 Gaspra: A Pre-Galileo Estimate. *Abstracts of the Lunar and Planetary Science Conference* **22**, p.953. 1991.

(Neukum and Ivanov 1994)
Neukum, G.; Ivanov, B.A. Crater Size Distributions and Impact Probabilities on Earth from Lunar, Terrestrial-Planet, and Asteroid Cratering Data. In Hazards Due to Comets and Asteroids, (T. Gehrels, Ed.), The University of Arizona Press, Tucson, p.359-416. 1994.

(Nordyke 1962)
Nordyke, M.D. An Analysis of Cratering Data from Desert Alluvium. *Journal of Geophysical Research* **67**, p.1965. 1962

(Öpik 1951)
Öpik, E. J. Collision probability with the planets and the distribution of planetary matter. *Proceedings of the Royal Irish Academy Section A* **54**, p.165-199. 1951.

(Öpik 1960)
Öpik, E. J. The lunar surface as an impact counter. *Monthly Notices of the Royal Astronomical Society* **120**, p.404. 1960

(Öpik 1961)
Öpik, Ernst J. SYMPOSIUM: Comets: The survival of comets and cometary material. *Astronomical Journal* **66**, p.381. 1961.

(Öpik 1963)
Öpik, E. J. The stray bodies in the solar system. Part 1. Survival of cometary nuclei and the asteroids. *Advances in Astronomical Astrophysics* **2**, p.219-261. 1963.

(Pope *et al.* 1997)
Pope, K.O.; Ocampo, A.C.; Baines, K.H. Constraints on volatile production by the Chicxulub impact. 28th Annual Lunar and Planetary Science Conference, p.127. 1997

(Pierazzo *et al.* 1997)
Pierazzo, E.; Vickery, A. M.; Melosh, H. J. A Reevaluation of Impact Melt Production. *Icarus* **127-2**, p.408-423. 1997.

(Pravdo *et al.* 1997)
Pravdo, S.H.; Rabinowitz, D.L.; Helin, E.F.; Lawrence, K.J.; Bambery, R.J.; Clark, C.C.; Groom, S.L.; Levin, S.; Lorre, J.; Shaklan, S.B.; Kervin, P.; Africa, J.A.; Sydney, P.; Soohoo, V. The Near-Earth Asteroid Tracking (NEAT) Program: an Automated System for Telescope Control, Wide-Field Imaging, and Object Detection. *The Astronomical Journal* **117-3**, p.1616-1633. 1997.

(Pravec *et al.* 1997)
Pravec, Petr; Wolf, Marek; Sarounova, Lenka; Harris, Alan W.; Davies, John K. Spin Vector, Shape, and Size of the AMOR Asteroid (6053) 1993 BW_3. *Icarus* **127**-2, p.441-451. 1997.

(Pravec and Harris 2000)
Pravec, P.; Harris, A.W. Fast and Slow Rotation of Asteroids. *Icarus* **148-1**, p.12-20. 2000

(Rabinowitz 1993)
Rabinowitz, D.L. The size Distribution of the Earth-approaching Asteroids. *The Astrophysical Journal* **407**, p.412-427. 1993.

(Rabinowitz 1994)
Rabinowitz, David L.; The Size and Shape of the Near-Earth Asteroid Belt. *Icarus* **111**, p.364-377. 1994.

(Rabinowitz *et al.* 2000)
Rabinowitz, D.; Helin, E.; Lawrence, K.; Pravdo, S. A reduced estimate of the number of kilometer-sized near-Earth asteroids. *Nature* **403**, p.165-166. 13 Jan 2000.

(Rivkin *et al.* 2002)
Rivkin, A.S.; Howell, E.S.; Vilas, F.; Lebofsky, L.A. Hydrated Minerals on Asteroids: The Astronomical Record. Technical Report, Massachusetts Institute of Technology, Cambridge, MA. 2002.

(Rork 1998)
Rork, E.W. Photometric Calibration with the USNO-SA1.0 Astrometric Star Catalog. Lincoln Laboratory Technical Report, ETS-133. MIT Lincoln Laboratory, Lexington Massachusetts. 1998.

(Russell 1916)
Russell, H.N.. On the Albedo of the Planets and their Satellites. *The Astrophysical Journal* **18-3**, p.173-196. 1916.

(Schmidt and Housen 1987)
Schmidt, R. M.; Housen, K. R. Some recent advances in the scaling of impact and explosion cratering. *International Journal of Impact Engineering* **5**, p.543-560. 1987.

(Sekanina 1998)
Sekanina, Z. Evidence for asteroidal origin of the Tunguska object. *Planetary and Space Science*, **46-2/3**, p.191-204. 1998.

(Shoemaker 1960)
Shoemaker, E.M. Impact mechanics at Meteor Crater, Arizona. PhD. Thesis, Princeton University, 1960.

(Shoemaker *et al.* 1977)
Shoemaker, E.M.; Helin, E.F. Populations of Planet-Crossing Asteroids and the Relation of Apollo Objects to Main-Belt Asteroids and Comets. In Comets, Asteroids, Meteorites: Interrelations, Evolution, and Origins, (A.H. Delsemme, Ed.), The University of Toledo Press, p.297-300. 1977.

(Shoemaker 1977)
Shoemaker, E.M. Astronomically observable crater-forming projectiles. In Impact and Explosion Cratering: Planetary and Terrestrial Implications, (Roddy, Pepin, Merrill, Eds.) Pergamon, New York, p.617-728. 1977.

(Shoemaker *et al* 1979)
Shoemaker, E.M.; Williams, J.G.; Helin, E.F.; Wolfe, R.F. Earth-crossing asteroids: Orbital classes, collision rates with Earth, and origin. In Asteroids, (T. Gehrels, Ed.), p. 253-282. 1979.

(Shoemaker 1983)
Shoemaker, E.M. Asteroid and Comet Bombardment of the Earth. *Annual Review of Earth and Planetary Science* **11**, p,461-494. 1983.

(Shoemaker *et al.* 1990)
Shoemaker, E.M.; Wolfe, R.F.; Shoemaker, C.S.; Asteroid and comet flux in the neighborhood of Earth. Geological Society of America Special Paper 247. 1990.

(Slivan 1995)
Slivan, S.M. Spin-Axis Alignment of Koronis Family Asteroids. PhD. Thesis. Massachusetts Institute of Technology. 1995.

(Stöffler and Ryder 2001)
Stöffler D.; Ryder G. Stratigraphy and isotope ages of lunar geologic units: Chronological standard for the inner solar system. In Chronology and Evolution of Mars (R. Kallenbach *et al.*, Eds.). Kluwer, Dordrecht, p.9-54. 2001.

(Stokes *et al.* 1998)
Stokes, G.H.; Viggh, H.E.M.; Shelly, F.L.; Blythe, M.S.; Stuart, J.S. Results from the Lincoln Near Earth Asteroid Research (LINEAR) Project. American Astronomical Society, DPS meeting #30, #16.07; *Bulletin of the American Astronomical Society* **30**, p.1042. 1998

(Stokes *et al.* 2000)
Stokes, G.H.; Evans, J.B.; Viggh, H.E.M.; Shelly, F.C.; Pearce, E.C. Lincoln Near-Earth Asteroid Program (LINEAR). *Icarus* **148-1**, p.21-28. 2000.

(Stuart 2001)
Stuart, J.S. A Near-Earth Asteroid Population Estimate from the LINEAR Survey. *Science* **294**, p.1691-1693. 23 Nov 2001.

(Tedesco *et al.* 1989)
Tedesco, E. F.; Williams, J. G.; Matson, D. L.; Weeder, G. J.; Gradie, J. C.; Lebofsky, L. A. A three-parameter asteroid taxonomy. *Astronomical Journal* **97**, p.580-606. 1989.

(Tedesco *et al.* 2002)
Tedesco, E.F.; Noah, P.V.; Noah, M.; Price, S.D. The Supplemental IRAS Minor Planet Survey. *The Astronomical Journal* **123-2**, p.1056-1085. 2002.

(Tisserand 1896)
Tisserand, F. Traité de Mécanique Céleste, Vol. 4. Paris: Gauthier-Villars. 1896.

(Tholen 1984)
Tholen, D. J. Asteroid taxonomy from cluster analysis of Photometry. Ph.D. Thesis, The University of Arizona, Tucson. 1984

(UK NEO Task Force 2000)
UK NEO Task Force. Report of the Task Force on Potentially Hazardous Near Earth Objects. UK NEO Information Centre, London. http://www.nearearthobjects.co.uk/ 2000.

(van Houten *et al.* 1970)
van Houten, C.J.; van Houten-Groeneveld, I.; Herget, P.; Gehrels, T. The Palomar-Leiden survey of faint minor planets. *Astronomy & Astrophysics Supplement Series* **2-5**, p.339. 1970.

(Veverka *et al* 2001)
Veverka, J.; Farquhar, B.; Robinson, M.; Thomas, P.; Murchie, S.; Harch, A.; Antreasian, P. G.; Chesley, S. R.; Miller, J. K.; Owen, W. M.; Williams, B. G.; Yeomans, D.; Dunham, D.; Heyler, G.; Holdridge, M.; Nelson, R. L.; Whittenburg, K. E.; Ray, J. C.; Carcich, B.; Cheng, A.; Chapman, C.; Bell, J. F.; Bell, M.; Bussey, B.; Clark, B.; Domingue, D.; Gaffey, M. J.; Hawkins, E.; Izenberg, N.; Joseph, J.; Kirk, R.; Lucey, P.; Malin, M.; McFadden, L.; Merline, W. J.; Peterson, C.; Prockter, L.; Warren, J.; Wellnitz, D. The landing of the NEAR-Shoemaker spacecraft on asteroid 433 Eros. *Nature* **413-6854**, p.390-393. 2001.

(Viggh *et al.* 1998a)
Viggh H.E.M.; Stokes G.H.; Shelly F.C.; Blythe M.S.; Stuart J.S. Results from the Lincoln Near Earth Asteroid Research (LINEAR) Project. 29th Annual Meeting of the Division for Planetary Sciences of the American Astronomical Society, Cambridge, MA. 1998.

(Viggh *et al.* 1998b)
Viggh, H.E.M.; Stokes,G.H.; Shelly, F.C.; Blythe, M.S.; Stuart, J.S. Applying Electro-Optical Space Surveillance Technology to Asteroid Search and Detection: The LINEAR Program Results. Proceedings of the Sixth International Conference and Exposition on Engineering, Construction, and Operations in Space, p.373-381. 1998

(Weissman *et al.* 1989)
Weissman, Paul R.; A'Hearn, Michael F.; Rickman, H.; McFadden, L. A. Evolution of comets into asteroids. In Asteroids II (R.P. Binzel, T. Gehrels, M. Matthews, Eds.), The University of Arizona Press, p.549-556. 1989.

(Weissman *et al.* 2002)
Weissman, P.R.; Bottke, W.F.; Levison, H.F. Evolution of Comets into Asteroids. In Asteroids III (W. F. Bottke, A. Cellino, P. Paolicchi, R. P. Binzel, Eds.). The University of Arizona Press. 2002.

(Werner *et al.* 2002)
Werner, S. C.; Harris, A. W.; Neukum, G.; Ivanov, B. A. NOTE: The Near-Earth Asteroid Size-Frequency Distribution: A Snapshot of the Lunar Impactor Size-Frequency Distribution. *Icarus* **156-1**, p.287-290. 2002.

(Wetherill 1967)
Wetherill, G. W. Collisions in the asteroid belt. *Journal of Geophysical Research* **72**, p.2429-2444. 1967.

(Wetherill 1976)
Wetherill, G.W. Where do the meteorites come from? A re-evaluation of Earth-crossing Apollo objects as sources of chondritic meteorites. *Geochimica et Cosmochimica Acta* **40**, p.1297-1318. 1976.

(Wetherill 1979)
Wetherill, G.W. Steady state populations of Apollo-Amor objects. *Icarus* **37**, p.96-112. Jan 1979.

(Wisdom 1981)
Wisdom, J.L. The origin of the Kirkwood gaps: A mapping for asteroidal motion near the 3/1 commensurability 1. The resonance overlap criterion and the onset of stochastic behavior in the restricted three-body problem 2. Ph.D. Thesis California Institute of Technology, Pasadena, CA. 1981.

(Wisdom 1982)
Wisdom, J. The origin of the Kirkwood gaps - A mapping for asteroidal motion near the 3/1 commensurability. *Astronomical Journal* **87**, p.577-593. Mar 1982.

(Wisdom 1983)
Wisdom, J. Chaotic behavior and the origin of the 3/1 Kirkwood gap. *Icarus* **56**, p.51-74. Oct 1983.

(Wisdom 1985)
Wisdom, J. Meteorites may follow a chaotic route to earth. *Nature* **315**, p.731-733. 27 Jun 1985.

(Whipple 1967)
Whipple, F.L. The meteoritic environment of the Moon. *Proceedings of the Royal Society of London* **296A**, p.304. 1967.

(Wood and Kuiper 1963)
Wood, X.H.J.; Kuiper, G.P. Photometric Studies of Asteroids. *Astrophysical Journal* **137**, p.1279. 1963

(Xu *et al.* 1995)
Xu, S.; Binzel, R.P.; Burbine, T.H.; Bus, S.J. Small main-belt asteroid spectroscopic survey: Initial results. *Icarus* **115-1**, p.1-35. 1995.

(Zellner 1973)
Zellner, B. Polarimetric Albedos of Asteroids. *Bulletin of the American Astronomical Society* **5**, p.388. 1973.

Appendix: Definitions

A.1 Absolute Magnitude

The principal photometric properties of asteroids are described by the IAU two-parameter magnitude system for asteroids (Bowell *et al.* 1989) using the parameters *H,* and *G*. The absolute magnitude, *H*, is the magnitude of the asteroid at unit distance from the observer and the Sun (1 astronomical unit) and at zero solar phase angle (fully illuminated). The phase slope parameter, *G*, describes how the brightness falls with increasing solar phase angle, as less of the visible portion of the asteroid is illuminated. The apparent magnitude may be calculated from *H*, and *G* as (Bowell *et al.* 1989):

$$
\begin{aligned}
V &= H + 5\log_{10}(R\Delta) - 2.5\log_{10}\left((1-G)\Phi_1(\alpha) + G\Phi_2(\alpha)\right) \\
\Phi_1(\alpha) &= \exp\left(-3.33\left(\tan\frac{\alpha}{2}\right)^{0.63}\right) \\
\Phi_2(\alpha) &= \exp\left(-1.87\left(\tan\frac{\alpha}{2}\right)^{1.22}\right)
\end{aligned}
\tag{A.1}
$$

where *R* and Δ are the distances from the sun and observer in astronomical units (AU), and α is the solar phase angle (observer-asteroid-sun angle). The phase slope parameter is usually between 0 and 1, but can fall outside that range. Smaller values of *G* indicate a more severe drop in brightness at high phase angle.

The absolute magnitude is related to the diameter and geometric albedo of the asteroid, assuming a spherical asteroid with no variation across the surface, by (Harris and Harris 1997):

$$
\begin{aligned}
H &= 15.618 - 5\log_{10} D - 2.5\log_{10} p_V \\
D &= \frac{1329}{\sqrt{p_V}} 10^{-0.2H} \\
p_V &= \frac{1329^2}{D^2} 10^{-0.4H}
\end{aligned}
\tag{A.2}
$$

where *D* is the diameter in kilometers, and p_V is the visual geometric albedo. Care must be taken to ensure that *H*, *G*, and p_V are all measured at the same wavelength, usually in the middle part of visible wavelengths (V-band, Bessell 2002).

A.2 Orbital Parameters

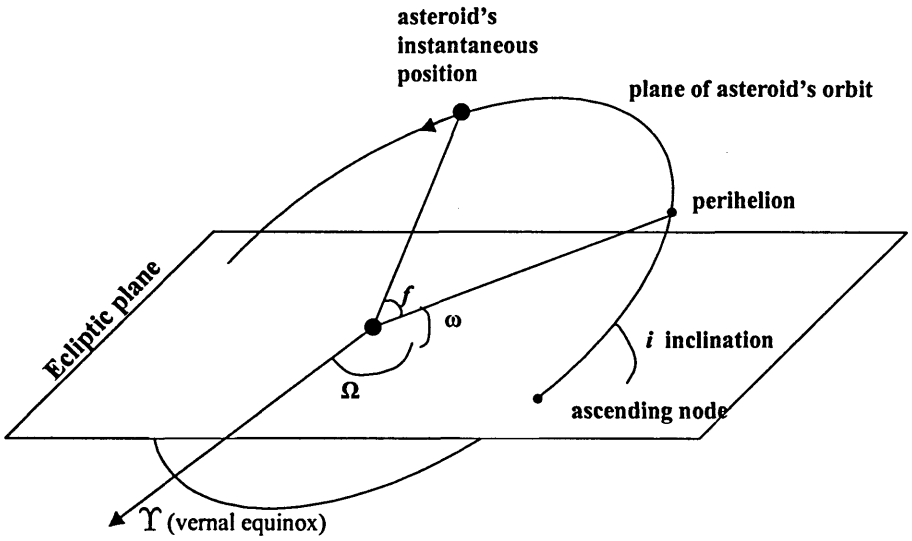

- a = semi-major axis - the size of the ellipse
- e = eccentricity - amount of deviation from a circle
- i = inclination – angle between the orbit plane and the Earth's orbit plane (the Earth's obit plane is called the Ecliptic plane)
- Ω = longitude of the ascending node – position where asteroid crosses the ecliptic plane going from South to North (ascending). The angle is measured in the ecliptic plane from the vernal equinox.
- ω = argument of perihelion – angle between the ascending node and the perihelion point (closest point to the sun). The angle is measured in the orbital plane.
- f = true anomaly – angle from perihelion to position of the asteroid, measured in the orbit plane.
- mean anomaly is an angle that is used instead of true anomaly for specifying orbits. It is linearly proportional to time, and is converted to true anomaly by Kepler's equation and a geometric transformation.

A.3 Jovian Tisserand Parameter

The Jovian Tisserand parameter (Tisserand 1896) is a measure of the degree to which an asteroid's orbit is dynamically linked to Jupiter. The Tisserand parameter is calculated from the orbital elements by:

$$T_J = \frac{a_J}{a} + 2\cos(i)\sqrt{\frac{a}{a_J}\left(1-e^2\right)} \tag{A.3}$$

where a_J is the semi-major axis of Jupiter (approximately 5.2 AU), and a,e,i are the semi-major axis, eccentricity, and inclination of the asteroid. T_J is approximately equal to Jacobi's integral, which is a conserved quantity in the circular, restricted, three-body problem. If an asteroid makes a close approach to Jupiter, its orbital elements may change drastically, but the value of T_J is approximately conserved.